

DOCTORAL THESIS

Biologically inspired computer models of the
microscopic and macroscopic structure of the brain
based on wiring optimisation



by

Moritz Groden

Institut für Theoretische Physik
Justus-Liebig-Universität Gießen

Gießen, 2022

Supervised by

Prof. Dr. Christian Heiliger

Prof. Dr. Peter Jedlička

Contents

List of Figures	4
1 Abstract	7
2 Zusammenfassung	8
3 Introduction	9
3.1 The Macroscopic structure of the brain: Gyrification	9
3.1.1 Gyrification of the brain	9
3.1.2 Cortical connectivity	14
3.1.3 Wiring optimisation	16
3.2 The Microscopic structure of the brain: Neuron reconstructions	19
3.2.1 Human neuron morphology reconstructions	19
3.2.2 Repairing neuron morphologies	21
3.2.3 Neuron biological regrowth	24
4 Materials and methods	26
4.1 Gyrification model	26
4.1.1 Optimal placement	26
4.1.2 Folding connectivity	27
4.1.3 The folding index	28
4.1.4 Fractal dimension	30
4.1.5 Fold frequency and Amplitude	31
4.1.6 Discarding degenerate folding patterns automatically	32
4.2 Neuron dendrite repair tool	34
4.2.1 The <i>fix_tree</i> function	34
4.2.2 (T2N) Electrophysiological properties	37
5 Research and results	41
5.1 The scope of this thesis: Optimal wiring-based macroscopic and microscopic models of the nervous system	41
5.2 Macroscopic modelling: A computational model of gyrification	42
5.2.1 The impact of connectivity	49
5.2.2 Breaking symmetry	51

5.3	Microscopic modelling: A realistic neuron repair algorithm	56
5.3.1	The GUI and <i>fix_tree</i> function	57
5.3.2	Validating the neuron repair algorithm	60
5.3.3	Repairing human CA1 pyramidal neurons	64
5.3.4	Electrophysiology in repaired human and mouse cells and differences between the two species	67
5.3.5	Repairing other cell types	75
5.3.6	Biological repair of class IV da-neurons of <i>D. melanogaster</i>	77
6	Discussion	80
6.1	What causes the brain to fold?	80
6.2	Folding in pathological human brains	86
6.3	Gyrification model relationships	88
6.4	The lissencephalic manatee	92
6.5	Benefits of a neuron dendritic repair tool	93
6.6	Recovering human CA1 pyramidal neuron morphology and electrophysiology	95
6.7	Neuron dendrite regeneration	99
6.8	Pros and cons of the neuron repair tool	100
6.9	Conclusion	101
7	Publications	103
8	Acknowledgements	104
9	Declaration	105
10	References	106
11	Appendix	124

List of Figures

1	Different methods of calculating the folding index FI	9
2	Folding index of the cortex of different species depending on the number of neurons	10
3	Scaling behaviour of FI in different orders of species with respect to brain weight	11
4	Folding index of sheets of paper of varying size and thickness	12
5	Local short range connection probability among neurons of different layers in the cortex	15
6	Network cost and efficiency	16
7	Dimension reduction methods can recover neuron positions based on connectivity	17
8	MDS predicts pinwheel arrangements of neurons found in the visual cortex . .	18
9	Neuron complexity affects spiking behaviour	20
10	The dendrite growth algorithm based on optimal wiring finds the optimal trade-off between cable length and conduction delay	22
11	Microscope images of mouse CA1 data set	23
12	Total and exposed circumference	29
13	Horizontal projection of a folding pattern boundary	32
14	MST growing into distributed carrier points	35
15	Cortical folding derived from connectivity	43
16	Folding patterns with extreme folding	44
17	Degenerate folding results	45
18	Cortical folding transition from lissencephalic to convoluted	46
19	Quantifying gyrification	47
20	The exception of the manatee	48

21	<i>FI</i> scaling for different mammalian orders predicted by the brain folding model	48
22	Connectivity parameters	49
23	The impact of connectivity on folding patterns	50
24	Folding patterns with the same parameters are not identical	52
25	Stereotypical folding patterns	53
26	Characteristic single folds	54
27	Model predictions of folding changes in brain disorders	55
28	Neuron repair tool GUI	58
29	Lost dendritic material can be recovered with the new growth algorithm	59
30	Successful repair of artificially damaged mouse CA1 pyramidal neurons	61
31	Statistics for the main features of dendrite morphology shows a successful recovery of lost dendrites	63
32	Dendritic segment definition	64
33	Human CA1 pyramidal neuron data set	65
34	Repairing human CA1 pyramidal neurons	66
35	Repairs recover a neuron's original firing behaviour	68
36	Human dentate gyrus granule cell morphology and passive property simulation	70
37	Passive electrophysiological properties of human and mouse dentate gyrus granule cells	71
38	Passive electrophysiological properties of human dentate gyrus granule cells separated by Wyler grade	73
39	Comparing morphological properties of mouse and human granule and CA1 pyramidal neurons	74

40	Repairing different cell types: hippocampal granule cells, cerebellar Purkinje cells and artificially grown cells	76
41	Biological regrowth using the neuron repair tool	78
42	Rostrocaudal folding differences	82
43	From cortical arrangement to nuclei	84
44	Local and global folding forces	85
45	Increasing M leads to lissencephaly	87
46	Modelling specific anatomical structures	92
S1	Human neuron extension volumes	124

1 Abstract

Like all natural systems, the mammalian brain and its neurons are governed by the fundamental principles of physics. Simplified computer simulations based on such principles help us see through the high complexity of especially the human brain and ultimately figure out how it works. In the scope of this thesis, two biologically realistic models were created focusing on, firstly the macroscopic and secondly the microscopic structure of the brain. The key component to both of these morphological simulations is the principle of wiring optimisation. First, combining dimensionality reduction methods and biologically inspired modelling based on optimal wiring, this thesis develops a method to simulate how the gyrification pattern of the mammalian brain emerges, differs from species to species, and changes due to pathological changes in neuron connectivity. The gyrification model is based on two biology-driven key principles: First, neuron placement follows wiring optimisation requirements and second, local connectivity between neurons is strong while long range connectivity is sparse as observed in the mammalian cortex. Many studies from the past saw the formation of gyri and sulci as the result of the surface of the cortex trying to expand in the limited cavity of the skull. The simulation described here shows that even without the constraint of the skull, gyrification still emerges when applying a biological neural connectivity distribution in addition to wiring optimisation.

The first model provides new insights into the macroscopic structure of the brain but lacks microscopic detail. The second model is also based on optimal wiring but focused on reproducing the anatomical neuronal structure at the level of single cells. It provides a new algorithm and a tool to repair and preserve the microscopic structure of neuron morphology reconstructions. This is especially relevant for human neurons since here, data is extremely hard to come by, and the data that is available mostly originates from patients with diseases like severe epilepsy. Since the reconstruction process is a delicate procedure, the anatomical structure of reconstructed neurons is oftentimes severed by dendrites accidentally being cut. The recovered anatomy of neuronal dendrites is, however, pivotal to study the functionality of human and nonhuman neurons, which is further illustrated by analysing passive electrophysiological differences between human and mouse neurons.

In summary, the thesis shows that optimal wiring is a useful guiding principle to simulate and better understand macroscopic and microscopic anatomical structure of the brain at the level of cortical folding as well as individual dendritic trees of nerve cells.

2 Zusammenfassung

Wie alle natürlichen Systeme unterliegt auch das Gehirn von Säugetieren und seine Neuronen den grundlegenden Prinzipien der Physik. Im Rahmen dieser Arbeit wurden zwei biologisch realistische Modelle erstellt, die sich zum einen auf die makroskopische und zum anderen auf die mikroskopische Struktur des Gehirns konzentrieren. Die Schlüsselkomponente dieser beiden morphologischen Simulationen ist das Prinzip der Verdrahtungsoptimierung. Zunächst wird in dieser Arbeit durch die Kombination von Methoden zur Dimensionalitätsreduktion und biologisch inspirierter Modellierung auf der Grundlage optimaler Verdrahtung eine Methode entwickelt, mit der simuliert werden kann, wie das Faltungsmuster des Säugetiergehirns entsteht, wie es sich von Art zu Art unterscheidet und wie es sich durch pathologische Veränderungen der Neuronenverknüpfungen verändert. Das Faltungsmodell basiert auf zwei biologisch begründeten Grundprinzipien: Erstens folgt die Platzierung von Neuronen den Anforderungen an eine optimale Verdrahtung, und zweitens ist die lokale Konnektivität zwischen Neuronen stark, während die Konnektivität über weite Entfernungen gering ist, wie es im Kortex von Säugetieren beobachtet wird. Die hier beschriebene Simulation zeigt, dass auch ohne die Beschränkung durch den Schädel Faltungen entstehen, wenn zusätzlich zur Optimierung der Verdrahtung eine biologische Verteilung der neuronalen Konnektivität angewendet wird.

Das erste Modell bietet neue Einblicke in die makroskopische Struktur des Gehirns, lässt aber mikroskopische Details vermissen. Das zweite Modell basiert ebenfalls auf dem Prinzip der optimalen Verdrahtung, konzentriert sich aber auf die Reproduktion der neuronalen Struktur auf der Ebene einzelner Zellen. Es bietet einen neuen Algorithmus und ein Werkzeug zur Reparatur und Erhaltung der mikroskopischen Struktur von Neuronenmorphologierekonstruktionen. Dies ist vor allem für menschliche Neuronen von Bedeutung, da hier Daten extrem schwer zu bekommen sind und die verfügbaren Daten meist von Patienten mit Krankheiten wie schwerer Epilepsie stammen. Die wiederhergestellte Anatomie neuronaler Dendriten ist jedoch entscheidend für die Untersuchung der Funktionalität menschlicher und nicht-menschlicher Neuronen, was durch die Analyse der passiven elektrophysiologischen Unterschiede zwischen menschlichen und Mäuseuronen weiter veranschaulicht wird.

Zusammenfassend zeigt die Arbeit, dass die optimale Verdrahtung ein nützliches Leitprinzip ist, um die makroskopische und mikroskopische anatomische Struktur des Gehirns zu simulieren und besser zu verstehen.

3 Introduction

3.1 The Macroscopic structure of the brain: Gyrification

3.1.1 Gyrification of the brain

The mammalian brain has a distinct appearance with its striking cortical folding pattern. These folds revolve around gyri (ridges or outward folds) and sulci (depressions or furrows). A gyrus is typically surrounded by sulci and vice versa. Gyrification appears in a wide variety of mammals, such as humans, carnivores, dolphins, whales and non human primates etc. (Welker (1990), Bayly et al. (2014), Kroenke and Bayly (2018)). Interestingly, the degree of cortical folding varies dramatically from species to species (Pillay and Manger (2007), Zilles et al. (2013), Huggenberger (2008)), ranging from cortices with no folds at all (lissencephalic), in for example, rats, to highly convoluted specimen, like dolphin brains.

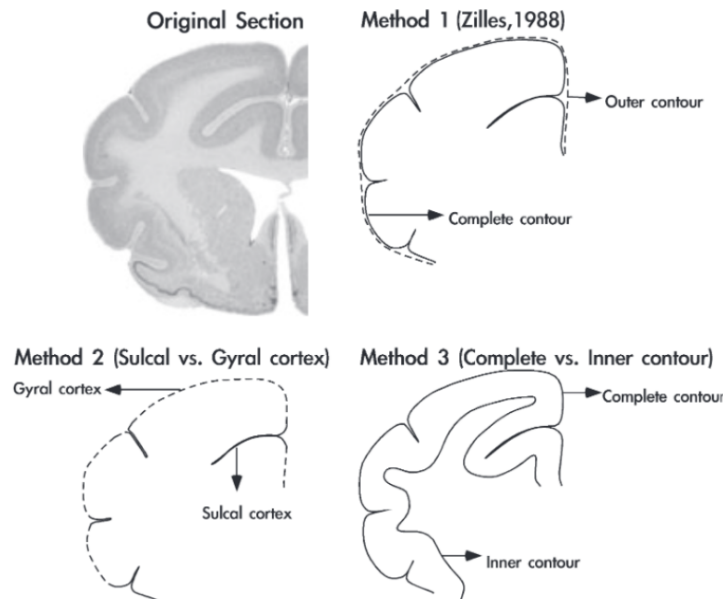


Figure 1. Different methods of calculating the folding index FI

(Note: Figure by Pillay and Manger (2007), Fig. 2) Example methods of how to calculate the folding index FI by comparing two different contours of the cortex. **Top left:** Image of cortex section. **Top right:** Method 1 is the most popular way to determine FI by comparing the complete contour to the outer contour. **Bottom:** Method 2 and 3 depict alternative procedures to determine FI .

The degree of folding is measured using the folding index (FI). There are several different methods of calculating FI (Pillay and Manger (2007)) which are depicted in Fig. 1. Method 1 compares the exposed circumference A_E (here complete contour) to the total circumference A_T (here outer contour) by forming the quotient as follows.

$$FI = \frac{A_T}{A_E}$$

In this thesis FI will be calculated using this method.

Increasing the cortical surface area increases the number of neurons as well, enhancing cognitive capabilities. It was therefore popularly assumed that cortical folding is the result of the brain trying to expand in the limited cavity of the skull, thereby increasing its surface area (Welker (1990)). This is, however, largely inaccurate since studies in mice have shown that cortical folding can be induced by a genetic change that triggers a cortical surface expansion (Chenn and Walsh (2003), Kingsbury et al. (2003)). In conjunction with lesion experiments which were able to show that folding emerges even without any space limiting cavity during brain development, these findings debunk the expanding brain theory (Barron (1950), Welker (1990)). The expanding brain theory furthermore has difficulties explaining anomalies like the lissencephalic cortex of the manatee.

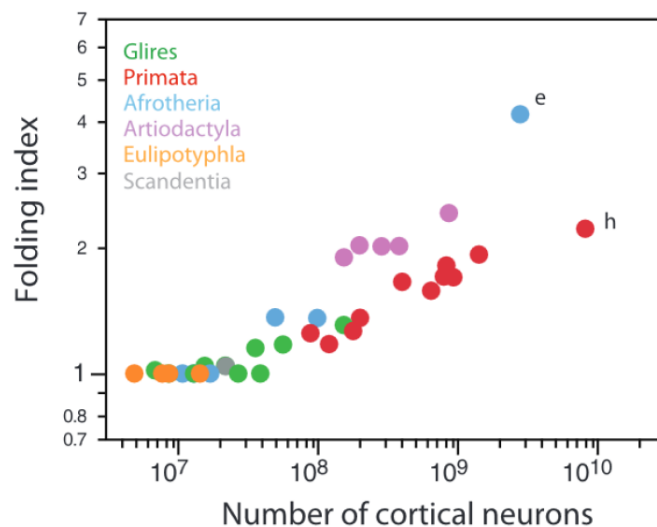


Figure 2. Folding index of the cortex of different species depending on the number of neurons (Note: Figure by Mota and Herculano-Houzel (2015), Fig. 1 B) The folding indices of different species plotted against the number of neurons in their respective cortices.

Despite having similar numbers of neurons to primates, the manatee's cortex does not exhibit any folding (Charvet et al. (2016)), which is strikingly odd since, in general, folding seems to increase with the number of cortical neurons in mammals as shown in Fig. 2. Therefore, the low degree of folding in rodents like mice and rats compared to other mammalian species is unlikely to be the result of their small size. The degree of cortical gyrification does not only vary from species to species but seems to obey scaling laws specific to orders of mammals as described by Zilles et al. (2013). They visualise this in Fig. 3, which plots the FI (here GI for gyrification index) against the brain weight for different orders of mammals in **a** and different families of primates in **b**.

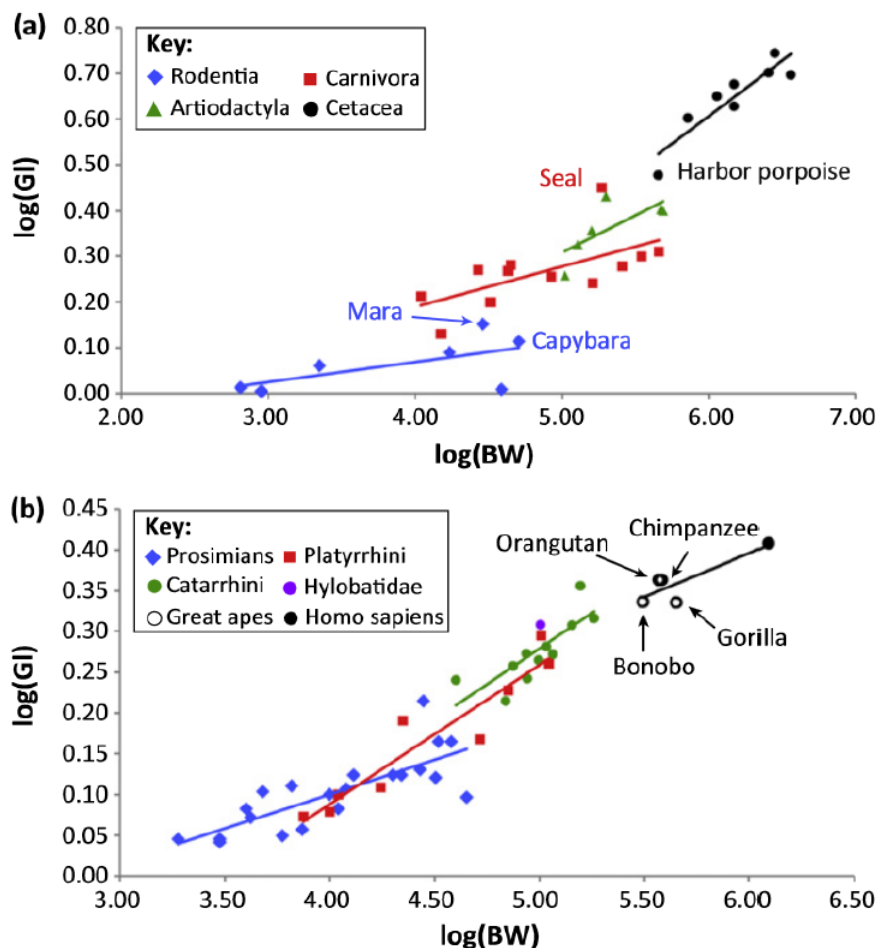


Figure 3. Scaling behaviour of FI in different orders of species with respect to brain weight

(Note: Figure by Zilles et al. (2013), Fig. 1 (a) and (b)) **(a)** Logarithm of the gyrification index GI (equivalent to the folding index) plotted against the logarithm of the brain weight for different species. The scaling of GI is fitted for different orders of species indicated by colours, revealing differences in scaling between orders. **(b)** Same plot as in (a) but for different primate species.

The brain weight can be used as a substitute measure for the number of cortical neurons as was shown by Herculano-Houzel (2009). Among primates, the homo sapiens brain shows the highest degree of folding, however, folding is at its most extreme in cetaceans who also exhibit the most intense scaling of gyrification with increasing number of cortical neurons. Cortices of cetaceans also are very thin (Hof and Van Der Gucht (2007)).

Brain functionality is dependent on its anatomy and vice versa, as for a healthy brain specific functions are strictly localised on the cortical surface. Therefore, it is likely that there is a link between anatomy and functionality of the brain (Rakic (1988) Welker (1990), Felleman and Van Essen (1991), Amunts and Zilles (2015)). Even though there are multiple hypotheses regarding the emergence of cortical folding patterns, the exact mechanism is largely unknown. Some models suggest physical forces are responsible for the formation of gyri and sulci by pulling them towards each other (Tallinen et al. (2014), Tallinen et al. (2016), Mota and Herculano-Houzel (2015)). Such forces could explain the different degrees of folding in different species (Pillay and Manger (2007), Zilles et al. (2013)) as the level of gyrification depends on cortical thickness and its surface area (Mota and Herculano-Houzel (2015)). The cortex behaves similarly to a crumpling sheet of paper where the amount of folding has been shown to increase with larger but at the same time thinner sheets as depicted in Fig. 4. Folding patterns in the cortex, which are dependent on cortical functionality, can however be inherited across generations (Welker (1990), Bartley et al. (1997), Biondi et al. (1998),

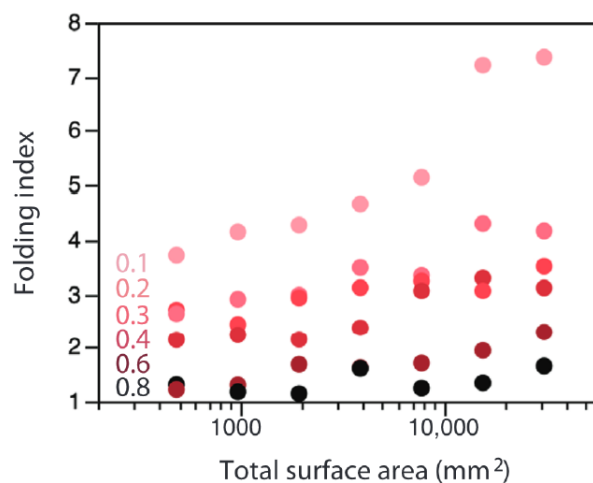


Figure 4. Folding index of sheets of paper of varying size and thickness

(Note: Figure by Mota and Herculano-Houzel (2015), Fig. 2 B) The folding index of crumpled sheets of paper plotted against their surface area. The different colours indicate the sheet thickness as shown by the inlay numbers in mm.

Lohmann et al. (1999), Fischl et al. (2008)), suggesting that connectivity and genetic parameters influence the final appearance of any folding pattern. Llinares-Benadero and Borrell (2019) do indeed observe changes in the expression of genes during cortical development. These changes of gene expression, which occur mostly in the outer subventricular zone (OSVZ), do correspond to the locations where ultimately a gyrus or sulcus will emerge (de Juan Romero et al. (2015)). The cortex seems to fold as the OSVZ forms, which allows for the proliferation of basal progenitor cells that are situated within the OSVZ (Poluch and Juliano (2015), Martínez-Martínez et al. (2016)). This is in line with Reillo et al. (2011) and Nonaka-Kinoshita et al. (2013) who find that the regulation of genes that govern proliferation of the OSVZ in ferrets either increases or decreases the cortical surface area, which in turn leads to a change in gyrification. The basal progenitor cells are likely to be among the architects of folding, as they change the framework of radial fibers. This allows proliferated neurons to spread out tangentially, forming a gyrus (Reillo et al. (2011), Borrell and Reillo (2012), Borrell and Götz (2014), Borrell (2018), Del Toro et al. (2017)). Importantly, gyrification does not start before neurogenesis is completed. Gliogenesis begins once all excitatory neurons have reached their final locations and folding is initiated (Kroenke and Bayly (2018), Rash et al. (2019)). Therefore, gyrification is likely to be the result of connections forming throughout white matter as neurons differentiate alongside the cortex expanding.

The folding pattern of the cortex has also been observed to change with pathological diseases, such as autism, schizophrenia and persistent epilepsy (Walsh (1999), Bayly et al. (2014), Barkovich et al. (2012), Fernández et al. (2016), Kroenke and Bayly (2018)). These observations further underline the interdependence of functionality and anatomy of the cortex. The folding pattern changes due to pathological deficiencies of its microscopic structure and connectivity. Pinpointing exactly what mechanical forces are at work when gyrification emerges, is however, a controversial debate. The tension exerted by axons could theoretically be one component of the force acting on neurons. This is underlined by experiments, confirming that the axonal tension is a substantial force acting on neurons (Mota and Herculano-Houzel (2012), Xu et al. (2009), Chada et al. (1997), Geng et al. (2009), Hilgetag and Barbas (2006)). Folding could also be caused by the cortex expanding tangentially (Ronan et al. (2014), Kroenke and Bayly (2018)). This theory, is however, not as popular as the axonal tension hypothesis since pulling axons would be consistent with wiring optimisation. Saving wiring cost is an essential concept in the brain as it decreases signal travel time as well as conserving resources (Laughlin and Sejnowski (2003), Ruppín et al. (1993), Van Essen (1997), Hilgetag and Barbas (2009)).

Nonetheless the tension between the opposing walls of a gyrus, which was supposed to be the pivotal factor (Van Essen (1997)), was found to be negligible (Xu et al. (2010)). Therefore, the tangential expansion theorem seems to be more plausible. With the exact mechanism that leads to gyrification, when considering tangential expansion being unclear (Ronan and Fletcher (2015), Kroenke and Bayly (2018)), it is hypothesised that folding is induced by different expansion speeds of different layers. In case an outer layer of the cortex expands faster than its corresponding inner layer, a gyrus could form. In case the roles of the layers are reversed, a sulcus would emerge (Bayly et al. (2013), Budday et al. (2014), Richman et al. (1975)).

Another major factor in gyrification is likely to be cortical connectivity, as it heavily influences local cytoarchitecture (Rakic (1988), Dehay et al. (1991), O'Leary et al. (2007)). Additionally, connectivity influences the size of specific cortical areas, leading to the formation of stereotypical folding patterns (Ronan and Fletcher (2015)). In general, structures in neuroanatomy are restricted by connectivity (Laughlin and Sejnowski (2003), Bullmore and Sporns (2012), Chklovskii and Koulakov (2004)).

3.1.2 Cortical connectivity

The mammalian brain is organised microscopically and macroscopically. On the macroscopic scale, different brain areas fulfil different functions and are interconnected to link information from for example, different sensory organs. On a cellular level, six different layers can be observed in the cortex. Information travels up and down the layers (vertically) with neurons in close vicinity being highly interconnected. This local cytoarchitecture is organised into so called cortical columns which span the layers vertically. Connectivity between different areas (global connectivity) is different from connectivity within and in between neighbouring cortical columns (local connectivity). While both local and global connectivity drop off rapidly with distance, global connectivity is sparse compared to local connectivity. A study by Hellwig (2000) found connectivity between neurons separated by more than $500\mu m$ (long range) to drop to 0% – 15% in contrast to the local 50% – 80%. They were able to fit the decay of local connectivity with distance using a Gaussian function of the following form, where the connection probability $p(x)$ scales with the cell separation $x - x_0$.

$$p(x) \sim e^{-(x-x_0)^2}$$

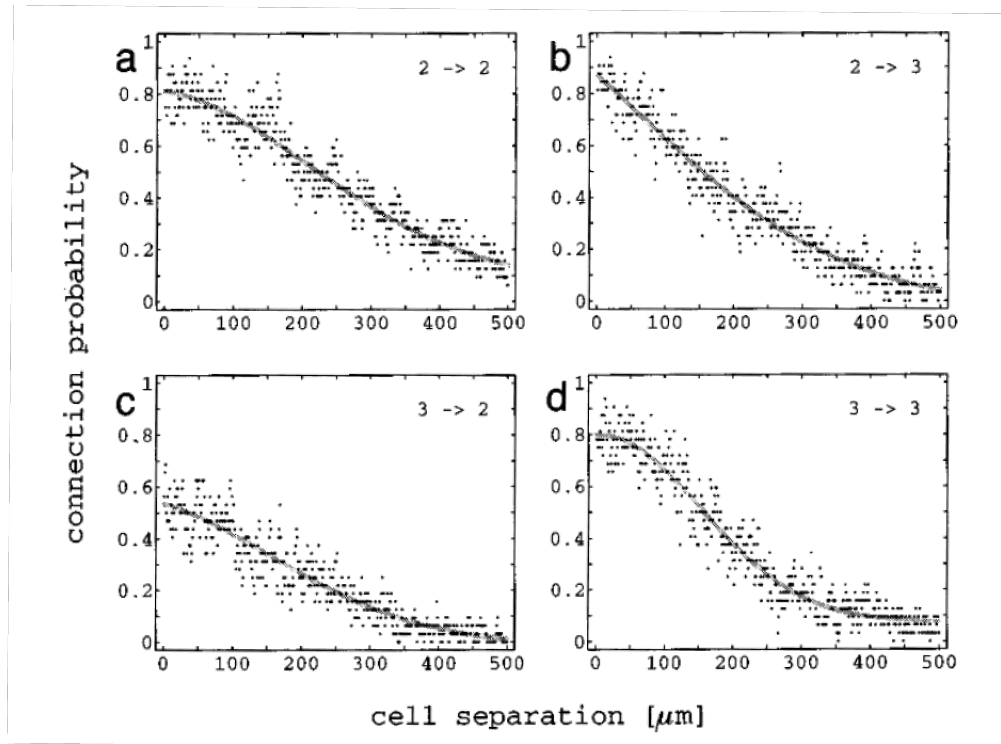


Figure 5. Local short range connection probability among neurons of different layers in the cortex (Note: Figure by Hellwig (2000), Fig. 7) **a**, The local connection probability between an axon of a layer-2 neuron and a dendrite of a layer-2 neuron (as indicated in the upper right corner) plotted against cell separation and fitted by a Gaussian function. **b**, Same plot for connections between axons of layer-2 to dendrites of layer-3. **c**, Axons of layer-3 to dendrites of layer-2. **d**, Axons of layer-3 to dendrites of layer-3.

Importantly, local connectivity seems to be attached to the framework of cortical columns, as it appears to be clustered (Hellwig (2000)), indicating that connections within a column are favoured. Fig. 5 showing the Gaussian fits of local connectivity underlines the clustering of local connectivity. Here, the data points for connection probability alternate from being located above and below the fitting curve as distance between neurons increases. This alternation indicates that connection probability stays constant as long as neurons are within the same column, dropping once the next column is reached.

The decay of global connectivity was found to be of exponential nature (Ercsey-Ravasz et al. (2013)). Monitoring weighed connectivity between different brain areas with the help of sensitive retrograde tracer experiments in macaque monkeys revealed an exponential decay in connectivity with distance between areas. The weight of a projection from a source to a target area is defined as the ratio between the number of labelled source area neurons and the

total number of neurons labelled in the entire cortex that are not a part of the target area.

3.1.3 Wiring optimisation

The layout of connections between neurons in the brain has to solve the pivotal problem of being as efficient as possible, while at the same time minimising wiring cost. Going to extremes on both aspects at the same time is not possible (Bullmore and Sporns (2012)), as indicated by Fig. 6. Minimal wiring cost would be achieved by neurons just being connected to their closest neighbours, which results in a network lacking any global long range connections. Short wires additionally allow for fast signal propagation. Efficient global information processing however, relies precisely on long range connections, which in turn drive wiring cost up. In other words, connectivity in the cortex is a delicate compromise, optimising both wiring cost and network efficiency to the extent that either factor does not fall utterly short. The brain therefore organises itself in a modular arrangement, where clusters of neighbouring information nodes tend to optimise wiring cost. Long range connections between different modules/areas are also included but are kept sparse in order to not blow wiring cost out of proportion (Bullmore and Sporns (2012)). A large proportion of wires in the brain is located in the white matter of the brain. The separation of white and grey matter seems to be an optimal solution when connecting many neurons via fast axons to minimise conduction delay (Wen and Chklovskii (2005)). Wen and Chklovskii (2005) show that the maximal size of a network that does not allow for conduction times longer than about one millisecond is close to the size of a cortical column.

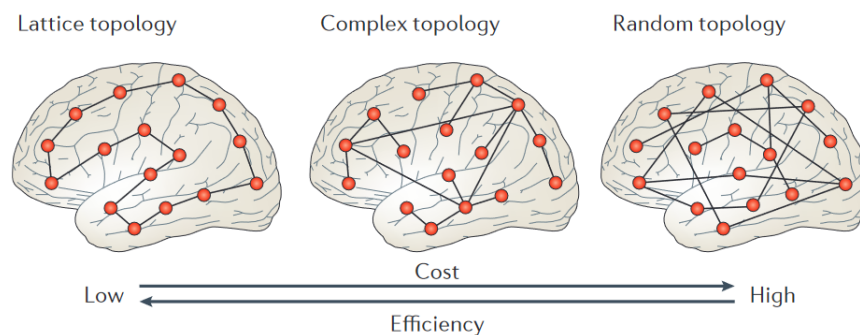


Figure 6. Network cost and efficiency

(Note: Figure by Bullmore and Sporns (2012), Box 1) Different types of networks optimise different aspects. Low cost networks with no global connection have low efficiency. Random connectivity with lots of global connections is costly but has high performance efficiency.

Therefore, all-to-all connection in the brain is not a viable option when considering conduction delays. Signal travel time could be reduced by increasing the axon diameter, yet this would result in a larger brain volume. With an increased volume, axons would have to be longer, increasing conduction delays.

Using the concept of wiring optimisation, computer models should be able to predict the optimal placement of neurons. Raj and Chen (2011) were able to show that nodes moving freely on a 3D surface that is topologically identical to the brain would arrange themselves similarly to the actual arrangement found in the brain when constrained by wiring optimisation. The connectivity between the nodes was kept identical to that observed in the brain. They conclude that the brains anatomy is a result of its connectivity demands and not the other way around. Inspired by this concept, Weigand et al. (2017) predicted the optimal placement of neurons via similarities. Two neurons are similar if they are interconnected and share a lot of connections to other neurons. The more similar two neurons are, the closer they are placed together. To test this basic concept, a random arrangement of neurons is set up in a square with each neuron being assigned to a horizontal area depending on its position (Fig. 7 left). The different areas are colour coded. A connection probability matrix is derived, based on the distances between neurons (Fig. 7 middle left). Neurons in close vicinity have a high connection probability dropping off rapidly with distance. The connection probability matrix is translated into a connection matrix (Fig. 7 middle right) which is then used to determine neuron similarities depending on their connections.

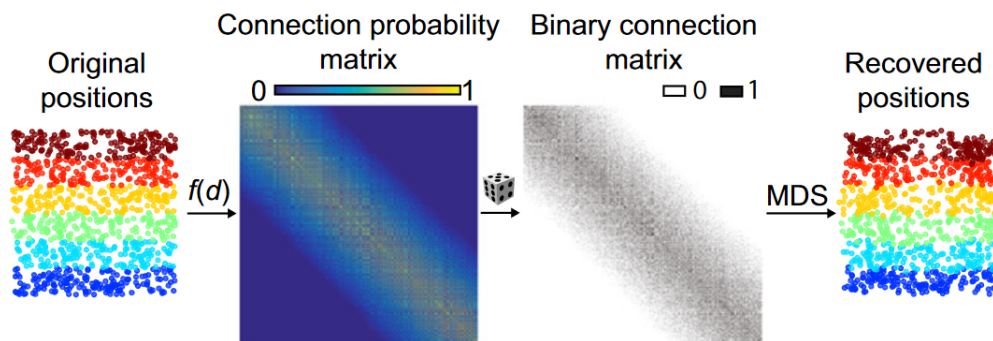


Figure 7. Dimension reduction methods can recover neuron positions based on connectivity

(Note: Figure by Weigand et al. (2017), Fig. 1 A) The original positions of neurons can be recovered based on a distance dependent connectivity function $f(d)$, using multi-dimensional scaling (MDS), a dimension reduction method. A connection probability matrix is calculated based on the distances between neurons. Neurons are then placed according to the binary connection matrix, connected ones in close vicinity, others further apart.

Since all neurons have many connections, this problem can be treated as a high dimensional data set. By using a dimension reduction algorithm (here multi-dimensional-scaling MDS (Borg and Groenen (2005))), neurons are placed in a 2D manifold, accurately reproducing the original input arrangement (Fig. 7 right). Depending on the nature of the connection probability function and the number of neurons involved, this method is capable of reproducing a transition from salt and pepper arrangements to a pinwheel for orientation selective neurons (Fig. 8). These neuron arrangements mimic the configurations in the rodent and cat visual cortex where neurons encode different object orientations in the visual field. Neurons that encode for similar or the same orientations are assumed to be more closely connected and share the same colour in Fig. 8. Rodents, with low numbers of neurons n when compared to the cat, exhibit random looking salt and pepper arrangements, while cats develop pinwheel structures. These findings show that anatomical features of the brain can be predicted by applying the proper connectivity amongst neurons and considering wiring optimisation. By realising a transition from the anatomy of one species to another when altering parameters, it is demonstrated that connectivity is indeed one of, if not the most prominent factor that determines brain anatomy.

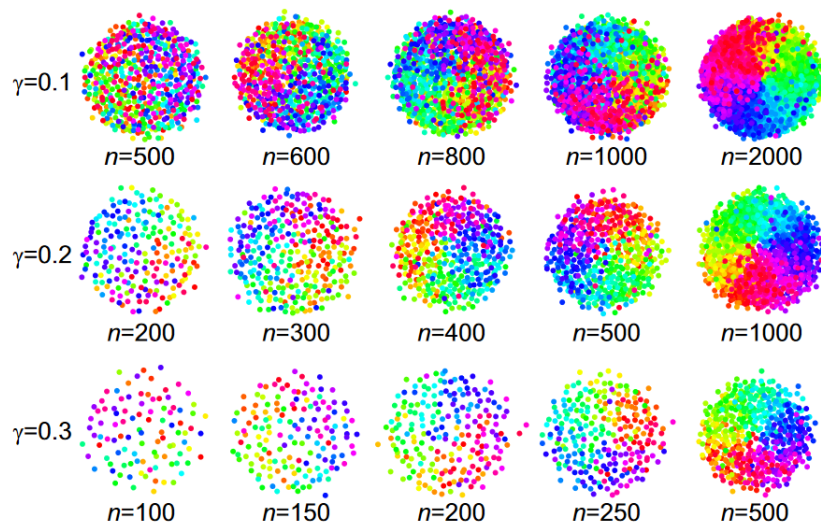


Figure 8. MDS predicts pinwheel arrangements of neurons found in the visual cortex

(Note: Figure by Weigand et al. (2017), Fig. 1 C) Neurons in the visual cortex encode for different object orientations (orientation preference), indicated by the colours. Using a connectivity function based on orientation preference similarity, MDS reproduces the transition from salt and pepper towards pinwheel arrangements with increasing numbers of neurons n , as found in the visual cortex of rodents and cats. γ is a parameter of the connectivity function that determines how selective neurons are with respect to orientation preference.

3.2 The Microscopic structure of the brain: Neuron reconstructions

3.2.1 Human neuron morphology reconstructions

The morphology of dendrites from many species has been the subject of research for a long time. These investigations have recently led to the emergence of computational models capable of growing artificial dendrites that are indistinguishable from real ones (Cuntz et al. (2010), Cuntz et al. (2007)). The reason neural dendrites are of such importance, is the fact that informational inputs from many other neurons arrive here. These inputs, which can be of inhibitory or excitatory nature, are integrated by the dendritic tree (London and Häusser (2005), Gullledge et al. (2005), Wen and Chklovskii (2005)). The geometric and structural properties of the dendrites are responsible for the way information is processed (Mainen and Sejnowski (1996)). Dendrite complexity heavily affects a neuron's firing properties as found by Zhu et al. (2016) and van Ooyen et al. (2002). In this study, cortical neurons were grown on polyolefine polymer (POP) stamps featuring a high resolution in a pattern specifically designed for that purpose as depicted in Fig. 9 A. Neurons grown in such a patterned structure exhibit differences in firing rate and neural excitability compared to un-patterned neurons. This is demonstrated in Fig. 9 B that showcases two example spike trains from an un-patterned and a patterned neuron. Despite the efforts of the past, investigating and analysing dendritic tree structure and electrophysiology of human neurons has proven to be a big challenge since reliable data of fully reconstructed 3D human neurons is in short supply (DeFelipe (2015)). The scarceness of human data is due to multiple aspects but the most obvious of them, and at the same time hardest hurdle to overcome, is that humans are very unlikely to surrender any of their healthy brain cells to the scientific community. The few data that are accessible are reconstructions from human patients with severe brain diseases, like for example, epilepsy or brain tumours, that are untreatable (Domínguez-Álvaro et al. (2018), Buchin et al. (2020)). Morphologies affected by such diseases exhibit changes in behaviour, causing intellectual disability alongside heavily impaired cognitive functionality (Shuman et al. (2017)), amongst other pathological changes. Hence, utilising such data to perform research on human neurons might result in inaccurate scientific conclusions that represent a neuron's functionality in its pathological and therefore not its healthy state. On top of that, reconstructing a neuron's morphology is a difficult procedure that is prone to error.

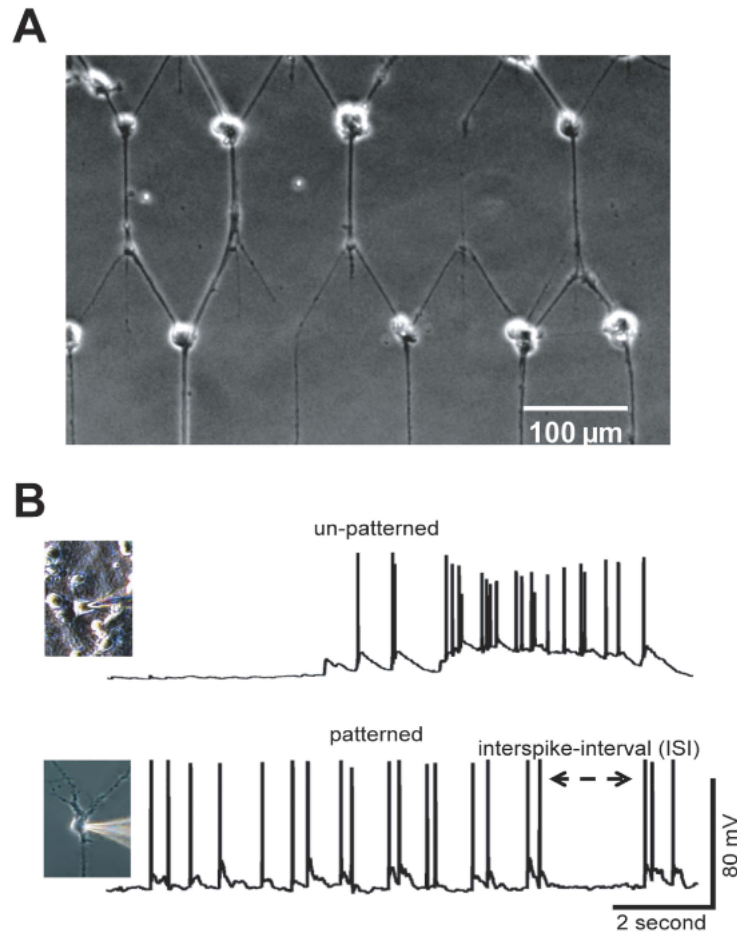


Figure 9. Neuron complexity affects spiking behaviour

(Note: Figure licensed by <https://creativecommons.org/licenses/by/4.0/>, figure by Zhu et al. (2016), Fig. 4 A and B) **A**, Patterned cortical neurons in an image of a phase contrast micrograph on a cover slip at DIV14. **B**, Whole cell patch mode recordings of spontaneous spike trains, in segments of 10s raw data with an example for un-patterned and patterned neurons.

Reconstructing a neuron's morphology successfully is dependent on many factors, such as the quality of the microscopic image stack the neuron is reconstructed from, or uncertainties that may arise when distal cell branches overlap. Cutting tissue to prepare for microscopic imaging inevitably leads to lesions in the delicate distal arbors of the dendrites. The staining agents injected into neurons to make their dendritic tree visible in the microscope image may not reach the furthest regions in the dendrite, which alongside tissue shrinkage and distortions (Horcholle-Bossavit et al. (2000), De Schutter and Jaeger (2000)), can make reconstruction very difficult. The resulting 3D reconstructions are oftentimes incomplete since part of the dendrites are missing, which inhibits our understanding of human neuron functionality.

While human neurons are poorly understood, research on neurons of rodents such as rats and mice has progressed rather well. Therefore, the question arises whether reconstructions of human neurons are actually needed since rodent morphologies may be sufficient. Studies of human morphologies in the recent past have revealed differences between human neurons and neurons of other species, regarding morphology and brain circuits (Benavides-Piccione et al. (2020), Mihaljevic et al. (2020), Schmidt and Polleux (2022)). Kötter and Feizelmeier (1998) showed that existing variations in morphological size between species result in recognisable differences in electrophysiological properties of neurons. They found that simply scaling the size of a neuron to turn a neuron from one species into a neuron from a different species is not enough to create constant activity patterns. Therefore, other mechanisms must exist which are able to compensate. Another recent study suggests that the capacitance of human neuron membranes is lower compared to other species (Eyal et al. (2016)). There also seem to be differences in the developmental stages of neurons, with human neurons exhibiting a longer prometaphase-metaphase than chimpanzees (Mora-Bermúdez et al. (2016)). Apparently, this is not true for non-neural cells, but only proliferating progenitors. These reasons emphasise how important it is to make data on human neuron morphologies more reliable, accurate and accessible. They are, however, just the tip of the iceberg when it comes to understanding how the human brain and its neurons differ from those of other species. Understanding the nature of these differences will enable us to implement more realistic computer simulations (Zhao and Bhattacharyya (2018)) and potentially even get to the bottom of the superiority of the human brain compared to other mammalian species.

3.2.2 Repairing neuron morphologies

To address the issue of the scarcity of human neuron morphology data, the second project in this thesis implements a repair algorithm. The repair tool is based on the TREES toolbox (Cuntz et al. (2010)), which is a model created to grow realistic artificial dendrites. The model uses optimal wiring principles to connect a number of carrier points to a root node (the soma), growing an artificial neuron. The TREES toolbox provides a simple solution to modelling different cell types via just one parameter called the balancing factor bf . A neuron needs to minimise conduction time in its dendrites, preferably using direct connections to the soma. This, however, comes at a considerably increased wiring cost, while opting for low wiring cost increases conduction time instead. The balancing factor introduced by Cuntz et al. (2010)

represents a compromise, tipping the balance between the two extremes, depending on the cell types specific needs. Fig. 10 illustrates how the bf impacts the shape of an artificial neuron, showing four different possibilities to connect the same set of carrier points (red) to the root node (black), with increasing bf . $bf = 0$ corresponds to a layout that minimises wiring cost, while $bf = 1$ minimises conduction time to the root. Different cell types can therefore be modelled by a single parameter. This goes to show that the constraints of optimal wiring are very relevant when it comes to explaining the macroscopic and the microscopic structure of the brain (compare **Chapter 3.1.3**). Indeed, wiring optimisation will be a key component for both models, the macroscopic gyrification model and the microscopic neuron repair tool, later in this thesis.

The repair algorithm will allow the user to complete any incomplete neuron morphology by adding artificial dendrites to the existing ones.

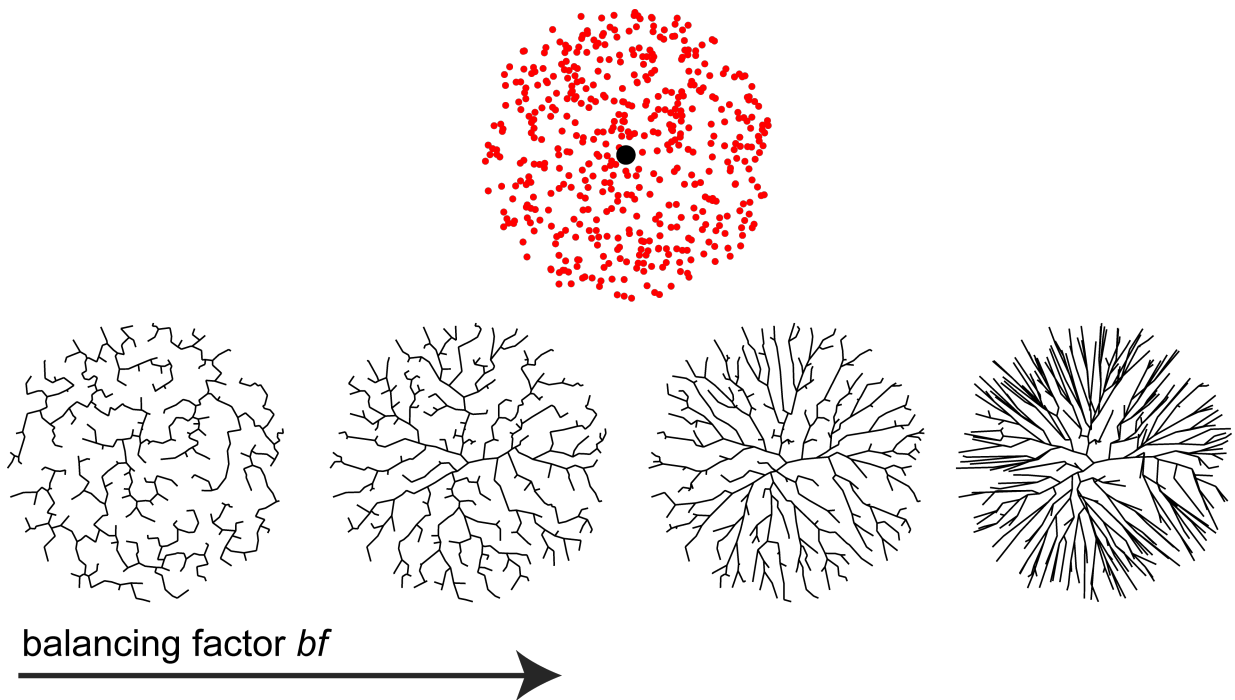


Figure 10. The dendrite growth algorithm based on optimal wiring finds the optimal trade-off between cable length and conduction delay

(Note: Figure by Cuntz et al. (2010), Fig. 2 B, redrawn by Moritz Groden) The impact of the balancing factor on artificially grown dendrites. The same set of carrier points (top, red points) is connected to the root node (top, black point). Depending on the balancing factor bf either wiring cost is minimised (low values of bf), or signal travel time to the root (high values of bf).

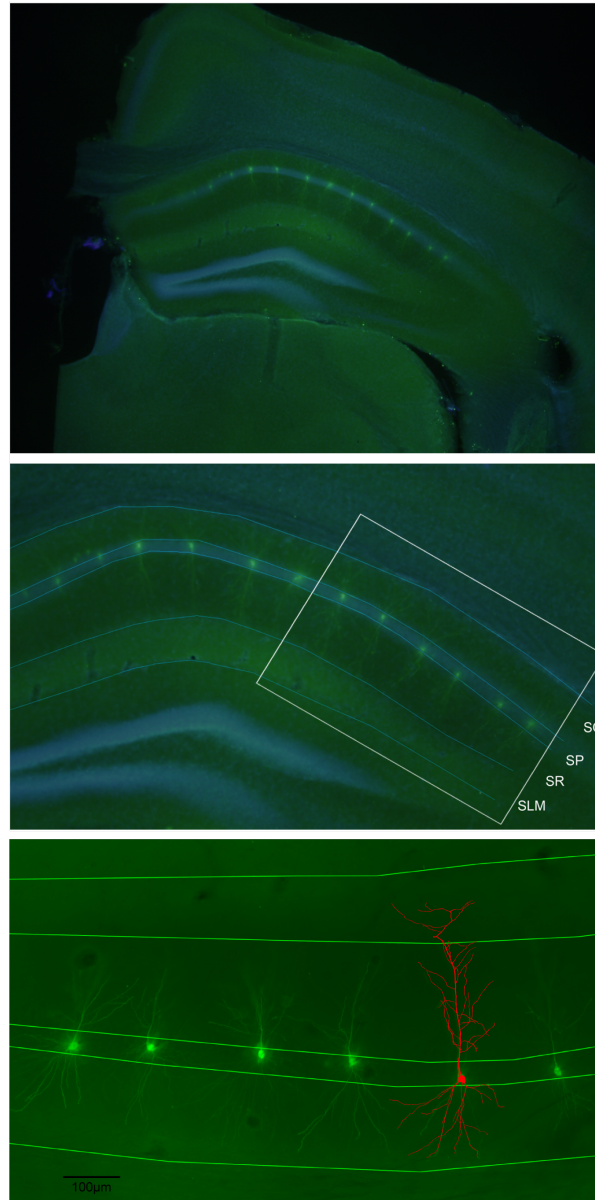


Figure 11. Microscope images of mouse CA1 data set

(Note: Images by Benavides-Piccione et al. (2020)) **Top:** Confocal microscope image of the mouse hippocampus with stained pyramidal neuron morphologies. **Middle:** Magnified image of the mouse CA1 region with region of interest. **Bottom:** Region of interest with one example pyramidal morphology reconstruction overlay in red.

For this purpose, new artificial dendrites are grown exclusively from the incomplete ends (severed ends) of the dendritic tree of the input neuron. The incomplete ends and their coordinates are specified in the morphology by the user. To validate the effectiveness of this approach, it will be tested on a set of CA1 pyramidal neuron reconstructions of the mouse, reconstructed by

Benavides-Piccione et al. (2020). Even though the goal of the algorithm is to repair incomplete human morphologies, they are not suitable candidates for the validation process. Mouse neurons have been studied far more intensively than human ones, not least because of the reasons mentioned in **Chapter 3.2.1**. Fig. 11 shows the microscopic images of the mouse pyramidal neuron reconstructions used to validate the repair tool. All reconstructions are taken from the mouse hippocampus, which is depicted in the top panel of Fig. 11 (images by Benavides-Piccione et al. (2020)). Specifically, neurons from the CA1 region (Fig. 11 middle) were reconstructed as indicated by the rectangular region of interest (ROI). The magnified ROI is depicted in Fig. 11 bottom, with an example overlay of a neuron reconstruction. In the validation process, neurons are cut intentionally in their apical and basal arbors. These intentionally cut versions of the pyramidal neurons are repaired using the repair algorithm to compare the repaired neurons to the original reconstructions. Morphological changes affect the electrophysiological properties of neurons, altering their firing response (Zhu et al. (2016)). A successful repair, should therefore, recover the original electrophysiological behaviour of a neuron, which will also be demonstrated in this thesis.

The neuron repair model can be applied to any cell type besides pyramidal neurons. The validation relies on pyramidal neurons since they are the most abundant in the cortex. Extrapolating the concept of the validated model, it will be applied to human neurons morphologies in this thesis.

3.2.3 Neuron biological regrowth

As mentioned earlier, changes in dendritic morphology can have an impact on neuron functionality. This has also been reported for brain disorders in the developmental stage such as Down's syndrome (Blanpied and Ehlers (2004), Penzes et al. (2011)) and after the brain was affected by trauma (Greenwood and Connolly (2007)). How dendrites regrow and regenerate after suffering such pathological conditions remains largely unclear. Bodmer and Jan (1987) have created a biological model using the multiple dendritic arborisation (da) neurons of the peripheral nervous system of *Drosophila* flies. These neurons are divided into four different groups depending on their dendritic pattern, called classes I-IV. Neurons of class IV grow on a two dimensional plane on the extracellular matrix secreted by the epidermis (Han et al. (2012)). The model of *Drosophila* was recently used to study regeneration in dendrites after dendriotomy by Song et al. (2012) and Stone et al. (2014). 98% of the class IV da neurons

proximal dendrites that were lesioned exhibited regeneration, which was measured by how much of the receptive field was covered after the lesion event. Interestingly, the lesioned dendrites displayed the all or nothing principle when it came to regeneration. This means that either a new dendrite grew that originated from the site of lesion, or the vacant area was filled by other invading branches from the neighbouring regions (Song et al. (2012)). Therefore, biological regrowth seems to follow a bimodal distribution between invasion and regeneration from the site of lesion.

The neuron repair algorithm introduced in this thesis aims to mimic biological regrowth. The method used for biological regrowth is identical to incomplete growth (growth from severed ends only), the only difference being that the algorithm is allowed to grow from any random point on the morphology in close vicinity. The algorithm is tested on reconstructions of class IV da neurons that were lesioned during experiments. The artificially regrown cells reproduce the same bimodal distribution found by Song et al. (2012).

4 Materials and methods

Custom code for both simulations, the gyrification model and the neuron dendrite repair tool, was written in MATLAB (MathWorks). Some of the excessively time-consuming calculations, especially the parameter scans for the gyrification model, were performed on the Neuroscience Gateway cluster (Sivagnanam et al. (2013)).

4.1 Gyrification model

4.1.1 Optimal placement

The method used to predict the optimal positions of neurons for the gyrification model is a variant of what has been used in recent studies, specifically by Weigand et al. (2017), who used oMDS (ordinal multidimensional scaling) (Borg and Groenen (2005)) to calculate the relative positions of neurons. The gyrification model uses t-SNE (t-distributed stochastic neighbour embedding) (van der Maaten and Hinton (2008)) rather than oMDS. According to the connection dissimilarities between neurons, t-SNE predicts the optimal placement of neurons. t-SNE was chosen due to its superior performance over oMDS (see Discussion **Chapter 6**). Calculating the connection dissimilarities differed from the approach taken by Weigand et al. (2017), who used the Jaccard distance. The connection dissimilarity between two connected neurons would be determined by the Jaccard distance between their respective connection vectors. In case of two unconnected neurons, the connection dissimilarity was calculated as the shortest path length separating these two neurons on the connected graph. The dissimilarities of connected neurons along this shortest path serve as a distance measure, which are added up. In this thesis, however, only the cosine distance between neuron connection vectors was used instead of the Jaccard distance along the shortest path. This is due to the cosine distance yielding similar results using less computational power. Hence, with a given connectivity matrix C , the positions of neurons X can be predicted by t-SNE, which uses the connection dissimilarity matrix D as an input. The dissimilarities are calculated in the following way, such that the pairwise cosine distances $cd_{k,l}$ between neuron k and l are contained in D :

$$cd_{k,l} = 1 - \frac{\mathbf{c}_k \cdot \mathbf{c}_l}{\|\mathbf{c}_k\| \|\mathbf{c}_l\|}$$

\mathbf{c}_k and \mathbf{c}_l are the connection vectors of neurons k and l . Therefore, k and l correspond to the matrix columns in the connectivity matrix \mathbf{C} . Any neuron positions predicted in \mathbf{X} represent the relative positions among the other neurons. Therefore, any folding arrangements calculated by this method have to be standardised to fit within a unit square.

4.1.2 Folding connectivity

By assigning neurons to a specific cortical column, the gyrification model replicates the connectivity in the cortex. Each cortical column is filled with neurons according to the parameter M , which is the number of neurons per column. The number of columns C determines the size of the cortex. Therefore, $N = C \cdot M$ is the total number of neurons in a folding arrangement. Since any neuron $N_k \rightarrow C_i$ is assigned to a column C_i , the distances between neurons correspond to the distances between columns. The distance between any two columns C_i and C_j is defined as the cyclical topological distance $\Delta C_{i,j}$ as follows:

$$\Delta C_{i,j} := \begin{cases} \frac{C}{2} - (d - \frac{C}{2}) & \text{if } d > \frac{C}{2} \\ -d & \text{if } -\frac{C}{2} < d \leq \frac{C}{2} \\ -\frac{C}{2} - (d + \frac{C}{2}) & \text{if } d \leq -\frac{C}{2} \end{cases}$$

Here, $d = i - j$ is the difference between the two column indices. This topological distance between cortical columns is the setup for the connection probability function between two neurons N_k and N_l , with the corresponding connection probability $p_{k,l}$. As mentioned earlier, since neurons are assigned to columns, with $N_k \rightarrow C_i$ and $N_l \rightarrow C_j$, the connection probability function is based on the topological distance between the respective columns $\Delta C_{i,j}$.

$$p_{k,l} = a \left(\frac{\cos(\Delta C_{ij} \cdot \pi/C) + 1}{2} \right)^\gamma + (b - a) \cdot \exp \left(-\frac{(\Delta C_{ij} \cdot \pi/C)^4}{2\pi\sigma/C^4 \cdot 10^6} \right) \quad (1)$$

The first part of the equation models global long range connectivity using a broad cosine function with its strength determined by a . The exponent γ regulates the decay rate of global connectivity. The second part of the equation represents local close range connectivity with its strength equal to b , implemented by a rapidly decaying Gaussian function. The width of local connectivity is determined by σ . Folding in the model relies on strong local and weak global connectivity, meaning that b usually takes larger values than a , with $a \approx 0.3$ and $b \approx 1$. Importantly, since a and b correspond to probabilities, they have to fulfil the following conditions:

$$0 \leq a \leq 1 \text{ and } 0 \leq b \leq 1$$

To ensure the cyclic nature of the connection probability (Eqn. 1) regardless of the number of columns, the topological distance between the two columns ΔC_{ij} is multiplied by π/C . The same is true for σ , which is multiplied by $2\pi/C^4$, ensuring the width of local connectivity always spans the same number of columns regardless of the value of C , unless the value of σ is changed. To produce the connection matrix C , random values of one or zero representing the neuron connections $c_{k,l}$ are calculated based on the connection probabilities $p_{k,l}$. Containing the pairwise connections $c_{k,l}$, the connection matrix C is then used as an input to the neuronal placement algorithm to determine connection dissimilarities as described earlier. The folding pattern arrangement is predicted based on these dissimilarities.

4.1.3 The folding index

The most important measure to quantify the morphological properties of a folding pattern is the folding index FI . In order to calculate FI , the exposed circumference A_E (which is equal to the convex hull) is compared to the total circumference A_T (which is equal to the boundary).

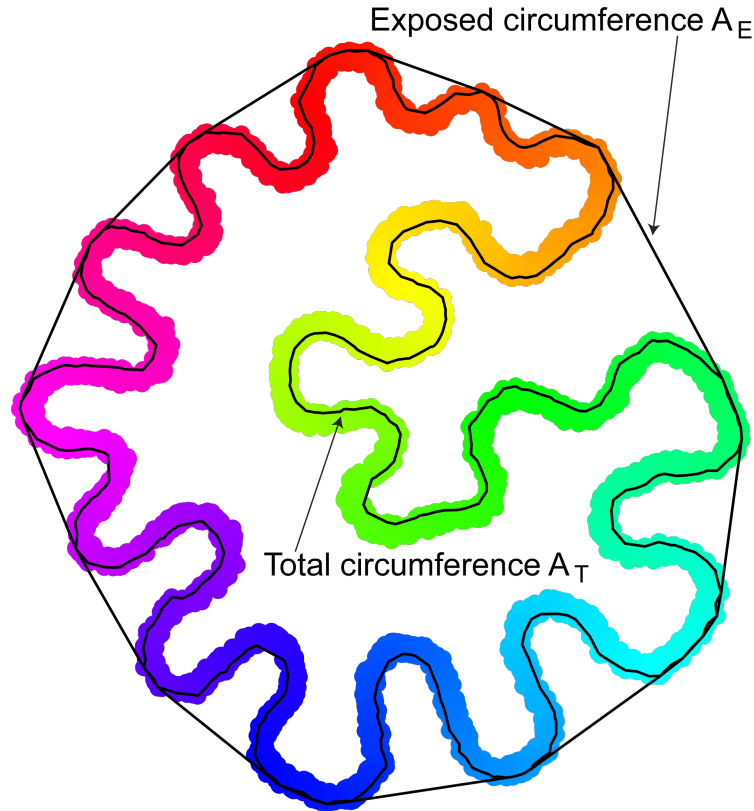


Figure 12. Total and exposed circumference

Example of the total and exposed circumference of a folding pattern.

The boundary as well as the convex hull are calculated using build-in functions of MATLAB, *boundary* and *convhull* respectively, as depicted in Fig. 12. The boundary (total circumference) fits tightly around the folding pattern while the convex hull (exposed circumference) envelops its rough area. Using these MATLAB functions, when applied to a set of 2D data points, yields the circumferences A_E and A_T , which in turn can be used to estimate the area H the data set occupies. In case of a folding pattern, the number of neurons N and their coordinates represent the set of 2D data points. If a formation is not convex, the convex hull leads to a false approximation of both the actual circumference (same as the total circumference A_T) and the area H . H is overestimated, while the actual circumference is underestimated, leading to $A_E < A_T$ for non-convex shapes.

The boundary function is based on the principle of α -shapes (Akkiraju et al. (1995)). α -shapes are composed of a set of curves K_α . Using only one parameter $\alpha \in [0, \infty]$ to characterise them, the curves K_α are built around the points of the data set (here N). K_0 represents the set of points N itself, whereas K_∞ is equal to the convex hull. With a set of points that is

usually finite, the set of curves K_α is also finite and is constructed in such a way that α_m takes the highest and α_1 the lowest value of α . In case of α_1 , K_{α_1} is the continuously connected graph of all the points contained in N , the finite set of points. For the largest α , which is α_m , $K_{\alpha_m} = K_\infty$. By finding all possible values of α , with $\alpha_1 < \alpha < \alpha_m$, the MATLAB function *boundary* calculates the unique curves. To select a specific α -value, the function implements a shrink factor \mathcal{F} called the boundary parameter. Setting $\mathcal{F} = 0$ produces the convex hull, whereas the tightest possible boundary corresponds to $\mathcal{F} = 1$. Since the perimeter of a folding pattern can exhibit small gaps of varying size, choosing a boundary parameter too high can cause the boundary to penetrate these gaps wrapping around the inside of the folding pattern as well as the outside. The resulting value for the total circumference A_T is way too large. To avoid this issue, but still get an accurate value for A_T , the boundary parameter was set to 0.9. This way, the boundary is still able to follow the outer contours of the folding pattern accurately while not penetrating small gaps. Once A_T and A_E have been determined, FI can be calculated by comparing them as follows:

$$FI = \frac{A_T}{A_E}$$

4.1.4 Fractal dimension

The fractal dimension is a measure to quantify how space-filling a self similar pattern is. A folding pattern takes the shape of a one-dimensional line that consists of neurons. The one-dimensional line gives rise to the gyri and sulci, that lie in a 2D-plane. Suppose the 1D line fills the entire 2D plane with its convolutions, its fractal dimension D would be equal to two, since it effectively is a two-dimensional object. The less space-filling the line, the lower D , down to a value of one, which would correspond to a straight line. A fractal dimension of two for a convoluted 1D line is a hypothetical value. In reality, D would approach two but never reach it. To determine the fractal dimension D of a folding pattern, the box counting algorithm was applied (Liu et al. (2003), Mandelbrot (1983), Kalmanti and Maris (2007)). Applying the box counting method requires a pixel image of the boundary (total circumference, see Materials and methods **Chapter 4.1.3**) of a folding pattern. The boundary in the image has to be no wider than one pixel. In a first step to achieve this, the build in MATLAB function

poly2mask is applied to the boundary of the folding pattern, yielding a 1000×1000 binary matrix **B**. In conjunction with the MATLAB morphological operator *bwmorph('remove')*, **B** now represents a rasterized pixel image of the boundary with 1-pixel-width. With the help of the build-in MATLAB function *boxcount*, the fractal dimension of the folding pattern boundary can be estimated. The *boxcount* algorithm computes how many squares s it takes to cover the pixel image of the folding pattern perimeter. s varies depending on the side length l of the squares. The variation in s can be characterised by the following power law:

$$s = g \cdot l^{-D}$$

Here, D is the fractal dimension and g is a constant. The set of points given by $\log(l)$ and $\log(s)$ is then fitted by a line, such that its positive gradient is an estimate for D (Kalmanti and Maris (2007), Falconer (2004))(Fig. 19 middle, Fig. 23 B).

4.1.5 Fold frequency and Amplitude

In order to analyse the spatial folding frequencies and amplitudes of a folding pattern, a projection of its radial shape on a horizontal graph is required. The horizontal graph is a projection of the folding pattern boundary's radial amplitude plotted against the column index C_i (boundary is equal to the total circumference, see Materials and methods **Chapter 4.1.3**). The radial amplitude is given by the Euclidean distance from the outer perimeter (the boundary) of a folding pattern to its centre of mass as depicted in Fig. 13. It shows the original folding pattern on the left and the corresponding graph on the right. Since the points on the boundary are not equally spaced with respect to the column index, the data points were fitted using a smoothing spline from the build-in MATLAB *fit* function. The smoothing spline fit is represented in Fig. 13 by the black line. After sampling the fit to obtain equally spaced data points, the fast Fourier transform function in MATLAB *FFT* is applied yielding the spatial frequency spectrum of the gyrification layout. The data is sampled into frequency bins, as there is no time component in the spatial frequencies of a folding pattern (see Fig. 19 right, Fig. 23 B bottom). The intensity of a frequency bin is given by the colour code next to the graph.

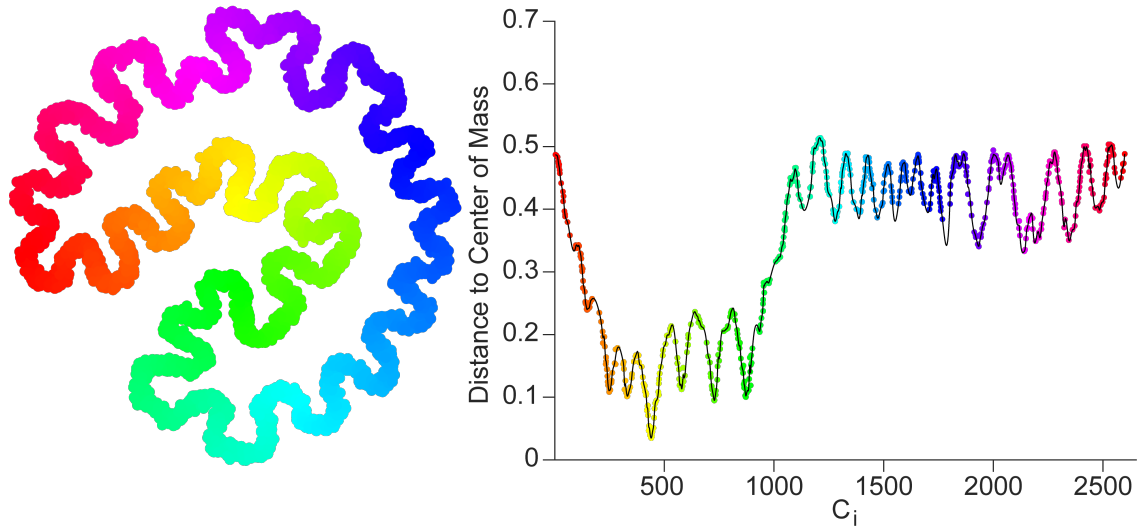


Figure 13. Horizontal projection of a folding pattern boundary

Example of a horizontal projection of the tight boundary of a folding pattern. The amplitude of gyri and sulci are measured from the centre of mass to the outer perimeter of the folding pattern.

Since the frequency spectrum would otherwise be dominated by the high power values of low frequencies in the folding pattern due to their large amplitudes, a cut off limit was introduced in the colour code. Without such a cut off limit, peaks of higher frequencies would not be visible despite their higher occurrence. This is because of their significantly lower amplitude. In case of a folding pattern, a frequency of one would signify a convolution spanning the entirety of the folding pattern perimeter. Next to calculating the frequency spectrum, the smoothing spline fit is also used to analyse the mean amplitude of folds in a folding pattern. This can be done by applying the *findpeaks* function in MATLAB to the sampled fit.

4.1.6 Discarding degenerate folding patterns automatically

The optimal placement method used in the gyrification model does not always predict folding patterns that feature a continuous ring-like shape as expected for a cortex. Such results, as mentioned in **Chapter 5.2**, are referred to as degenerate (Fig. 17) since they cross themselves or are discontinuous. Any degenerate result was automatically discarded and therefore excluded from all analyses. A folding pattern counts as non-degenerate if it features a closed ring like-shape. With a cyclical connectivity, this expectation is reasonable. The algorithm built to judge whether a folding pattern is degenerate and should be discarded, relies on a directed

graph $G = (V, E)$. E represents the graphs edges, whereas V the graphs nodes.

$$V = \{k : k \in \{1, \dots, N\}\} \quad (2)$$

$$E = \left\{ (k, l) : \Delta C_{ij} > 0 \wedge \|\mathbf{x}_k - \mathbf{x}_l\| < 2 \cdot \max_{u \in \{1, \dots, N\}} \left(\min_{m \in \{1, \dots, N\} \setminus \{u\}} (\|\mathbf{x}_u - \mathbf{x}_m\|) \right) \right\} \quad (3)$$

As neurons are assigned to cortical columns such that $N_k \rightarrow C_i$ and $N_l \rightarrow C_j$, ΔC_{ij} is the difference in column index between neurons k and l . The coordinates of the locations for neurons k and l are given by the vectors \mathbf{x}_k and \mathbf{x}_l . Applying the definition from Eqn. 2 and 3 the directed graph will only form a connection between the neurons N_k and N_l if the topological distance between their respective cortical columns C_i and C_j is positive. Furthermore, the neurons N_k and N_l must not be further apart from one another than double the maximum of all minimum Euclidean distances from neuron to neuron in order for a connection to be formed. In other words, for each neuron the distance to its closest neighbour is calculated. Taking the maximum of these distances and multiplying by two yields the maximum distance two neurons can be apart for the directed graph to form a connection and therefore counting as non degenerate. This procedure avoids the formation of local circles in the directed graph. Accordingly, the directed graph can only be cyclical if the folding pattern layout takes the shape of a closed continuous loop. The *isdag* function in MATLAB can be used to test whether a graph is cyclical or not. Based on the result of the *isdag* function the algorithm decides whether a folding pattern produced by the model is valid or degenerate. Folding pattern results where the boundary was able to penetrate a small gap in the folding pattern perimeter, were excluded from analyses as well. Some arrangements discussed in this thesis feature many nuclei instead of a ring-like cortex (see Fig. 15 B, Fig. 43 right). Such results were selected separately, since the directed graph criteria does not apply here.

4.2 Neuron dendrite repair tool

4.2.1 The *fix_tree* function

The neuron repair tool is implemented as a graphical-user-interface (GUI), built with custom code in MATLAB. The GUI calls upon the *fix_tree* function, which is the primary repair algorithm that is based on the TREES toolbox (Cuntz et al. (2010)), specifically the minimum spanning tree function (*MST_tree*). The neuron repair tool (GUI in conjunction with the *fix_tree* function) is used in this thesis to regrow and repair lesioned proximal dendrites of CA1 mouse and human pyramidal neurons. The missing dendritic branches in a target area are regrown and repaired, comparing the statistical properties of length, size (total cable length, mean path length per segment, mean diameter per segment) and complexity (number of branch points, Sholl intersection distribution). These properties are analysed and compared before and after the repair. On top of that, the electrophysiological firing behaviour is analysed for different morphologies using T2N (Beining et al. (2017)).

In the TREES toolbox, neurons are modelled as trees, which are a representation of their morphology. The morphology is considered as a directed graph between a set of nodes (carrier points) with a so-called adjacency matrix that specifies the connections between the nodes. By re-sampling the morphology, new nodes are added or removed such that the Euclidean distance between two consecutive nodes is the same for all nodes. This procedure does not alter the morphology as long as the sampling resolution is not too low. With a resolution of $1\mu\text{m}$ for example, the distance between neighbouring nodes is equal to $1\mu\text{m}$. The *fix_tree* function grows new artificial dendrites (repair dendrites) into a growth area/volume V that is passed to the function as an input. The coordinates for V can be drawn with the cursor using the GUI. V can be any set of arbitrary 2D or 3D points that is uploaded or drawn with the cursor, with the volume being determined by the *boundary* function in MATLAB. The *boundary* function uses α -shapes (Akkiraju et al. (1995)) to calculate the perimeter of any set of points, with the tightness of the fit being defined by the parameter α . $\alpha = 0$ corresponds to the convex hull, whereas $\alpha = 1$ corresponds to the tightest boundary. Carrier points are distributed within V according to the density profile of the branch and termination points in the dendritic spanning field of the input neuron that is supposed to be repaired. The clustering of the density profile is approximated via a Monte Carlo approach (unpublished by Laura Anton, available in the TREES toolbox), with the carrier points being distributed accordingly.

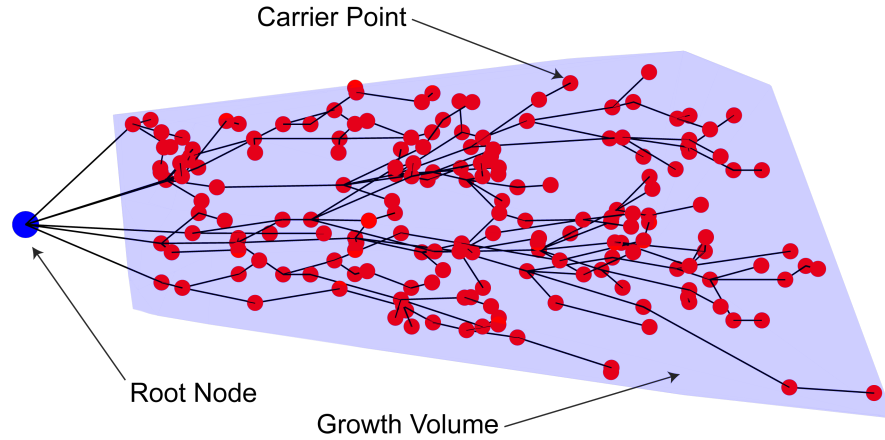


Figure 14. MST growing into distributed carrier points

Example of how the *MST_tree* function of the TREES toolbox successively connects a set of carrier points (red) distributed in a growth volume (blue shaded area) to a root node (blue).

To determine the number of carrier points N_{pts} , the density of the branch points in the input neuron as well as the size of V is evaluated. The artificial repair dendrites now grow into the distributed carrier points, which are successively connected to the morphology of the input neuron by the *MST_tree* function. This is demonstrated in Fig. 14, for a number of carrier points in red being connected to a single root node in blue. In the repair algorithm, the carrier points are connected to the existing dendrites of the input morphology instead. A connection is determined via a cost function that is defined by a single parameter, the balancing factor bf (Cuntz et al. (2010)). The cost function consists of the signal conduction time to the root node or soma (path length cost) and the material cost (wiring cost). The algorithm minimises the cost function for each connection with bf tipping the balance in favour of wiring cost or path length cost.

$$totalcost = wiringcost + bf \cdot pathlengthcost$$

bf is automatically estimated by the repair tool based on the input morphology using the *bf_tree* function of the TREES toolbox. The *bf_tree* function analyses the root angle distribution of the neuron as introduced by Bird and Cuntz (2019). Any single new connection to a carrier point formed by the algorithm is not allowed to span a distance larger than the growth threshold G_{thr} . G_{thr} is determined by measuring the length of the part of a line m that lies

within V . m passes through the coordinates of the root node R (soma) and the point that is located between the mean volume coordinate V_{mean} and the coordinate of the volume V that is furthest from the root node V_{far} . Therefore m is determined by:

$$Q = mean(V_{mean}, V_{far})$$

$$m = \left\{ \vec{x} = \vec{OR} + t \cdot \vec{RQ} \mid \vec{x} \in V \right\}$$

Any value for t is chosen in such a way that the line m is located within the growth volume V . With the first of the two growth modes available in the neuron repair tool, new artificial dendrites can grow from any point on the original input morphology that is not further away than G_{thr} . This mode is called biological growth mode, since new dendrites grow as if the living neuron would regenerate lost dendritic material. The second growth mode is meant to repair a section of the dendritic arbor that is known to exist but could not be reconstructed. For this purpose, the algorithm allows new dendrites to grow exclusively from incomplete terminals of neuron branches that have been severed (incomplete growth). The input neuron morphology file has to specify these incomplete terminals by stating their exact coordinates. Incomplete terminals that are located too far away from the growth volume V are not considered for growth, with the maximum distance allowed depending on the size of the input morphology. The incomplete growth mode has an additional option called main growth, which is designated to the repair of the apical dendritic arbor of pyramidal neurons. Pyramidal neurons feature one or more prominent main dendrites in their apical region (Benavides-Piccione et al. (2020)), which grow approximately in a straight line away from the soma of the neuron. Engaging the main growth option causes the algorithm to identify the thickest incomplete terminals when compared to all incomplete terminals. Main apical dendrites are then grown from these selected incomplete terminals radially outwards towards approximately 95% of the outer end of the growth volume V . The length and general directions of the main apical dendrites are estimated by the line m , that serves as a template, with any excess material that ends up outside of V being pruned. After main growth is completed, the growth procedure resumes as before, with the only difference that artificial repair dendrites can branch off the newly added main dendrite sections.

If existent, a reference morphology can be uploaded to the repair algorithm in addition to

the input neuron. The reference neuron serves as a statistical template, with the algorithm matching the number of branch points NBr of the repaired neuron to NBr determined by analysing the reference neuron. In case no reference neuron is uploaded, the desired number of branch points can be chosen manually (desired NBr has to be larger than NBr of the input neuron). The matching process is implemented by iterating over the growth process while successively adding more carrier points until the repaired morphology reaches the desired number of branch points. After matching the number of branch points to the reference or a manually chosen value, the algorithm can optionally adjust the total dendritic length of the repaired neuron to match the reference or a chosen value. This is done by pruning any excess dendritic material. To match the appearance of the artificial dendrites to the existing input morphology, the original part of the neuron is left untouched while the repaired dendrites are edited. Adding a quadratic taper, the dendritic diameter of the repaired dendrites is adjusted following the approach by (Bird and Cuntz (2016)). A spatial jitter is imposed upon the dendrite coordinates using low pass filtered spatial noise to make the dendrites resemble the appearance of their biological counterparts.

The parameters that determine the morphology of the repair dendrites can be adjusted manually as well, instead of being automatically estimated by the algorithm. The *fix_tree* function introduced here can be used via a custom build GUI as mentioned before, that will be available within the TREES toolbox. The GUI is based on the GUIDE MATLAB environment featuring a custom designed interface (see Fig. 28). The GUI is compatible with any 2D or 3D morphology reconstruction, as well as microscope image stacks that serve as background images.

4.2.2 (T2N) Electrophysiological properties

To test whether the electrophysiological firing behaviour of a neuron that has been sectioned can be recovered using the neuron repair tool described in this thesis, a compartmental model was used to perform somatic current clamps. These in silico current clamp experiments were performed using the T2N software interface designed by Beining et al. (2017) in MATLAB. T2N links the compartmental modelling package NEURON (Carnevale and Hines (2006)) to the TREES toolbox. The T2N software can be used to create or implement already existing complex electrophysiology models, many of which are accessible via the website <https://senselab.med.yale.edu/modeldb> (McDougal et al. (2017)). A morphology reconstruction in

the TREES toolbox format can be outfitted with passive and active ion channels, as specified by the used compartmental model using T2N. The model of choice for the testing of the neuron repair tool is a compartmental model by Jarsky et al. (2005), which was originally implemented to examine distal synaptic inputs in CA1 pyramidal neurons, which is fitting, since most neuron reconstructions lack dendritic material in the tuft region that can be repaired with the repair algorithm. Four active voltage channels (conductances) are included in the model by Jarsky. The first channel is a voltage-gated Na⁺ channel followed by a delayed rectifier K⁺ channel. Featuring an increased half-inactivation voltage the model incorporates a distal A-type K⁺ channel and lastly a proximal A-type K⁺ channel. The distribution of the ion channels mentioned above along the dendrites is modelled according to function of the direct path length to the soma. In case of the delayed rectifier K⁺ and the Na⁺ channels the compartmental model by Jarsky et al. (2005) features a version with weak excitability that follows a uniform distribution. As reported by experiments the A-type K⁺ current was increased by a factor of six along the apical dendrites in the model. The result of this current increase creates variable slopes for different morphologies that increase linearly between soma and tuft. The borders to divide the apical trunk of the dendrite were set in the following fashion: 3.14% of the dendritic arbor defined as the proximal apical, 36.27% as the medial apical, 68.90% as the distal and 100% as the tuft. The compartmentalisation of the dendrite was performed at path distances of approximately 100 μ m, 300 μ m and 500 μ m.

The in silico current clamp experiments consisted of somatic current injections of ramping intensity for both mouse and human morphologies. Each injection lasts for 500ms, as they are being performed for the reference, the repaired and the artificially cut morphologies. The firing behaviours of these three versions of the same neuron are then compared to show how damage and repair influence the resulting voltage traces. Ultimately, these simulations show that the electrophysiological properties of a damaged neuron can be recovered using the neuron repair tool.

The passive electrophysiological properties of the human dentate gyrus granule cells (GCs), provided by Buchin et al. (2020), were extracted from whole cell patch clamp recordings. The data was obtained from acute brain slices that were resected from epilepsy patients during surgery. Fig. 36 in **Chapter 5.3.4** depicts an example morphology on the top left, with the different dendritic regions marked by the colour code. The patch clamp recordings are taken from 24 different morphologies by injecting a rectangular current pulse at the soma and measuring the evoked voltage trace (example trace shown in Fig. 36 top right). The spine densities

and Wyler grades were measured for 6 out of the 24 morphologies. All measurements were performed by Buchin et al. (2020). The input resistance R_{in} , the membrane time constant T_m and the membrane resting potential V_{rest} , were calculated by analysing the recorded voltage traces. To ensure that only the passive response of the neuron is analysed, exclusively voltage traces with a small negative current injection were used for further analyses. This is done to prevent any active channels being involved in the neuron's response.

V_{rest} can be estimated by performing a linear fit of the voltage trace before the current pulse is injected. Since the exact time stamps of the start and stop of the current injection are given, the voltage trace can be cut accordingly. Averaging over the results for different voltage traces yields V_{rest} . To determine R_{in} , the voltage deflection from the resting membrane potential when current is injected must be calculated. The deflection is equal to the difference between V_{rest} of the specific trace and the voltage U after the current has been injected. U can be determined by performing a linear fit on the part of the voltage trace after current injection begins and before it ends. Repeating this procedure for multiple voltage traces with different injection currents I yields R_{in} according to Ohm's law $U = R \cdot I$. Therefore $R = U/I$, which means that the slope of a linear fit through the data points of U plotted against I gives R_{in} . To determine T_m one simply tracks the time it takes for the membrane potential to reach $1 - e^{-1}$ of its resting potential V_{rest} , after the current injection and therefore hyperpolarization stops. Repeating this procedure for every voltage trace and taking the average yields T_m .

To determine the axial resistance R_a and the membrane conductance G_m , a steady state simulation was performed using the `sse_tree` function of the TREES toolbox. The function estimates the input resistance R_{in} based on the input values R_a and G_m . Since R_{in} has already been extracted from the voltage traces as described earlier, proper values for R_a and G_m reproduce R_{in} plus minus two standard deviations. Fig. 36 in **Chapter 5.3.4** shows a visualisation of the procedure on the bottom. To account for the lack of spines in the GC morphologies, the simulation is carried out two times. First for the original morphologies without any changes and secondly after adding artificial spines to the morphologies using the `spines_tree` function of the TREES toolbox. Since the spine densities were only recorded for 6 morphologies, artificial spines could only be added for these 6. The densities were measured at two points for each morphology by Buchin et al. (2020). The first measurement was performed close to the soma and the second on the most distal ends of the dendrites. To add artificial spines to the entire dendritic tree apart from the soma, the spine density was extrapolated stepwise between the two points where the measurements were made. Spine sizes were modelled according to the

measurements on human cortical pyramidal cells by Eyal et al. (2018), due to the lack of spine data for human dentate granule cells. Using the simulated values for G_m and the membrane time constant T_m , the membrane capacitance was calculated as follows.

$$C_m = \frac{T_m}{R_m}$$

5 Research and results

5.1 The scope of this thesis: Optimal wiring-based macroscopic and microscopic models of the nervous system

1. Macroscopic model of cortical folding: Brain functionality is governed by the laws of physics, which we can implement in computer simulations in an attempt to make them resemble reality as closely as possible. The closer we get, the better we can understand how the brain and its neurons function and even predict how neurons and the brain grow and connect. For this approach to work, dividing the problem into smaller chunks is helpful, as it reduces complexity. In case of this thesis, two computer simulations were built, one focusing on the macroscopic, the other on the microscopic structure of the brain.

The macroscopic simulation is capable of reproducing the folding patterns of the mammalian cortex. The algorithm is based only on wiring optimisation and neuron connectivity and therefore provides a simple explanation as to why gyrification emerges. The transition from brains with no folds (lissencephalic), found in small mammals such as rodents, to highly convoluted cortices, as found in whales and humans, is easily realised by adjusting parameters. The change of gyrification observed in pathological diseases such as autism is reproduced, as parameters can be adjusted section wise. The model also predicts different scaling of gyrification among different orders of species. The algorithm therefore explains a lot of different phenomena using a simple approach on the macroscopic scale, while neglecting a lot of microscopic detail. In a future attempt to build an artificial brain, the model could be used as a framework that provides the large anatomical architecture. Microscopic details could then be embedded into this framework, piece by piece moving closer to a full computational model of the brain.

2. Microscopic model of nerve cell's anatomy: A lot of detail is required to understand the microscopic components of the brain. While a lot of data and research exists on neurons and their morphologies of small mammals such as rodents and even small monkeys, data on human neurons is sparse. As the ultimate goal of neuroscience is to understand how the human brain works and what makes it superior, we first need to improve availability and usability of human neuron data sets. Therefore, this thesis introduces a graphical user interface capable of repairing damaged morphology reconstructions of any neuron. As reconstructing

neuron morphologies from resected tissue is a delicate process, errors occur frequently. The model can repair microscopic parts of dendrites by adding artificial ones in any area the user chooses. By adjusting one parameter, different types of neurons can be repaired with ease. A repair restores the electrophysiological behaviour of a damaged neuron, as will be demonstrated in this thesis, which can be severely impaired when dendrites are cut or missing. Due to damage, dendrites of neuron reconstructions might appear to not reach layers and areas they normally do reach since important axonal input arrives there. This can lead to false scientific conclusions. The tool was built to relieve these problems and improve the size and availability of human morphology data sets, so the scientific community can develop better and better models of the human brain.

5.2 Macroscopic modelling: A computational model of gyrification

The gyrification model introduced in this thesis is based on two simple principles:

1. Neuron placement follows wiring optimisation requirements.
2. Local connectivity between neurons is strong while global/long range connectivity is sparse as found in the mammalian cortex (Hellwig (2000), Kaiser et al. (2009), Ercsey-Ravasz et al. (2013)).

The algorithm predicts neural placement by analysing pairwise connection dissimilarities between neurons. Therefore, a neuron's relative position to all other neurons depends on connectivity. In conjunction with connection dissimilarities, t-SNE (t-distributed stochastic neighbour embedding) (van der Maaten and Hinton (2008)), a dimension reduction method, is used for optimal placement (see Materials and methods **Chapter 4**), placing neurons that share a lot of connections in close vicinity, spatially separating those that do not. To establish strong local and sparse long range connectivity, neurons in the model are grouped into columns. These correspond to cortical mini columns, which have been observed to feature strong connectivity among their neurons (Sporns et al. (2005), Mountcastle (1997), Buxhoeveden and Casanova (2002)). Columns can be regarded as a small area on the cortex since they span the six layers of the cortex vertically. Therefore, two key parameters in the model are the number of columns C and the number of neurons N .

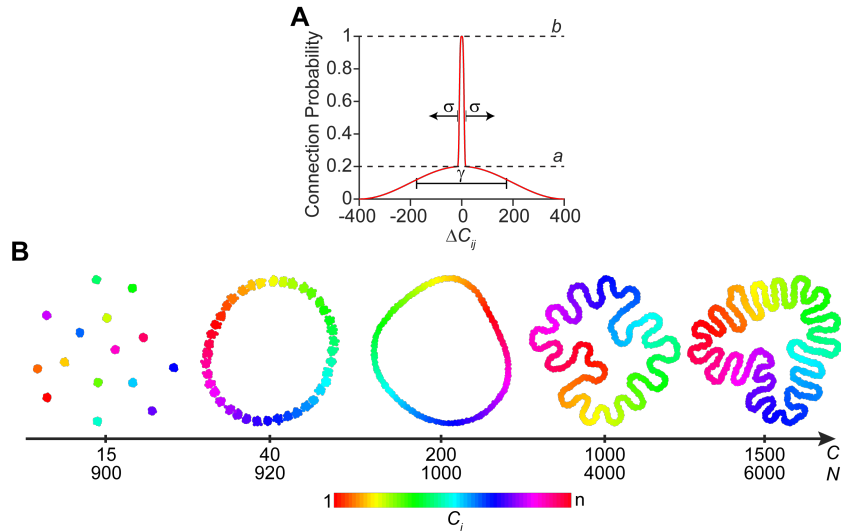


Figure 15. Cortical folding derived from connectivity

(Note: Figure by Groden et al. (2019), Fig. 1 A and B) **A**, Connection probability function based on the topological distance between cortical columns, featuring strong local but sparse long range connectivity. σ : width of local connectivity; γ : decay of global connectivity; a : strength of global connectivity; b : strength of local connectivity. **B**, Results for folding patterns with a fixed connectivity ($b = 1$, $a = 0.2$, $\sigma = 0.1$, $\gamma = 1$), but increasing number of columns C and decreasing number of neurons per column $M = N/C$. The results show a transition from nuclei to lissencephalic to convoluted folding patterns. Points with the same colour belong to the same cortical column

The model neurons and columns are connected topologically in a cyclical fashion, meaning that neurons in column 1 and neurons in column C are neighbours. This way, the model columns form a topological ring. The connections between neurons are set randomly following a connection probability function that depends on the topological $\Delta C_{i,j}$ distance between the columns of neuron i and j (Fig. 15 A). The shape of the connection probability function (see Materials and methods **Chapter 4**) is controlled by a set of parameters. The strength of global and local connectivity can be adjusted via the parameters a and b , where a is responsible for global and b for local connectivity. a and b are used to create an offset between local and global connectivity to meet the requirements of strong local and sparse long range connectivity. γ controls the speed of global connectivity decay, while σ sets the range of local connectivity. The number of neurons in the simulation is considerably lower than neuron numbers found in real mammalian brains due to computational limits. For the same reason, the model is restricted to 2D gyrification patterns. The resulting patterns therefore resemble coronal or horizontal slice images of the cortex as depicted in Fig. 15 B. In Fig. 15 B, folding patterns are shown with ascending numbers of columns C and neurons N from left to right with all

other connectivity parameters fixed. Each column is assigned a colour in Fig.15 B, such that all points, which represent single neurons, with the same colour belong to the same column. Depending on the ratio between C and N , the number of neurons per column M differs as well, with $M = N/C$. In case $M \gg C$ like with the first layout on the left in Fig. 15 B, the model predicts a pattern that features multiple separate neuron clusters that resemble the ganglia-like nervous systems found in for example, worms (Mayer and Whittington (2009)). As C and N increases, there is a relative decrease in the number of neurons per column M and the folding patterns form a connected ring shaped layout to the point where intricate folding emerges. The level of folding increases with decreasing numbers of neurons per column, going from lissencephalic to highly convoluted. As demonstrated in Fig. 16 the gyrification model is able to produce extreme levels of folding for large cortices (high values for C) and large total number of neurons N . The optimal placement method t-SNE in the model also predicts degenerate solutions for folding patterns. Such degenerate folding patterns do not form a closed loop, but rather have overlapping sections where the pattern crosses itself as depicted in Fig.17. Degeneracy among folding patterns can occur even when using sets of parameters that otherwise produce regular ring-like layouts. Using custom code in MATLAB, these degenerate patterns were identified automatically and discarded (see Materials and methods **Chapter 4**).

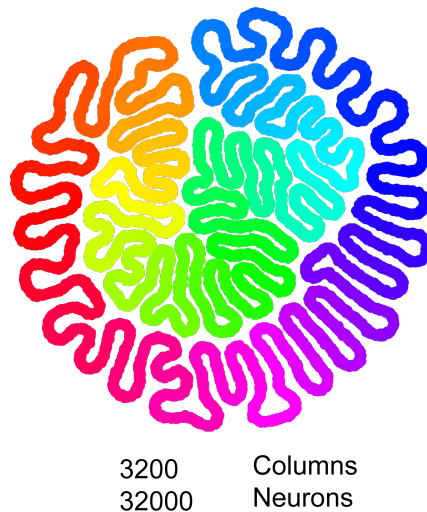


Figure 16. Folding patterns with extreme folding

By adjusting the folding parameters, folding patterns can reach extreme levels of gyrification ($C = 3200$, $M = 10$, $a = 0.1$, $b = 1$, $\sigma = 0.01$, $\gamma = 1$).

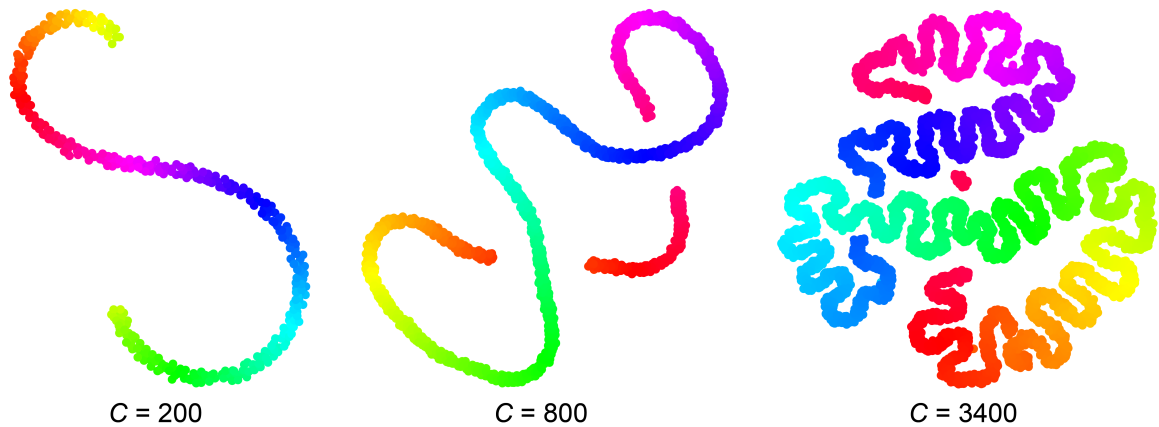


Figure 17. Degenerate folding results

(Note: Figure by Groden et al. (2019), Fig. S1 A) Examples of degenerate folding patterns with different numbers of columns (parameters: $\sigma = 1.5$, $a = 0.2$ and $M = 2$).

The degree of folding of the cortex in mammalian species increases dramatically with brain size, more specifically the surface area of the cortex. The increase in gyrification is especially significant for cortices that are relatively thin. For primates of increasing size, cortical thickness does not change much, while brain size increases along with the level of gyrification (Fig. 18 A) (Mota and Herculano-Houzel (2015), Zilles et al. (2013), Hofman (1985)). As cortical columns correspond to small patches of cortex, the parameter for the number of columns C in the model determines the size of the cortical sheet. Cortical thickness on the other hand is modelled by the number of neurons per column M , as columns span the cortex vertically. As a result, increasing the number of columns in the simulation while keeping M and all connectivity parameters constant should yield a similar trend in folding as observed in mammalian species. The model does indeed reproduce the same transition from lissencephalic cortices to highly convoluted ones when cortical size (the number of cortical columns) is increased as shown in Fig. 18 B. The first (primary) folds that start to emerge exhibit large amplitudes and a long spatial wavelength. As C increases, smaller secondary gyri and sulci start to develop on top of the primary folds that feature a higher frequency and smaller amplitude. In order to quantify the degree of folding of the folding patterns produced by the model, the folding index FI was calculated.

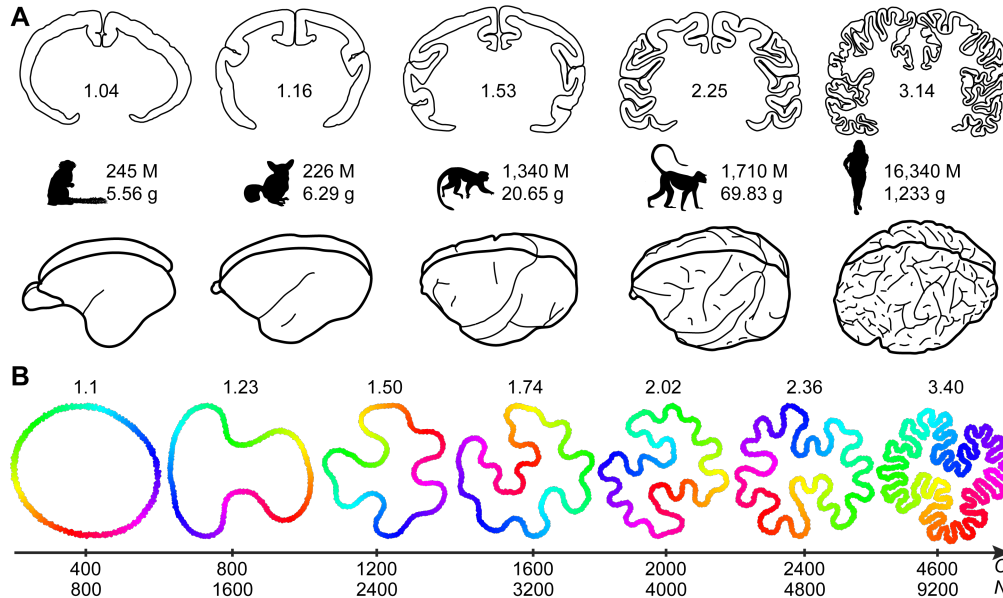


Figure 18. Cortical folding transition from lissencephalic to convoluted

(Note: Figure by Groden et al. (2019), Fig. 2 A and B) **A**, (Top) Traces of primate brain sections for species with increasing brain weight and number of neurons in million (FI value depicted in each brain section). From left to right: marmoset, galago, squirrel monkey, macaque, and human. (Bottom) Traces of the full brains for reference. **B**, Example model results with fixed connectivity and number of neurons per column ($M = 2, b = 1, a = 0.2, \sigma = 2.6, \gamma = 1$). C and N are increased gradually showing a transition from lissencephalic to convoluted like in **A** (FI depicted above each folding pattern).

FI is defined as the inverse ratio between length of the convex hull, which envelopes the outer most perimeter of the pattern and the tight boundary that follows the patterns exact contour (see Materials and methods **Chapter 4**). In Fig. 18 FI is shown for each layout as a decimal number.

To graphically visualise the overall trend of gyrification in model folding patterns, the fractal dimension and the spatial frequency spectrum of gyri and sulci in addition to FI were calculated for a large parameter space of C . The fractal dimension is a measure of how space-filling a 1D line is that produces self similar patterns. It ranges from 1 to 2, while 1 corresponds to a straight line and 2 to a line that fills the entire available 2D-space. The frequency spectrum was calculated using the fast Fourier transform function FFT in MATLAB, applied to a smoothing spline fit curve that fit the tight boundary of the folding pattern. The curve was calculated by measuring the distance of each boundary point to the centre of mass of the folding pattern (see Materials and methods **Chapter 4**).

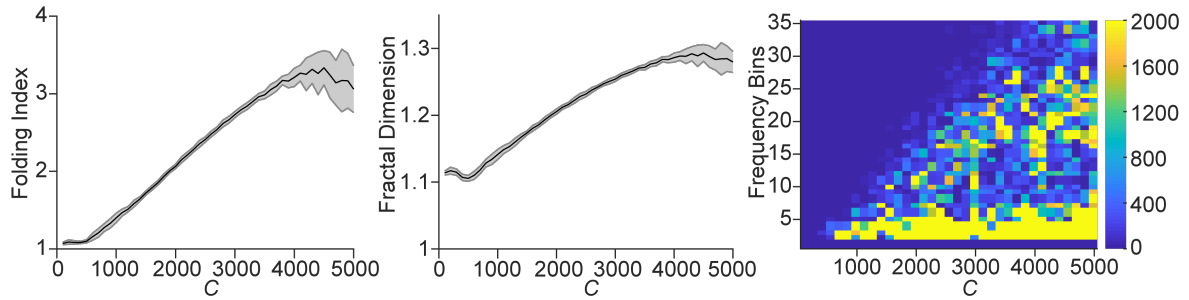


Figure 19. Quantifying gyrification

(Note: Figure by Groden et al. (2019), Fig. 2 C) Measures of the degree of folding from the folding pattern data set depicted in Fig. 18 B. C is increased from $C = 100$ to $C = 5000$ in 100 steps. The black line is the mean of 30 trials for each data point with the grey shaded area being the standard deviation. **Left:** Folding index FI plotted against the number of columns C . **Middle:** Fractal dimension plotted against C . **Right:** Amplitudes of spatial folding frequency bins as indicated by the colours.

The resulting graphs of the three measures are depicted in Fig. 19, with FI on the left, the fractal dimension in the middle and the frequency spectrum on the right. As expected, both FI and the fractal dimension show an increase with the number of columns C . They do however reach a peak indicating a maximum degree of folding. The spatial frequency spectrum shows the same trend with low frequency folds emerging first at low numbers of C . As C increases they stay present, but higher frequency folds start to develop (compare Fig. 18 B). The power in the frequency spectrum corresponds to the occurrence of a frequency and its relative amplitude. Since the low frequency folds amplitude (relative distance to the centre of mass) is large, they exhibit a high power in the frequency spectrum. Closely observing all three graphs, a decline in FI , the fractal dimension and high frequency folds in the frequency spectrum becomes apparent when C increases towards large numbers. Further increasing C leads back to lissencephalic folding patterns. Depending on the chosen set of connectivity parameters, this phenomenon is more or less pronounced. The higher frequency folds start to merge, forming a thicker cortex that still exhibits low frequency folds (Fig. 20 A). This phenomenon resembles the phenotype of the manatee (Fig. 20 B), which always has been an outlier, as its cortex is rather large yet lissencephalic and thick.

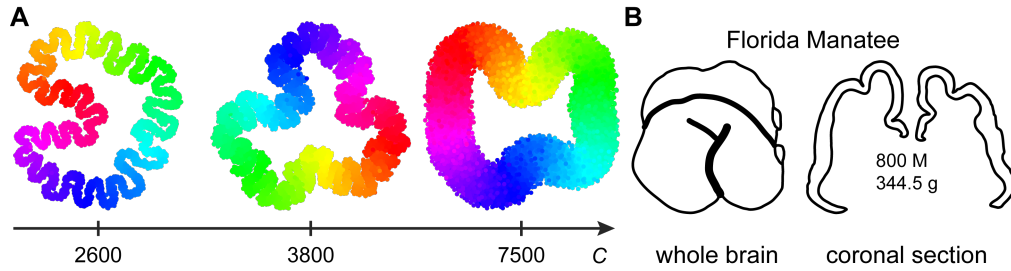


Figure 20. The exception of the manatee

(Note: Figure by Groden et al. (2019), Fig. 2 D) **A**, Increasing the number of columns even further with a fixed connectivity ($M = 2, a = 0.25, \sigma = 1.5, \gamma = 1$) leads to lissencephalic folding patterns. **B**, Tracing of the manatee brain with brain weight and number of neurons in million. Whole brain tracing on the left (only cortex and bulbus olfactorius shown) and section tracing on the right.

Cortical folding does not only scale with brain size in general. The strength of gyrification scaling varies between different orders of mammals (Mota and Herculano-Houzel (2015), Zilles et al. (2013), Pillay and Manger (2007)).

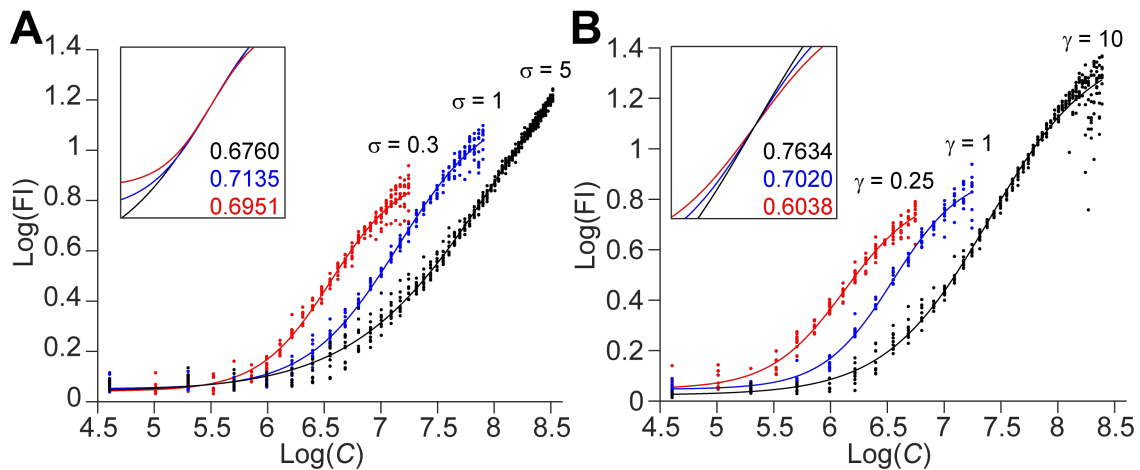


Figure 21. FI scaling for different mammalian orders predicted by the brain folding model

(Note: Figure by Groden et al. (2019), Fig. 5) Depending on connectivity, the level of gyrification scales differently with increasing cortical size C . 10 trials were calculated for each value of C . The other folding parameters were fixed unless stated otherwise ($a = 0.2, b = 1, M = 2, \gamma = 1, \sigma = 0.3$). **A**, The folding index FI increases with the number of cortical columns C for different values of width for local connectivity σ (red, blue and black). For red $C = 100$ to $C = 2000$ in 50 steps. For blue $C = 100$ to $C = 3000$ in 100 steps. For black $C = 200$ to $C = 5000$ in 100 steps. **B**, The folding index FI increases with the number of cortical columns C for different values of decay in global connectivity γ but also scales differently (red, blue and black). Same increments of C used here as in **A**. The data points in **A** and **B** were fitted using a sigmoidal function. The inlays in both graphs are a magnification of the sigmoidal fits overlaid at the point of greatest slope. The value for the slope is also shown. In **A** slopes are roughly the same whereas in **B**, slopes vary significantly.

The gyrification model predicts these variations in scaling when altering connectivity parameters. The model predictions for the folding index FI for different brain sizes (number of columns C) are demonstrated in Fig. 21. Increasing the influence of local connectivity, which in the model is done by increasing σ or γ (compare Fig. 22), leads to a shift in the onset of gyrification as well as a higher peak FI (Fig. 21 A and B). If C is increased even further, the degree of folding (FI) goes back down to 1 ($\log(1) = 0$ as in Fig. 21) in all cases, which corresponds to lissencephalic cortices. Fitting the data points using a sigmoid function reveals the maximum slope of each curve as indicated by the inlays. Varying σ does not change the magnitude of scaling in FI (Fig. 21 A), while altering γ yields significantly different values for the maximum slope (Fig. 21 B). Quantitatively reproducing the results for the slopes of scaling for different mammalian orders as found by Zilles et al. (2013) has not been possible with the model approach. This issue is due to the low number of neurons in the model compared to the real brain. However, calculating the differences in slope between the curves from Fig. 21 B does match the differences in slope published by Zilles et al. (2013).

5.2.1 The impact of connectivity

Folding pattern shapes and properties in the model are heavily impacted by cortical size and the number of neurons per column. However, the choice of connectivity parameters has an equally significant effect. There are three parameters which influence different aspects of connectivity. γ determines the width of global, while σ controls that of local connectivity. The difference in strength between global and local connectivity is set by a . The strength parameter for the local connectivity b is for the purpose of this demonstration considered to be equal to one,

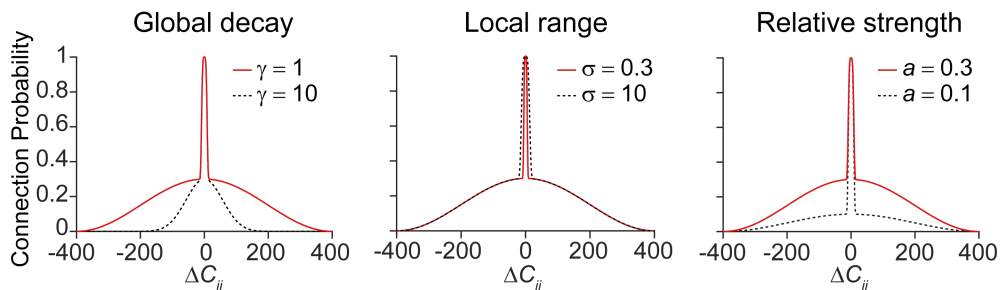


Figure 22. Connectivity parameters

(Note: Figure by Groden et al. (2019), Fig. 3 A, B, C top) Examples of how the connectivity parameters affect the shape of the connectivity function for γ , σ and a .

since the connection probability to the closest neighbours is very strong (b can however be adjusted). Fig. 22 visualises how the three connectivity parameters change the shape of the models connection probability function. To quantify the impact of a certain parameter, all other parameters were kept constant. Fig.23 A shows some example folding patterns demonstrating the effects of varying each of the three connectivity parameters respectively. These examples serve as a visual reference to better understand the graphs in Fig.23 B, which quantify the change in folding pattern properties induced by differences in connectivity. Large values of σ correspond to a wide range of local connectivity (Fig. 22 middle), which leads to large folds of low frequency (Fig. 23 A and B left). Decreasing σ and therefore the range of local connectivity increases the frequency of gyri and sulci. With more frequent folds the degree folding (folding index FI) increases as well, leading to a more fractal arrangement (increase in fractal dimension). Large folds with large amplitudes seem to be present throughout σ 's parameter range as indicated by the frequency spectrum.

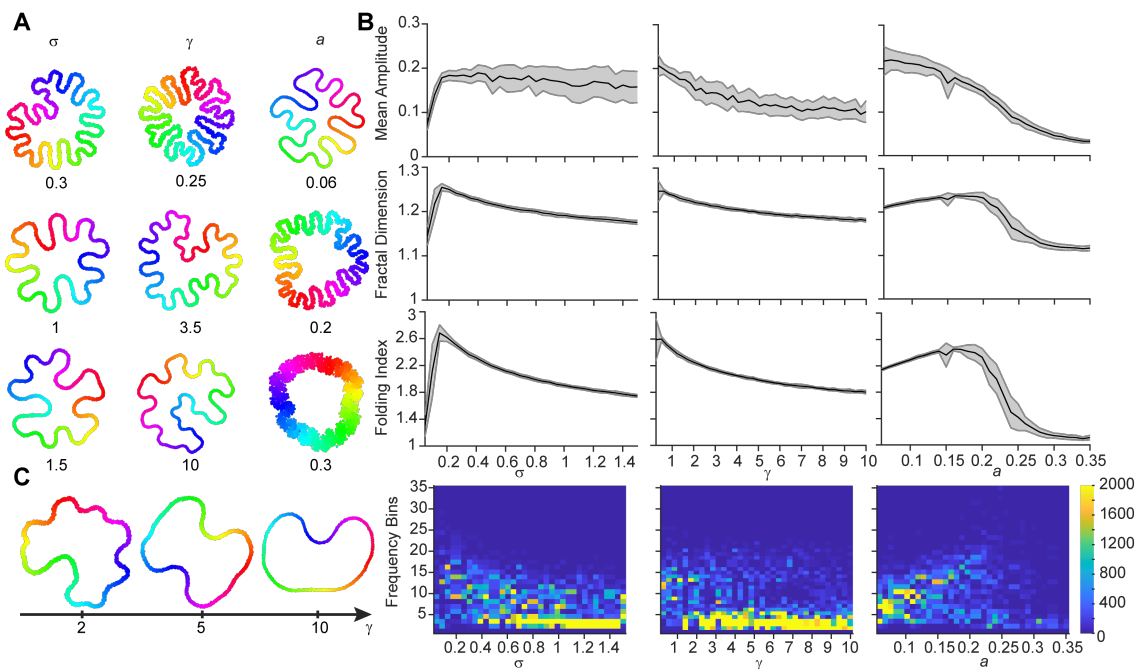


Figure 23. The impact of connectivity on folding patterns

(Note: Figure panel B by Groden et al. (2019), Fig. 3 A, B, C bottom) **A**, Example folding patterns for different values of σ , γ and a . **B**, Quantification of folding pattern properties with a fixed parameter set ($b = 1$, $a = 0.15$, $\sigma = 0.3$, $\gamma = 1$, $C = 1400$, $M = 2$). From left to right, σ is varied first (from $\sigma = 0.05$ to $\sigma = 1.5$ in 0.05 steps), then γ (from $\gamma = 0.25$ to $\gamma = 10$ in 0.25 steps) and last a (from $a = 0.06$ to $a = 0.3$ in 0.01 steps). The black line is the mean of 40 trial for each data point. Standard deviation in grey. **C**, Increasing γ and therefore the decay of global connectivity leads to lissencephaly ($b = 1$, $C = 600$, $M = 2$, $a = 0.2$, $\sigma = 0.3$).

Folds do however not only depend on the range of local connectivity. When changing the range of global connectivity, the degree of folding varies significantly. Specifically large values of γ which correspond to a low range of global connectivity (Fig. 22 left) result in a low degree of folding (low FI). Increasing the range of global connectivity leads to a significant increase in FI and a slight increase in fractal dimension. Interestingly, changes in γ have the same effect on folding patterns as changes in σ . However, the changes in global and local connectivity range are exactly opposite. While a wide range in global connectivity induces more folding, the same is true for a low range in local connectivity. The increase in gyrification induced by global connectivity, is however, different since the mean amplitude of folds increases, but their frequency is relatively constant. When the number of columns is decreased, large values for γ with a low range of global connectivity cause folds to disappear almost entirely as depicted in Fig. 23 C. Folding, therefore, seems to be dependent on the existence of long range connections. Increasing the strength of global connectivity a increases the frequency of folds, but at the same time decreases their mean amplitude. Compared to the impact of σ when increased, a has the inverse effect. Therefore, an increase in local connectivity width counteracts an increase in global connectivity strength (compare Fig. 22 and Fig. 23 A and B). An extensive increase in a however eventually leads to a drop in FI and fractal dimension. The frequency of gyri and sulci increases to the point where they merge into each other. Therefore, the level of gyrification decreases after it reached a peak. Maximum gyrification hence can be achieved with an optimal value for a (global connectivity strength).

5.2.2 Breaking symmetry

While folding patterns modelled with similar or the same parameter sets tend to look alike, their appearance never matches exactly. The differences between folding patterns with the same parameter set are very subtle, but when looking at details like for example, the exact position of a single gyri or sulci, significant variations become evident (Fig. 24). Therefore, parameters that correspond to the size, the thickness and the connectivity of the cortex do not lead to the formation of a stereotypical folding pattern in the model. Breaking the symmetry of the model's cyclical connection probability distribution, however, leads to the formation of stereotypical folds. In an asymmetrical folding pattern, the connectivity parameters are altered on specific sections of its perimeter.



Figure 24. Folding patterns with the same parameters are not identical

(Note: Figure by Groden et al. (2019), Fig. S3 A) Folding patterns sharing the same parameter set ($C = 600$, $M = 2$, $a = 0.2$, $\sigma = 0.3$, $\gamma = 0.5$) or even the same binary connection matrix are not identical as showcased by three examples.

Fig. 25 shows the consequences of this procedure when altering the width of local connectivity σ (Fig. 25 A), the strength of global connectivity a (Fig. 25 B) and the number of neurons per column M (Fig. 25 C). In each panel, the framed folding pattern has its perimeter amplitudes with respect to the center of mass plotted against the column index C_i on the right for better quantitative understanding. The part of the perimeter where the parameter was altered is marked by the shaded area. As indicated by the colour coding of cortical columns, the change in folding occurs at the same location of the cortex perimeter for each individual parameter that was altered. Therefore, folding can be altered stereo-typically in a local section of the perimeter by changing cortical connectivity parameters. For local connectivity σ and global connectivity a changes in sections of the perimeter led to the same differences in gyrification compared to parameter changes on the entire perimeter (compare Fig. 23). According to these results, local folding in the mammalian cortex is likely to depend on changes in the local connectivity and the number of neurons per column, meaning cortical thickness. The model is also capable of repeatedly producing recognisable individual folds by using the same approach of altering the connectivity in a certain section of the perimeter. Such folds emerge when increasing the strength of local connectivity b . Fig. 26 shows three examples that feature the same change in connectivity in the same section of the perimeter that leads to a characteristic fold in that area, which is marked in black. In the area marked black b is changed to 1, while in the rest of the folding pattern $b = 0.6$. Brain disorders can change the appearance of the folding arrangement in many ways (Walsh (1999), Sun and Hevner (2014), Barkovich et al. (2012), Fernández et al. (2016)). Changes can be specific to certain areas only, or affect the entire cortex. Such changes in folding can be reproduced by the model by breaking the symmetry and altering the model parameters.

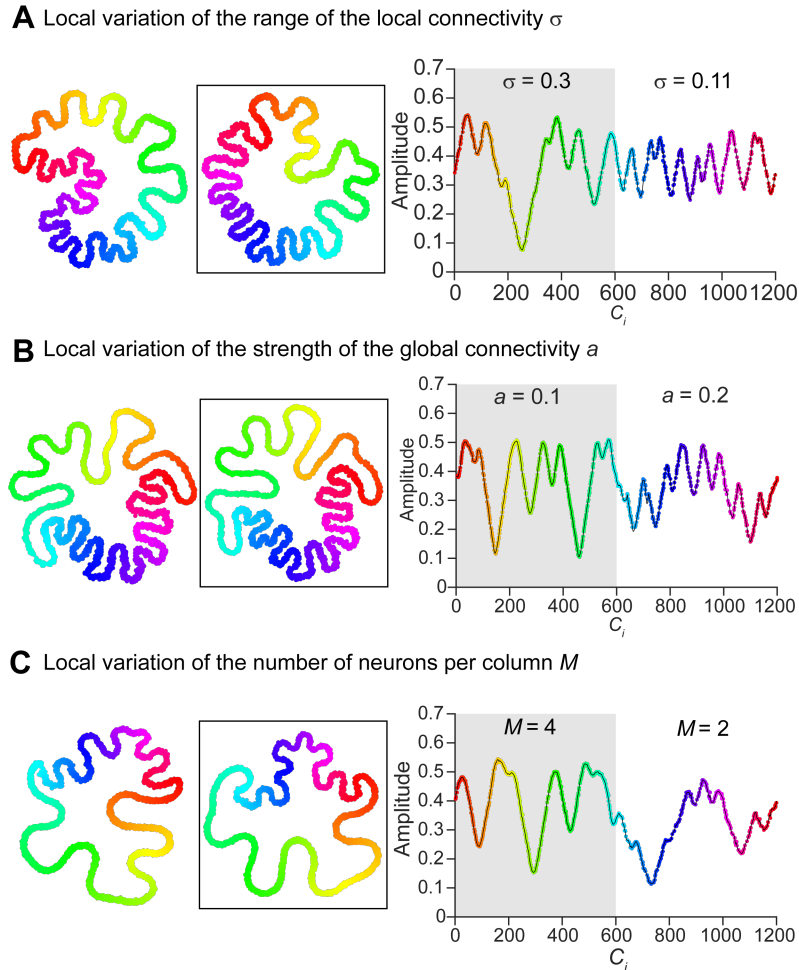


Figure 25. Stereotypical folding patterns

(Note: Figure by Groden et al. (2019), Fig. 4) Varying the connectivity function in a specific region leads to stereotypical folding arrangements. **A**, (Left) Example folding patterns where the local connectivity σ has been varied in a specific region ($C = 1200$, $a = 0.2$, $b = 1$, $M = 3$, $\gamma = 1$). (Right) Amplitude to the center of mass plotted for the framed folding pattern. Colours indicate cortical columns and position on the folding pattern. Regions for different values of σ are indicated by the shaded area. **B**, Same arrangement as in **A** with a being varied. Other parameters are ($C = 1200$, $b = 1$, $\sigma = 0.1$, $M = 3$, $\gamma = 1$). **C**, Same arrangement as in **A** but M is varied. Other parameters are ($C = 1200$, $b = 1$, $\sigma = 0.1$, $a = 0.2$, $\gamma = 1$).

The folding pattern in the centre of Fig. 27 represents the healthy brain, with its "healthy set of parameters". To reproduce the changes in folding caused by a brain disorder, the "healthy set of parameters" is altered accordingly, resulting in the folding patterns at the end of the arrows, that represent pathological arrangements. In cases where parameters were altered in a section of the folding pattern only, this particular section is marked in black.

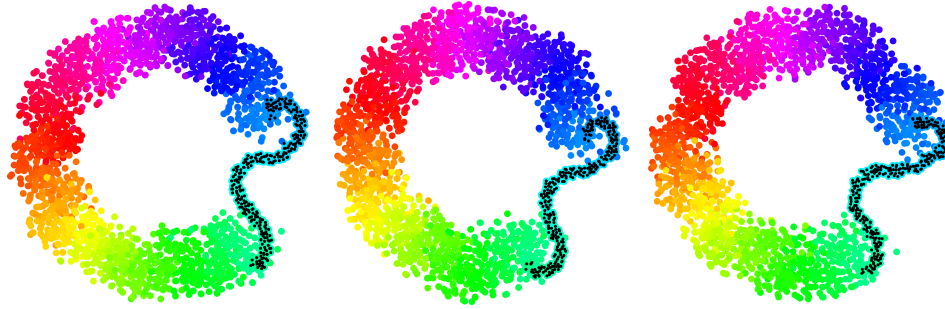


Figure 26. Characteristic single folds

(Note: Figure by Groden et al. (2019), Fig. S4) Example folding patterns with increased strength of $b = 1$ in a local area (marked black) produce a single stereotypical fold. In the rest of the folding pattern $b = 0.6$ ($C = 1000$, $M = 2$, $a = 0.2$, $b = 0.6$, $\sigma = 1$, $\gamma = 1$).

Polymicrogyria is one example of such a gyrification altering condition. Here, cortical thickness decreases and the frequency of folds increases while the size of gyri and sulci decreases (Chang et al. (2004)), which is the opposite of a thicker cortex, leading to lissencephaly (Toro and Burnod (2005), Richman et al. (1975), Budday et al. (2014)). This is exactly in line with the gyrification model, since as discussed multiple times, reducing the number of neurons per column M , which corresponds to a thinner cortex, increases folding in the model (Fig. 27 top, Fig. 45 left). Even though there reportedly is a change in connectivity caused by polymicrogyria, its exact nature is unknown (Trivedi et al. (2006)). In the gyrification model, increasing the strength of global connectivity by increasing a leads to shallower folds (Fig. 23 A and B). Therefore, the model predicts a reduced mean amplitude for gyri and sulci if the relative difference between the strength of local and global connectivity is reduced (increasing a while b stays constant). As demonstrated in Fig. 25 B, a change in a can be restricted to a section of the cortex in the model. Accordingly, polymicrogyria can develop in only part of the cortex because of altered local connectivity (Fig. 27 top). Clinical studies did indeed find cases where the entire cortex was affected by polymicrogyria, as well as examples where only specific regions exhibited the disorder (Rai et al. (2015), Chang et al. (2004), Jansen and Andermann (2005)). Patients with autism typically also exhibit cortices with changes in the degree of folding. The region most affected in autism is the frontal lobe, where deeper folds emerge increasing the folding index FI (Carper and Courchesne (2005), Hardan et al. (2004), Nordahl et al. (2007)). The same phenotype can be reproduced in the gyrification model by lowering the strength of global connectivity a (Fig. 27 left, Fig. 23 A and B).

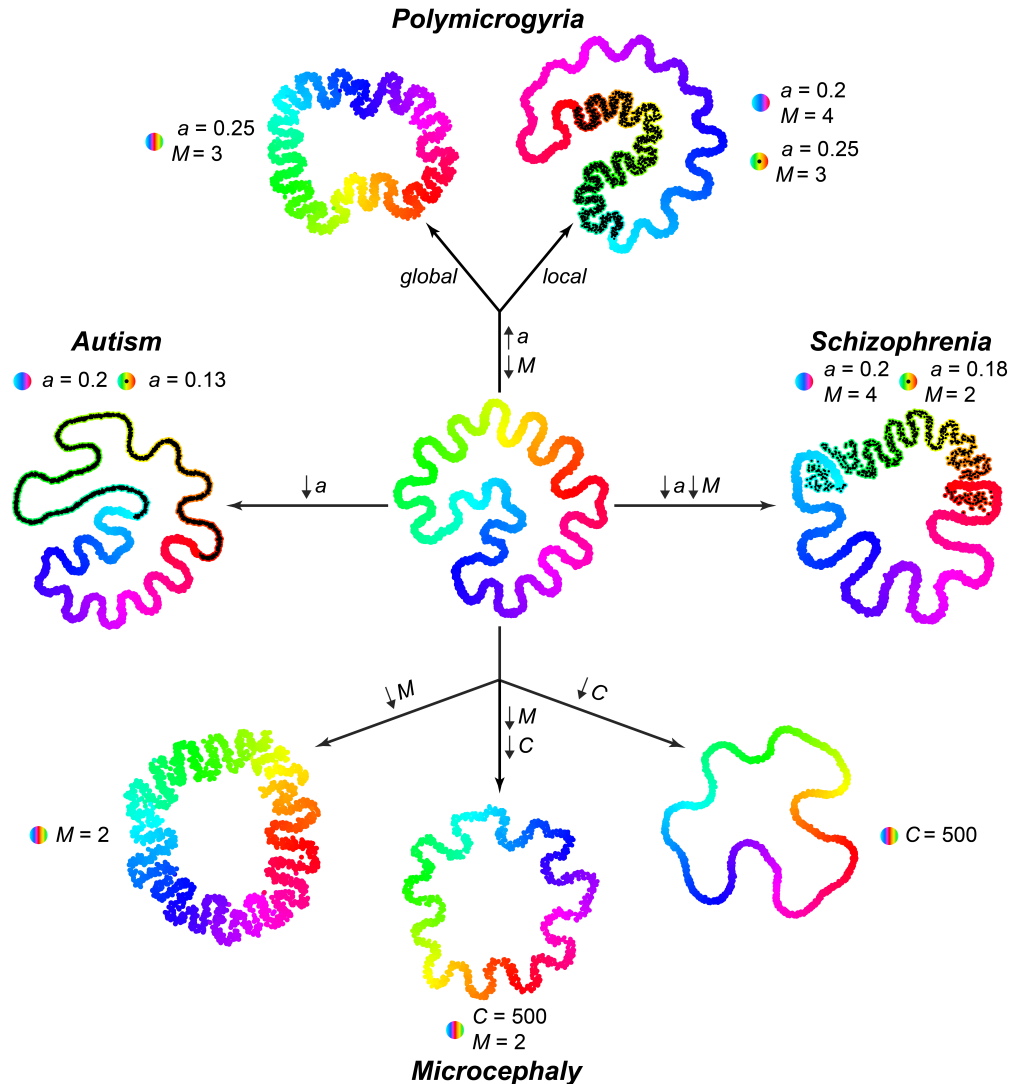


Figure 27. Model predictions of folding changes in brain disorders

(Note: Figure by Groden et al. (2019), Fig. 6) The gyrification model is capable of reproducing the pathological changes in folding of the human brain caused by brain disorders. **Middle:** In this plot, this is assumed to be the normal healthy cortical folding pattern that uses the following parameters, $C = 1000$, $M = 4$, $a = 0.2$, $b = 1$, $\sigma = 0.1$ and $\gamma = 1$. **Top:** The model reproduces Polymicrogyria, which is a pathological condition where smaller, more frequent folds are observed as well as a thinner cortical sheet. The change in folding is expressed either globally or locally, as also demonstrated by the model results. In the model, this is achieved by lowering M and increasing a . **Right:** Schizophrenia causes the superior temporal gyrus to exhibit an increased folding frequency, as well as a deeper superior temporal sulcus. The model predicts a similar result when decreasing both a and M . **Bottom:** When modelling Microcephaly a decrease in C , M or both leads to completely different folding arrangements. Decreasing C counteracts a decrease in M , since lower C increases folding and lower M has the opposite effect. Decreasing both at the same time results in a similar appearance to the folding pattern shown in the center. **Left:** In Autism, the frontal lobe of the brain exhibits deeper folds. By lowering the strength of global connectivity a in a section of the folding pattern the model achieves a similar result.

The model predictions agree with findings of Catani et al. (2016), Just et al. (2007) and Courchesne and Pierce (2005), where deeper folds correspond to strong local but weakened global connectivity. Similar to the next example disorder, schizophrenia, changes in folding caused by autism are much more subtle compared to polymicrogyria (Nordahl et al. (2007), Wisco et al. (2007)). The superior temporal sulcus in schizophrenia is enlarged, exhibiting increased depth (Csernansky et al. (2008)). In terms of connectivity, a decrease in global connectivity strength (Geoffroy et al. (2014), Alderson-Day et al. (2015), Skudlarski et al. (2010)), as well as decreased cortex thickness at the superior temporal gyrus that goes along with increased folding frequency reportedly correspond to schizophrenia disorder (Wisco et al. (2007)). The increase in folding frequency is likely due to the decrease in cortical thickness as observed in polymicrogyria, while a deeper superior temporal sulcus might be due to the decrease in global connectivity strength (Richman et al. (1975), Budday et al. (2014), Toro and Burnod (2005))(Fig. 27 right, Fig. 23 A and B, Fig. 45). In contrast to the other examples, microcephaly is associated with a significantly smaller brain, which can exhibit a normal appearance other than being too small. Folding can also be reduced in microcephaly (Volpe (2008), Francis et al. (2006)). In this brain disorder, connectivity does not seem to be altered, however, there is a deficiency in neuronal proliferation (Gilmore and Walsh (2013), Barkovich et al. (2012)). A decrease in neuronal proliferation might cause the diminution in cortical size with a relatively small number of columns, a low number of neurons per column or even both at the same time (Volpe (2008)). To reproduce a folding pattern in the model with an appearance similar to the "healthy state pattern" (Fig. 27 centre) but with less folds, both the number of columns and the number of neurons per column have to be scaled down in a uniform fashion (Fig. 27 bottom).

5.3 Microscopic modelling: A realistic neuron repair algorithm

Like the gyrification model introduced in this thesis, the neuron repair algorithm explained here is based on the simple principle of wiring optimisation. Artificial neurons can be grown in a computer simulation based on this approach, using the *in silico* TREES toolbox (Cuntz et al. (2010)). The TREES toolbox is build upon the minimum spanning tree algorithm (MST), which uses a balancing factor bf to optimise a cost function that weighs conduction time to the soma against total wiring length (see Materials and methods **Chapter 4**). With the reconstruction of neurons from microscopic images being a difficult procedure, the resulting

3D morphology reconstructions are often incomplete (De Schutter and Jaeger (2000)). This can be due to for example, lesion when cutting tissue, image distortion, shrinkage or staining agents failing to reach the most distal parts of dendrites. The neuron repair tool developed in this thesis is a Graphical-User-Interface (GUI) that can be used to repair any given morphology by extending the existing incomplete dendritic arbor with artificial dendrites.

5.3.1 The GUI and *fix_tree* function

The repair algorithm in and of itself consists of the *fix_tree* function (for details see Materials and methods **Chapter 4**) that is called upon by a Graphical-User-Interface (GUI) environment. The interface allows the user to upload an incomplete 3D neuron morphology as depicted in Fig. 28 (1.). In order to be able to accurately estimate the dimensions of the neuron morphology reconstruction, a background image stack can be uploaded to the GUI (Fig. 28 (2.)). For this purpose, different layers in the tissue can be marked out by lines, like in the example image in Fig. 28, that shows the stratum oriens (SO), the stratum pyramidale (Spir), the stratum radiatum (SR) and the stratum lacunosum moleculare (SLM) of the CA1 region in the mouse hippocampus. Image stacks can be uploaded in 3D or 2D. The position as well as the orientation of the morphology can be adjusted freely, to fit the background image (4.). In case the size of the background image is out of sync with the reconstruction, the voxel size can also be adjusted at will (3.). These adjustments are done via the *Image Stack* panel in the top right corner.

The region where new extended artificial dendrites should be added to the existing morphology can be marked out in the GUI. In case the volume and its position is already known, the user can upload volume coordinates to the interface. Otherwise, the perimeter of the volume can be drawn on the screen by selecting the coordinates with the cursor. This procedure is initiated via the *Repair Panel* (5.) and has to feature points being selected in at least two of three planes (x-y, x-z and y-z-plane). By hitting the repair button (7.), the algorithm determines the growth volume set by the chosen coordinates, using the *boundary* function in MATLAB, and initiates the repair automatically. All parameters for the repair are estimated by the algorithm automatically (see Materials and methods **Chapter 4**), but can be individualised via the interface (6.). The only exception here are pruning parameters, since pruning is optional. If needed, the algorithm can be limited to not grow beyond a set value of total dendritic length as well as maximum number of branch points.

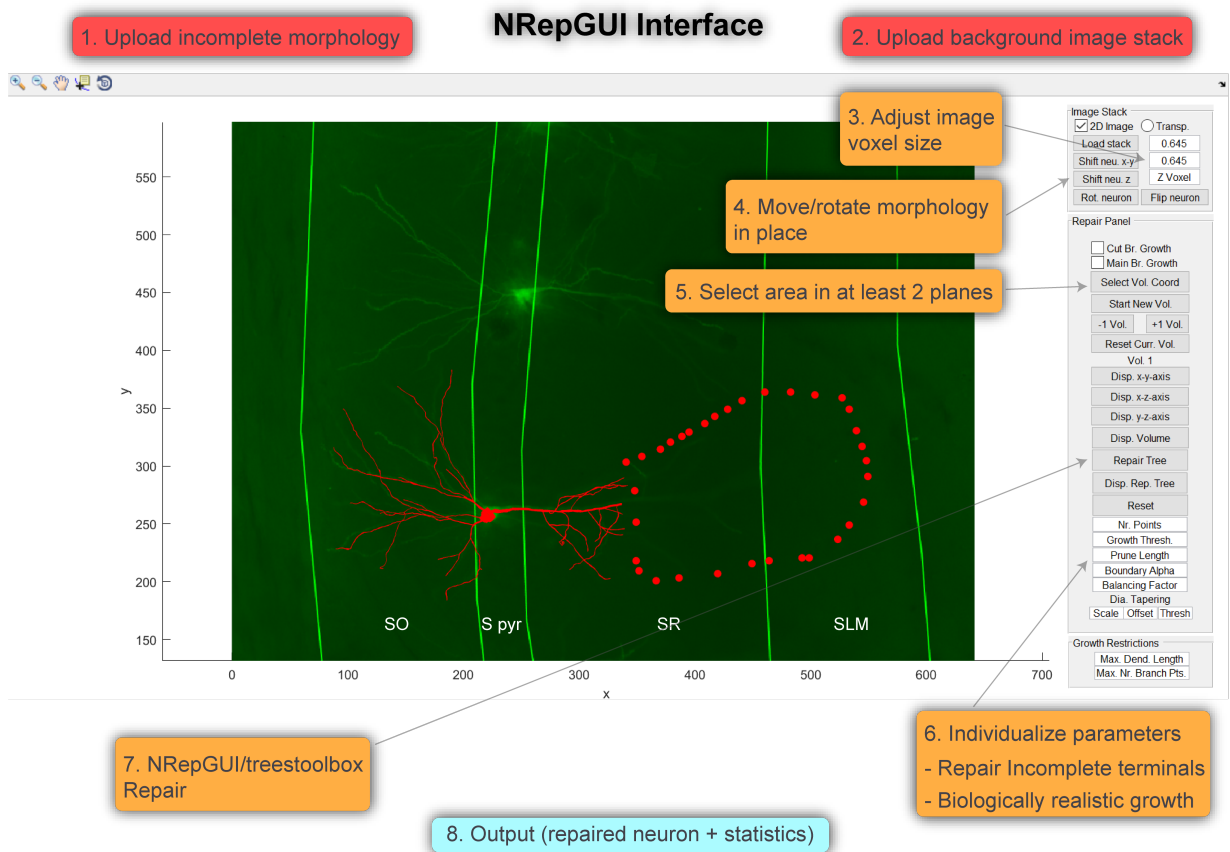


Figure 28. Neuron repair tool GUI

Illustration of the graphical-user-interface of the neuron repair tool. Plot of the neuron morphology and microscope image stack in the middle with the tool bar on the right. The bullet points 1. to 8. represent the necessary steps to upload a neuron morphology and image stack and then successfully repair the damaged morphology. The red points are an indication of a volume being drawn with the cursor.

Alternatively, a reference morphology can be uploaded to the GUI, if existent. The algorithm will then use the statistics of the reference morphology as a template, matching the number of branch points and the total dendritic length of the repaired morphology to the reference. Uploading a reference morphology is completely optional, mostly used to test the algorithm's functionality. In the default growth mode, new branches can grow from any random point on the original morphology in close vicinity to the growth volume (biological growth mode). This mode is meant to imitate biological regrowth of a damaged neuron, re-invading the vacant space. The second growth mode, referred to as incomplete growth mode, is used to repair morphologies that have been damaged accidentally during the reconstruction process.

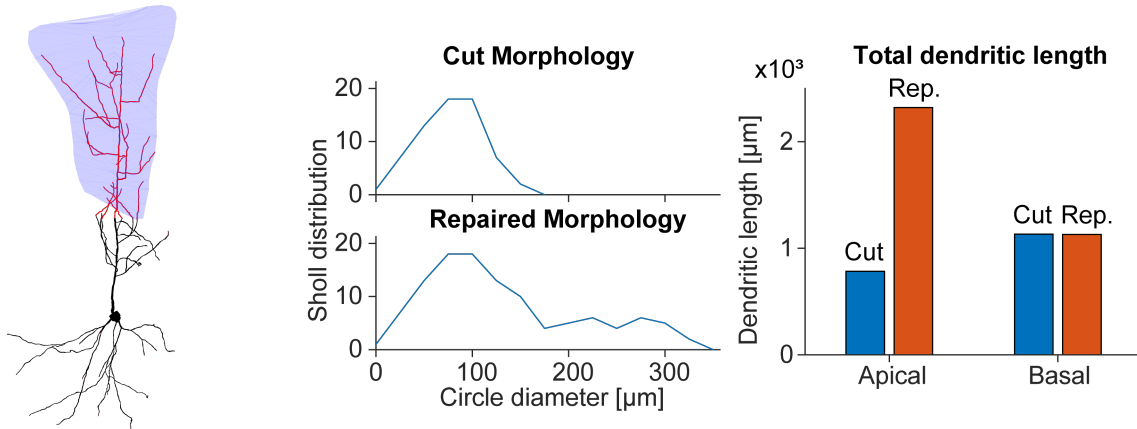


Figure 29. Lost dendritic material can be recovered with the new growth algorithm

Example GUI output, with the repaired morphology on the left. The input morphology is marked in black with the repaired dendrites marked in red. The blue shaded area is the repair volume. The GUI also outputs a before-after comparison of morphological statistics with two examples depicted on the right (Sholl intersection distribution and Total dendritic length for basal and apical arbor).

Here, the reconstructing scientist usually knows which ends of the dendrites have been severed and in which area the missing dendritic material is supposed to grow. Consequently, with the incomplete ends of the dendrite marked out in the uploaded morphology file, the repair algorithm will exclusively grow artificial dendrites from these severed ends in case the incomplete growth mode is engaged. There is one more option that can be engaged when the incomplete growth mode is active, dedicated to the special growth requirements of pyramidal neurons, since their apical dendritic arbor features a prominent main apical dendrite (Benavides-Piccione et al. (2020)). Engaging this option grows the main apical dendrite first before proceeding with the regular growth protocol (see Materials and methods **Chapter 4**). Fig. 29 shows an example output of the GUI with a repaired morphology on the left (artificial dendrites in red, growth volume in blue). The GUI automatically calculates morphological statistics like for example, the Sholl intersection distribution and the total dendritic length in a before and after comparison (Fig. 29 middle and right). The GUI includes more statistics than the examples shown here. The GUI is designed to address the issue of sparse human neuron reconstructions. This is done by repairing damaged morphologies, extending their dendrites artificially in areas where branches should be growing, but could not be reconstructed. The algorithm restores the morphological as well as the electrophysiological properties of the neuron. This will increase the accuracy and reliability of neuron morphology data sets.

5.3.2 Validating the neuron repair algorithm

Human neuron morphologies are poorly understood compared to for example, those of rodents. For this reason, testing and validating the repair algorithm is based on a data set of mouse CA1 pyramidal neurons (Benavides-Piccione et al. (2020)) (see Fig.11). Pyramidal cells are the most abundant neuron type in the brain and mouse neurons are widely studied, increasing the reliability of algorithm testing. Judging how good the repair of a neuron is requires a reference. Therefore, the reconstructed mouse pyramidal morphologies from the Benavides-Piccione et al. (2020) data set were cut intentionally in an arbitrary location in both the apical and the basal arbor at different points and angles. The cut morphology is used as an input to the repair algorithm to be repaired and the original morphology serves as the reference which is also passed to the algorithm. As described earlier, the algorithm matches the morphological statistics of the repaired morphology to the reference. The reference, the cut and the repaired morphologies are then compared to determine the accuracy of the repair. This procedure is carried out for multiple different morphologies as depicted in Fig. 30. Here, repairs were performed on six different morphologies, three in the top row and three in the bottom row. The original reference morphology is shown on the left and the repair on the right for each morphology respectively. In the reference all dendrites that have been cut intentionally are marked in red with the black dendrites representing the cut morphology. The same is true for the repaired morphology, but here, the red dendrites represent the artificial repair instead. The blue shaded areas show the growth volume the artificial repair dendrites were allowed to grow in. The volume is determined by calculating the convex hull, using the built-in *convhull* function in MATLAB, of the dendrite material that has been cut off from the reference morphology. The volume is then enlarged by 10%, since dendrites growing into a set volume will end up occupying a smaller space. Therefore, without any enlargement the repaired dendritic arbor would always be too small. The graphs beneath each repair comparison, with the reference on the left and the repair on the right respectively, show the Sholl-profile (Sholl (1953)) for the cut, the repaired and the reference morphology. The repairs in Fig. 30 are performed using the incomplete growth mode which allows dendrites to only grow from specified incomplete ends. Therefore, the repair simulates the situation where dendrites that are known to exist but were somehow lost (for example, during the reconstruction process) are restored resembling reality as closely as possible.

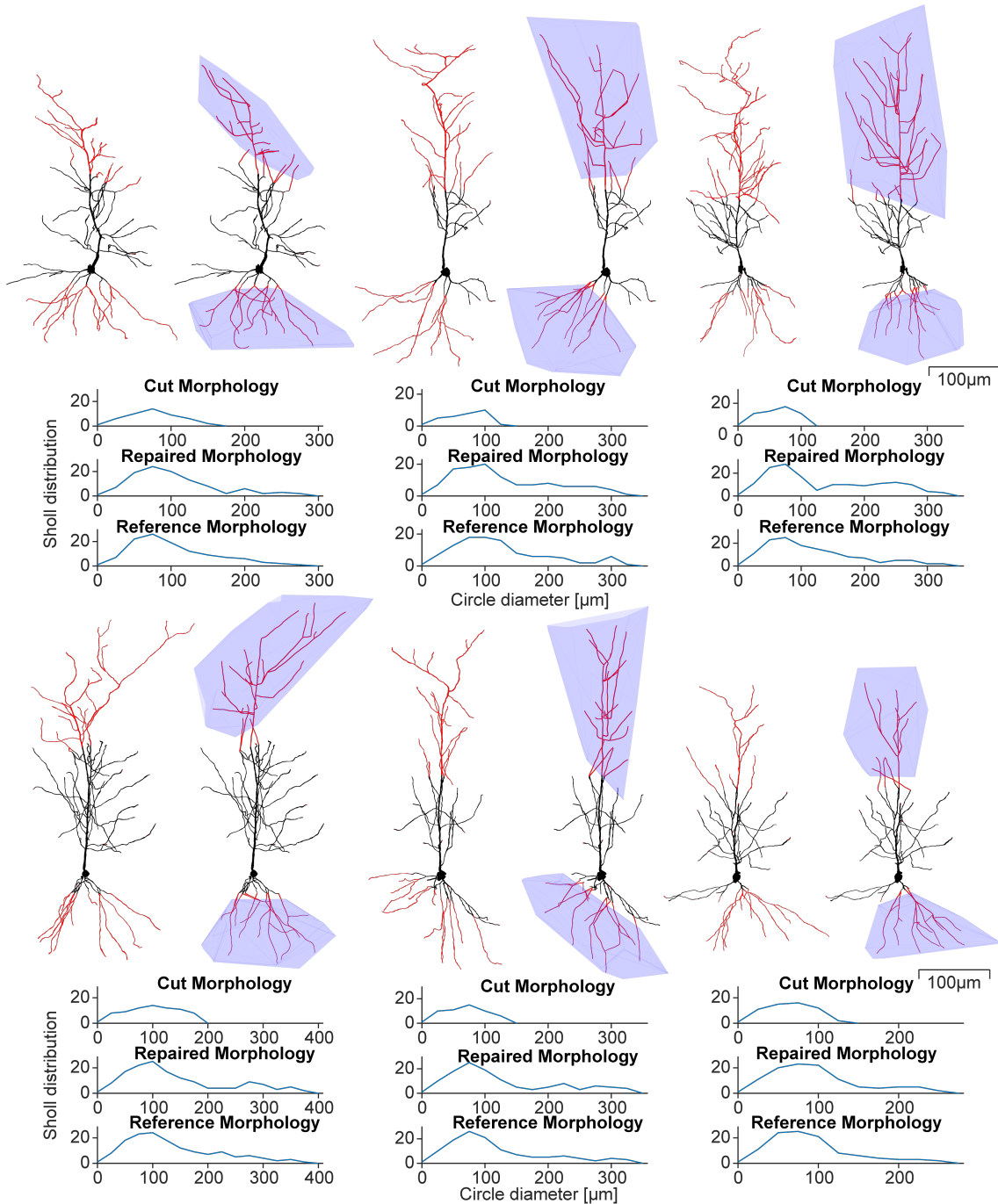


Figure 30. Successful repair of artificially damaged mouse CA1 pyramidal neurons

Six example repairs of mouse CA1 pyramidal neurons, reconstructed from the images in Fig. 11. The original reference morphologies have been cut intentionally in the basal and apical arbor and then repaired (Reconstructions by Benavides-Piccione et al. (2020)). For each repair, the left neuron depicts the reference and the right the repair. The input neuron is marked in black, with all red dendrites having been cut for the reference and artificially grown for the repaired morphology. The blue shaded areas represent the convex hull of the cut dendrites enlarged by 10%. Underneath each repair, the graphs show the Sholl intersection distribution for the cut, the repaired and the reference neuron. The repairs try to resemble the reference morphology as closely as possible.

The coordinates of the incomplete ends are specified in the morphology file, since they are well known due to the intentional lesion of the reference morphology. Since pyramidal neurons feature a prominent main apical dendrite in their apical dendritic arbor (Benavides-Piccione et al. (2020)), the main growth option (see Materials and methods **Chapter 4**) is engaged for the repair of the apical dendrites in Fig. 30. The main apical dendrite is severed in the proximal to distal area of the neurons in all cases in Fig. 30. With the main growth option, the main apical dendrite is grown first, followed by the rest of the dendritic arbor.

Fig. 30 showcases how the repair algorithm is capable of recovering dendritic material that was lost. The overall shape of the repair matches the reference accurately in both the apical and the basal arbor. Additionally, the Sholl-profile is also replicated well. Comparing the repaired Sholl-profile to the reference shows that the match is not perfect in every location. However, the improvement with respect to the cut version of the neuron is substantial. The Sholl-profile also reveals that dendrites reach the same points in space in the repair as they do in the reference, sitting in between $300\text{-}400\mu\text{m}$ for all morphologies in Fig. 30. The size of the artificially extended dendrites is limited by the growth volumes as indicated by the blue shaded areas.

In terms of analysing the morphological accuracy of a repair, it is particularly important to compare overall shape and appearance of a neuron as well as statistics associated with morphology simultaneously. This is due to the fact that matching statistics do not necessarily imply matching morphological shape and vice versa. Therefore, the information provided by the graphs of Fig.31, is very much complementary to the depictions of the morphologies in Fig.30. The graphs in Fig.31 show different statistical aspects of the morphologies depicted in Fig.30. Since the desired number of branch points is known due to the existing reference morphology, the algorithm matches the number of branch points to fit the repaired morphology exactly. This is shown in the first graph on the left side of the top row, by plotting the total number of branch points of the repair against the reference (blue data points). A point lying on the 45° angle ledger line indicates a match, as demonstrated by the blue points, which all lie on the line in this first graph. For the sake of a before-after comparison, the same measure for the cut morphologies is plotted against the reference in red. The red points do not lie on the 45° line indicating a miss match in this particular metric. All the graphs depicted in Fig. 31 share the same style with the 45° ledger line indicating matching statistics.

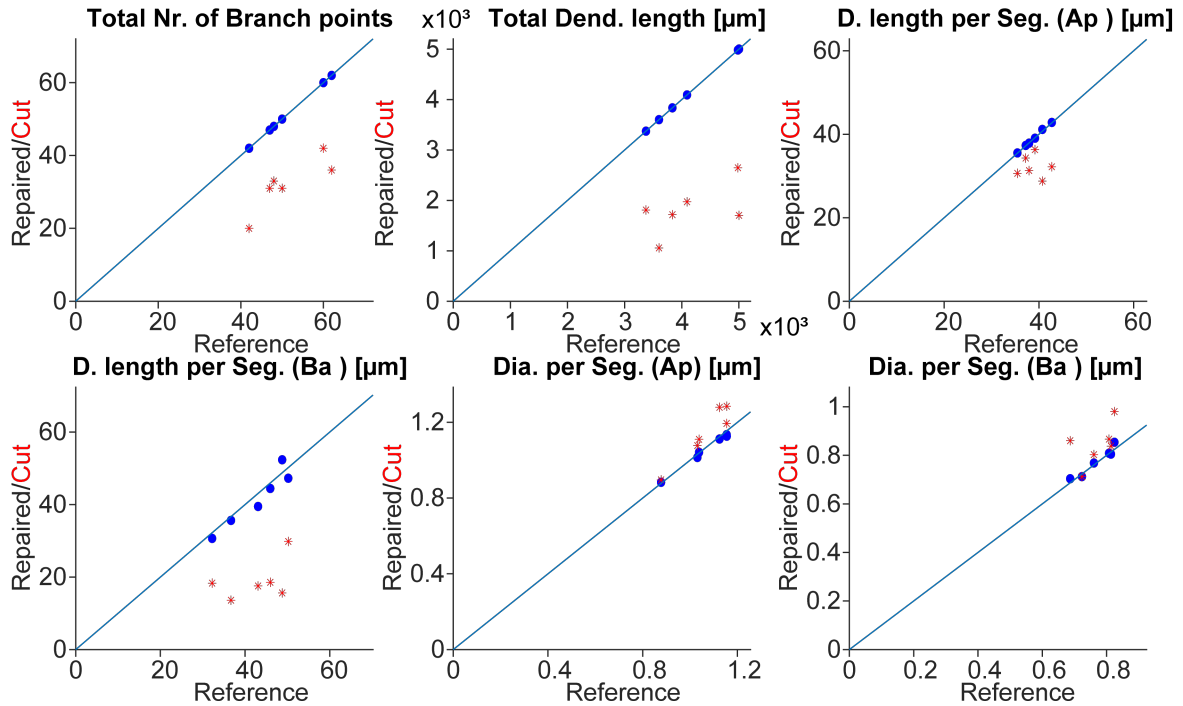


Figure 31. Statistics for the main features of dendrite morphology shows a successful recovery of lost dendrites

The graphs depict the morphological statistics of the repairs from Fig. 30. The values for the repaired morphologies are plotted against the reference, shown in blue. The statistics for the cut morphologies are plotted against the reference in red. The ledger line at a 45° degree angle signifies a match between the two morphologies. Points that lie close to this line indicate a close match. For the first graph (top left), showing the statistics for the total number of branch points, the blue points lie exactly on the line since the algorithm fits the repair to match that statistic exactly. The other graphs depict the total dendritic length (top middle), the dendritic length per segment (apical)(top right), the dendritic length per segment (basal)(bottom left), the diameter per segment (apical)(bottom middle) and the diameter per segment (basal)(bottom right).

With a matching number of branch points, the model tries to match the total dendritic length of the repair to the reference as accurately as possible. The graph in the top middle of Fig. 31 shows that matching the total dendritic length works well in most cases as all blue data points lie on the ledger line again. Unsurprisingly, the red data points for the cut morphology are far from matching the reference.

The next four graphs in 31 measure the average dendritic length or the average diameter of the different segments in a dendrite. A dendritic segment is measured as a continuous dendrite cable from one branch point to the next as depicted in Fig. 32 which shows two example segments in red and blue.

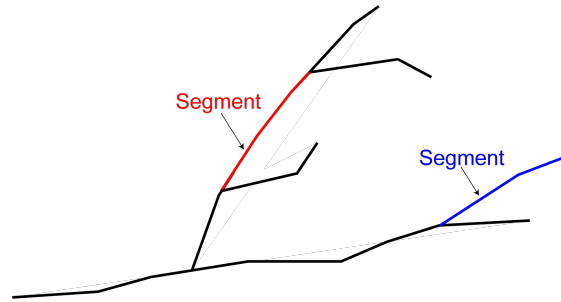


Figure 32. Dendritic segment definition

Skeletonized hypothetical dendrite with two example segments in red and blue.

The graphs in Fig. 31 show the average dendritic length per segment and the average diameter per segment for the apical and basal dendritic arbor separately. Fitting the first two properties, the total number of branch points and the total dendritic length exactly, causes the last four properties to fall into place accurately as depicted in Fig. 31. The fit for the dendritic length and diameter per segment is mostly very close to a match, improving the cut morphology by a large margin most of the time. According to these results, the neuron repair tool is capable of accurately reproducing the overall appearance and morphological statistics of CA1 pyramidal neurons of the mouse.

5.3.3 Repairing human CA1 pyramidal neurons

Since the main objective of the neuron repair tool introduced in this thesis is to repair damaged human morphology reconstruction, it was tested on human CA1 pyramidal neurons. This section demonstrates how a data set of human neurons can be repaired, in case a neuron sustains any form of damage. A neuron can even be extended, meaning that artificial dendrites are grown beyond the fully reconstructed neurons, where there are supposed to be dendrites. The data set of human CA1 pyramidal neurons was provided by Benavides-Piccione et al. (2020) and is shown in Fig. 33. Panel **A** shows a mosaic con focal microscope image of the CA1 region of the human hippocampus, with the dentate gyrus (DG) on the left. The layers of the CA1 region are marked out as SLM (stratum lacunosum moleculare), SR (stratum radiatum), SP (stratum pyramidale) and SO (stratum oriens). The region of interest, the morphologies were taken from, is marked by a rectangle and magnified in panel **B**.

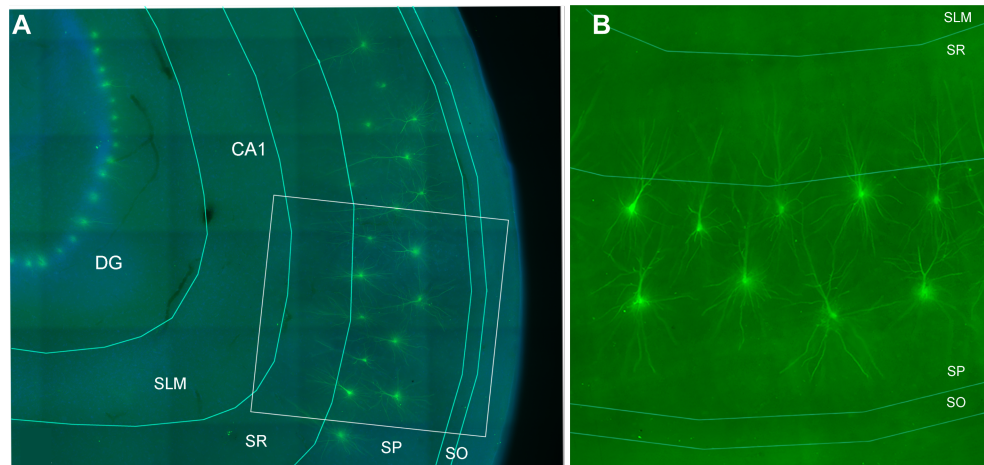


Figure 33. Human CA1 pyramidal neuron data set

Confocal microscope images of the human CA1 pyramidal neuron data set by Benavides-Piccione et al. (2020). **A**, Image of the hippocampal region with stained morphologies and marked out layers of the CA1 region (stratum oriens (SO), stratum pyramidale (SP), stratum radiatum (SR), stratum lacunosum moleculare (SLM)). Dentate gyrus (DG). The region of interest (ROI) is framed by a rectangle. **B**, Magnified ROI with stained pyramidal morphologies and marked layers.

The neurons' somata are located in the SP layer. Their apical dendritic arbor easily reaches into the SR layer but barely stretches far enough to touch the SLM layer.

The neurons in Fig. 33 were reconstructed resulting in digital 3D morphologies that are depicted in Fig. 34 A, where they are an overlay to a black background image which marks out the layers of the CA1 region like in Fig. 33 B. The morphology reconstructions are colour coded, such that each neuron can be identified by its specific colour throughout Fig. 34. Panel **B** shows the same neuron reconstructions from panel **A**, but they have been cut intentionally in their dendritic arbors, which have then been repaired. The repairs have been fitted to match the original reconstruction using the same procedure applied to mouse CA1 pyramidal neurons in **Chapter 5.3.2**. The repaired neurons are depicted as an overlay to the microscope image of the region of interest from Fig. 33 B. Panels **A** and **B** of Fig. 34 are a side by side comparison of the original morphologies and the repairs, which resemble the appearance of the original morphologies very well.

The original morphology reconstructions (Fig. 34 A) reportedly lack dendrites in the tuft area, which is the most distal region of the apical dendrite (Benavides-Piccione et al. (2020)). Due to the positioning of the morphologies in the image stack that was taken from cut tissue, the basal dendrites of these neurons have sustained damage during tissue sectioning.

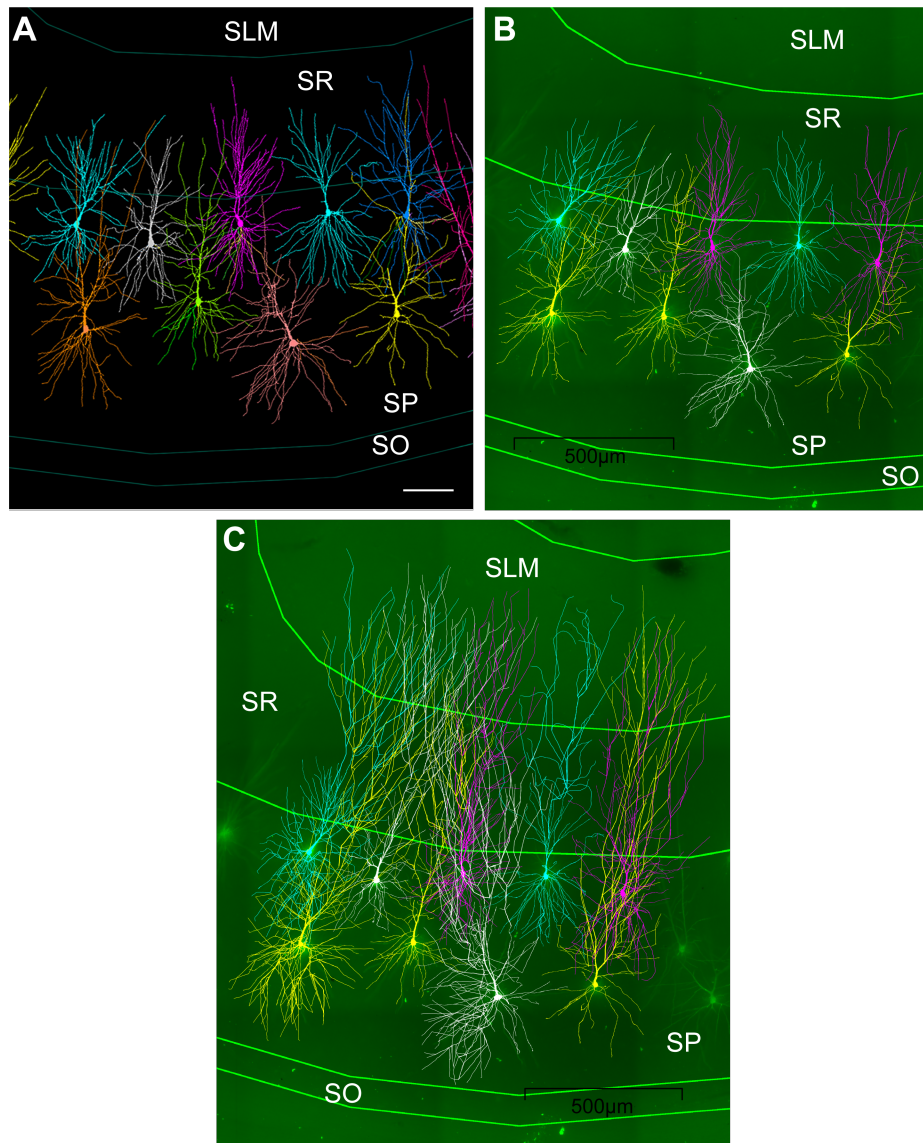


Figure 34. Repairing human CA1 pyramidal neurons

Human CA1 pyramidal neuron repairs and extensions. **A**, Reconstructions of the human CA1 pyramidal neurons shown in Fig. 33 B, overlaid on a black background with marked CA1 layers. **B**, The morphologies from **A** have been cut intentionally and then repaired using the neuron repair tool. The growth volume was calculated by taking the convex hull from the cut off dendrites enlarged by 10% (same procedure as in Fig. 30). **C**, The morphologies from **A** have been extended. The original reconstructions were left untouched and artificial new dendrites were added to the apical and basal arbors. The region where dendrites were missing and should therefore be extended were chosen in accordance with the expert opinion of Benavides-Piccione et al. (2020).

To complete the missing parts of the dendritical arbors of the original reconstructions from Fig. 34 A, the repair algorithm was applied. The results are depicted in Fig. 34 C, where entirely

new regions have been added to the full reconstructions by growing artificial dendrites. Neurons with somata located close to the edge of where SP meets SR should theoretically extend their apical dendrites more than halfway into the SLM layer, which is due to axons from the perforant path providing synaptic input in this region (Ito and Schuman (2012)). Neurons with somata located far away from the border of SP and SR will not reach deep into the SLM layer. Panel C of Fig. 34 shows the results of the human CA1 pyramidal neurons that have been extended using the repair tool. These repaired/extended neurons now feature dendritic arbors that cover the area of the CA1 region much better than the reference morphologies in panel A.

5.3.4 Electrophysiology in repaired human and mouse cells and differences between the two species

When recovering the morphology of an incomplete neuron, the goal is to reestablish its morphological appearance, statistic as well as its electrophysiological properties. The electrophysiological behaviour of a neuron in conjunction with detailed understanding of the brain's network will be key to understand how the brain works. For this reason, the repair algorithm introduced in this thesis was used to recover the morphology of a neuron, testing whether it was possible to recover the electrophysiological behaviour as well. Therefore, neurons were sectioned intentionally and then repaired to match the original reference neuron's morphology like in **Chapter 5.3.2**. The firing behaviour of these neurons was simulated by performing somatic current injections. These current injections were simulated using a compartmental model by Jarsky et al. (2005). The results are depicted in Fig. 35. The example shown in panel A is a mouse CA1 pyramidal neuron, whereas panel B depicts a human pyramidal neuron repair. The reference neuron is shown on the right and the repair on the left respectively, with the cut and repaired dendrites marked in red. The current clamps are performed with five different increments of increasing intensity, with the firing responses plotted for the reference, the repaired and the cut neuron morphology. Each current clamp lasts for $500ms$. The firing behaviour of the intentionally cut neuron is significantly different from the reference and the repaired neuron, in both human and mouse respectively as demonstrated in Fig. 35 A and B. The cut morphologies produce spikes at currents where both the reference and repaired neuron do not fire at all.

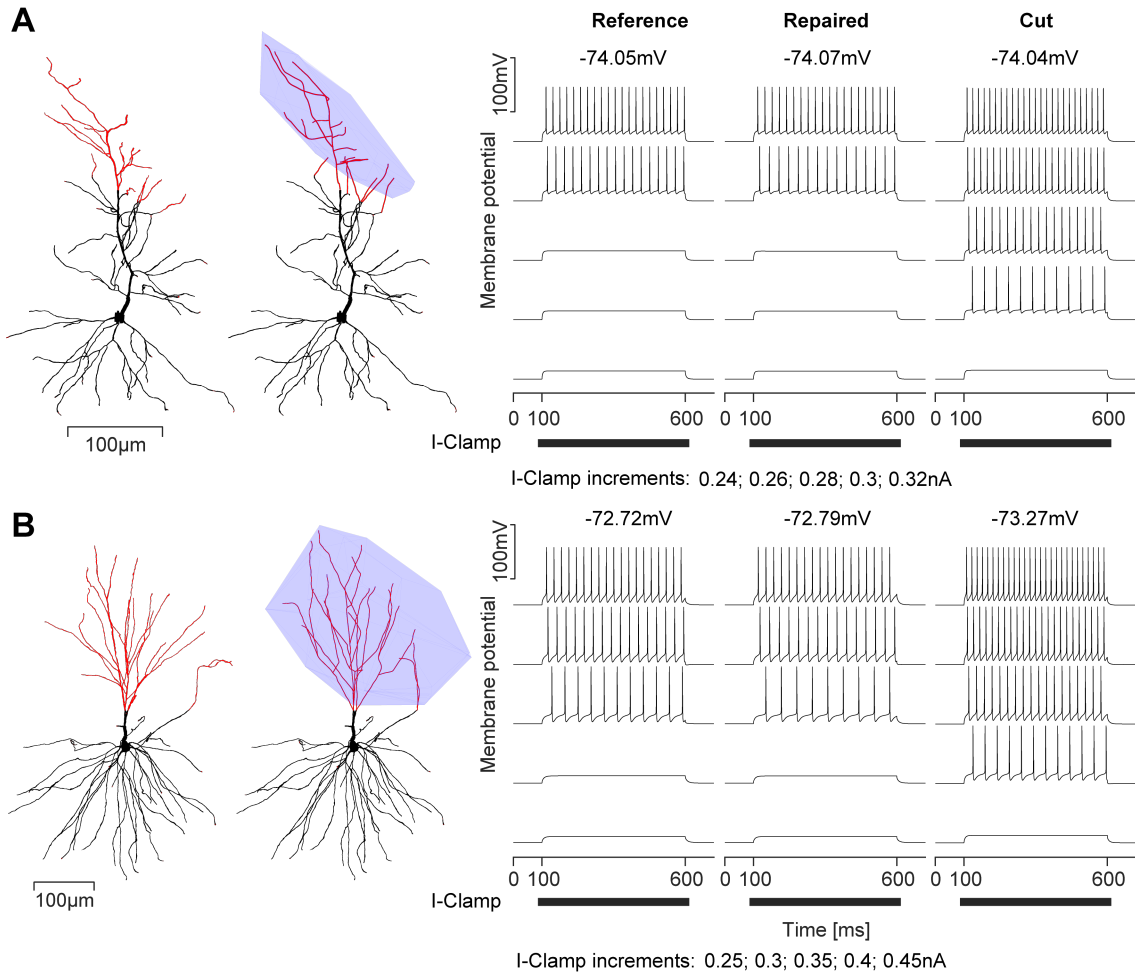


Figure 35. Repairs recover a neuron's original firing behaviour

Repaired neurons with the neuron repair tool recover their original firing behaviour. **A**, The reference mouse CA1 pyramidal neuron on the left has been sectioned in the apical arbor (sectioned dendrites in red). The cut dendrites have then been repaired using the same method as in Fig. 30 in the morphology on the right (repaired dendrites in red, growth volume in blue). In silico somatic current clamp experiments were performed on the reference, cut and repaired morphology, using a compartmental model by (Jarsky et al. (2005)). The graphs on the right show the voltage traces for each morphology with their resting membrane potential above the traces. The current increments are depicted below the graphs. Each current clamp lasts for 500ms, as indicated by the black bars. **B**, Same experiment layout as in **A**, but for a human CA1 pyramidal neuron.

The firing behaviour of the repaired neuron is very reminiscent of the reference neuron, unlike the firing rate of the cut neuron.

Since the neuron repair tool is able to recover the electrophysiological behaviour of the original reference morphology in the repaired morphology as demonstrated in Fig. 35 for both species, it is of great interest to analyse what separates human neurons from mouse neurons.

Both morphological and electrophysiological aspects are of importance here, since, as shown in Fig. 35, morphology and therefore morphological repairs do have a significant impact on electrophysiological behaviour. Understanding such differences in electrophysiology and morphology between human and mouse can teach us about how the human brain achieves superior cognitive abilities (Schmidt and Polleux (2022)). Unfortunately, for the CA1 pyramidal cell data set provided by Benavides-Piccione et al. (2020), there is no data from electrophysiological patch clamp experiments available. This means extracting any electrophysiological properties from voltage traces recorded directly from these neurons is not possible. To compensate for this lack of data, another data set of human granule cells from the dentate gyrus, which is a region of the hippocampus, is utilised. The data set is provided by Buchin et al. (2020) and includes 24 human granule cell morphologies with voltage traces from whole-cell patch clamp experiments. An example morphology and voltage trace is shown in Fig. 36 top. The following section analyses the passive electrophysiological properties of the human granule cells and compares them to findings in mouse granule cells. The analyses of the electrophysiological properties was done in association with two students of the Cuntz lab at ESI (Ernst-Strüngmann-Institut) Frankfurt am Main, Lina Eicke and Alicia Strosche. Additionally, the morphological differences between mouse and human granule cells as well as mouse and human CA1 pyramidal neurons are compared. The granule cell morphologies were taken from patients with temporal lobe epilepsy. This pathological condition is associated with hippocampal sclerosis (HS, for details see Buchin et al. (2020)), which is why the granule cell morphologies were quantified neuropathologically using the Wyler grade (WG) system (Wyler et al. (1992)). A WG of degree 1 (WG1) corresponds to no or mild HS, while WG3 and WG4 indicate severe cases of HS. For this reason, the passive properties of the granule cells will additionally be displayed and compared as they are separated by Wyler grade.

The voltage traces from current clamp experiments recorded directly from the neurons of the data set provided by Buchin et al. (2020) allow for the calculation of passive properties of the human granule cells. The resting membrane potential V_{rest} , the input resistance R_{in} and the membrane time constant T_m can be extracted from the voltage traces by linearly fitting sections of the voltage trace to obtain V_{rest} and the stimulated membrane potential V_{stim} (Fig. 36 top right). The time it takes for the membrane potential to reach $1 - e^{-1}$ of the difference between V_{rest} and V_{stim} determines T_m .

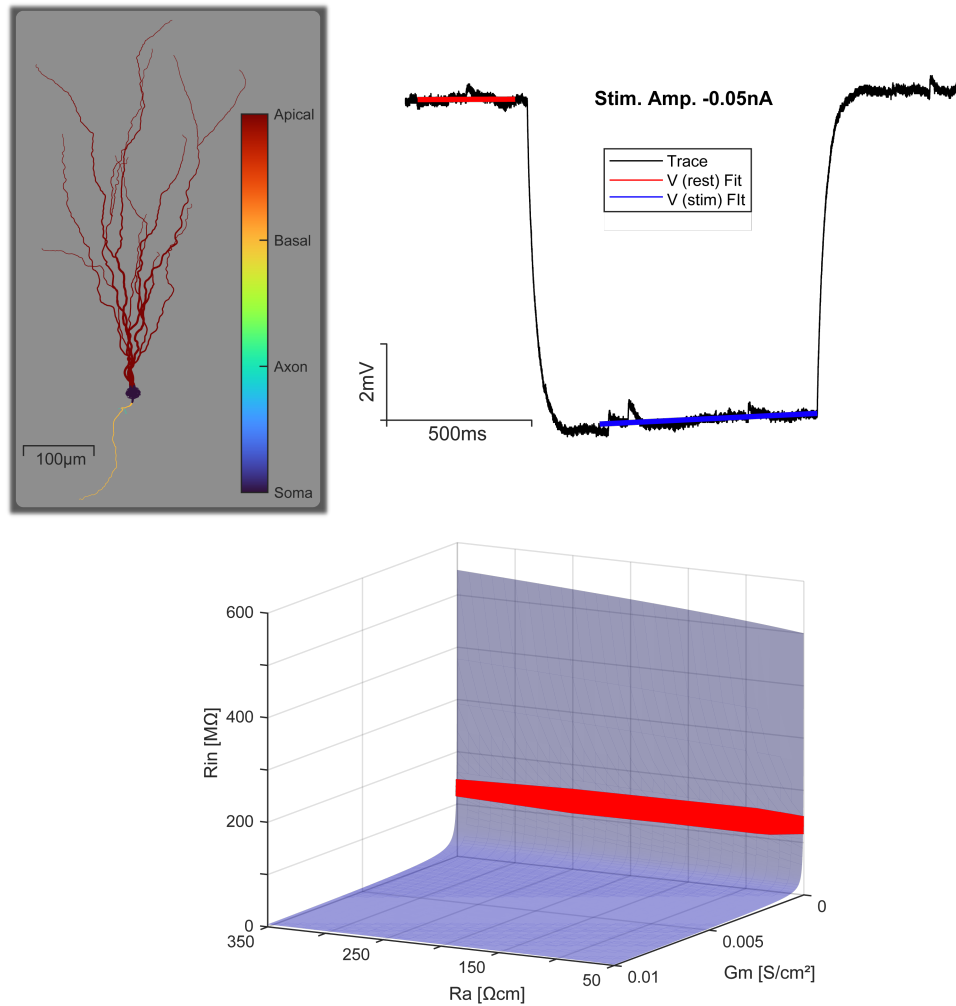


Figure 36. Human dentate gyrus granule cell morphology and passive property simulation

Top left, Example human dentate gyrus granule cell morphology provided by Buchin et al. (2020). Dendritic regions are marked out by the colour code. **Top right**, Example human granule cell voltage trace (current injection amplitude $-0.05nA$) with fits for the resting membrane potential V_{rest} (red) and the V_{stim} stimulated membrane potential (blue). **Bottom**, Parameter space of the simulation using the *sse_tree* function. The possible values for the axial resistance Ra and the membrane conductance Gm produce simulation values for Rin (blue sheet). Values for Ra and Gm that produce acceptable values of Rin (within two standard deviations of Rin calculated from the voltage traces) are marked by the red stripe.

Based on the voltage trace-based estimate of Rin , Ra (axial resistance) and Gm (membrane conductance) can be calculated using a parameter scan that simulates the observed Rin with the help of the *sse_tree* function of the TREES toolbox. The simulation is done for possible values of Ra and Gm that produce a fitting value for the observed range of Rin values (Fig. 36 bottom).

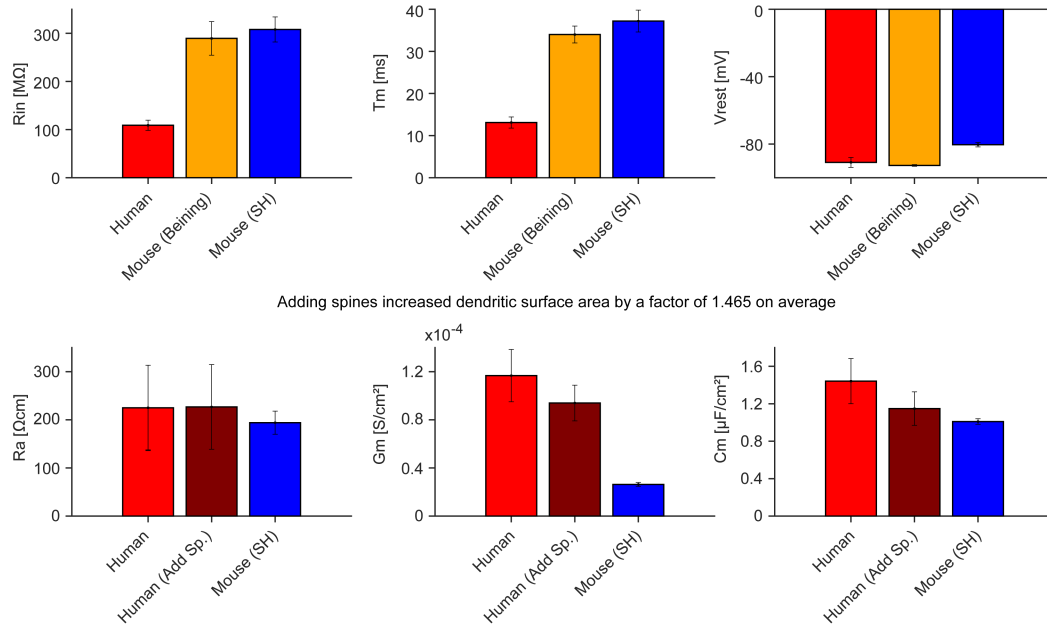


Figure 37. Passive electrophysiological properties of human and mouse dentate gyrus granule cells

Top, From left to right: input resistance R_{in} , membrane time constant T_m and membrane resting potential V_{rest} (Beining: values taken from Beining et al. (2017), SH: values taken from Schmidt-Hieber et al. (2007)). **Bottom**, From left to right: axial resistance R_a , membrane conductance G_m , membrane capacitance C_m . These three properties have been calculated using the `sse_tree` function of the TREES toolbox (see Materials and methods **Chapter 4**). Add Sp.: artificial spines have been added to the reconstructed morphology using the TREES toolbox. The data shown for the human GCs is from the 3 morphologies rated WG1 (mild/no HS) in the data set.

Fig. 37 shows the passive properties of the 3 (healthy) cells from the data set that were rated WG1 by Buchin et al. (2020). The top row of graphs in Fig. 37 depicts R_{in} , T_m and V_{rest} . These properties are extracted from traces with a relatively small negative stimulation current, since little to no active ion channels are involved in this interaction (see Materials and methods **Chapter 4**), leaving only the passive response of the neuron. As demonstrated in Fig. 37, compared to a mouse granule cell (compare Beining et al. (2017) and Schmidt-Hieber et al. (2007)), a human granule cell exhibits a much lower R_{in} . This is likely due to the larger size of the human neuron. A lower input resistance decreases the cell's excitability following Ohm's law $U = R \cdot I$, as the voltage deflection decreases with lower R at constant I . To compensate for a decreased excitability, human granule cells feature a lower input latency, expressed in a decrease in the membrane time constant T_m . The membrane resting potential V_{rest} is, however, similar across both species, regardless of the difference in neuron size and R_{in} .

The following properties of the human granule cells in the bottom row of Fig. 37 have been calculated according to the method depicted in Fig. 36 bottom. As the reconstructed morphologies do not feature any synaptic spines, which lowers the surface area of the reconstructions, the calculations have been carried out two times. Firstly, the properties were simulated for the original reconstructions ("Human" in Fig. 37) and secondly, artificial spines were added to the reconstructions using the TREES toolbox ("Human (Add Sp.)" in Fig. 37). A spine control factor to compensate for the reduced surface area because of absent spines was proposed by Schmidt-Hieber et al. (2007) to be in the range of 1.7 to 2.3 for mouse granule cells. However, the density of spines in human granule cells is lower than the density of spines in mouse granule cells, increasing the surface area in human granule cells by a factor smaller than 1.7. Therefore, artificial spines were added to the morphologies according to the observed spine densities by Buchin et al. (2020) (see Materials and methods **Chapter 4**). Out of the 24 human granule cell morphologies, the spine densities as well as the Wyler grades are only recorded for 6 individual reconstructions. Therefore, the sample size for the passive properties of relatively healthy human granule cells with added artificial spines in Fig. 37 is only equal to 3 (3 of the 6 cells are rated WG1) rather than 24. The range of possible values for the axial resistance R_a is very large as indicated by the error bars in Fig. 37 and the graph in Fig. 36 bottom. This means that almost any value of R_a paired with a suitable candidate for the membrane conductance G_m will lead to a fitting value of R_{in} as extracted from the voltage traces. Therefore, the values for R_a in human granule cells in Fig. 37 are all very similar, even with artificially added spines. R_a in mice seems to be slightly decreased compared to humans according to Schmidt-Hieber et al. (2007). The membrane conductance G_m is significantly increased in humans compared to mice as shown in Fig. 37. G_m is the inverse of the membrane resistance $R_m = 1/G_m$, which is decreased due to the also rather low R_{in} of human neurons. With a low resistance the conductance, being the inverse, rises. When adding artificial spines, the surface area of a reconstruction increased by a factor of 1.465 on average. This results in G_m not being halved (as it would be the case with a spine control factor of 2 applied to R_m) but decreased by a factor 0.67 compared to the original morphologies in Fig. 37. Together with T_m the membrane capacitance C_m can be calculated as $C_m = T_m/G_m$. The expected value for C_m is $\approx 1\mu F/cm^2$, following the hypothesis that C_m is a natural constant (Curtis and Cole (1938)). While the data by Schmidt-Hieber et al. (2007) seems to confirm this as shown in Fig. 37, there have been some studies reporting lower values of C_m , especially for human neurons (see Discussion **Chapter 6**).

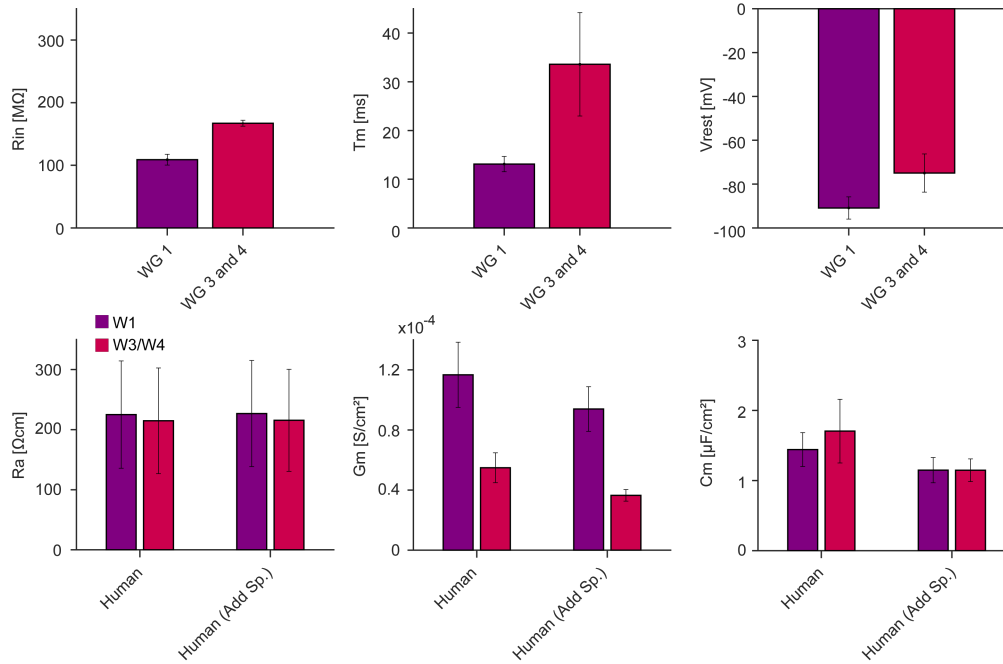


Figure 38. Passive electrophysiological properties of human dentate gyrus granule cells separated by Wyler grade

Top, From left to right: input resistance R_{in} , membrane time constant T_m and membrane resting potential V_{rest} (WG: Wyler grade). WG 1 represents no or mild HS (hippocampal sclerosis). WG 3 and 4 indicate severe HS. **Bottom**, From left to right: axial resistance R_a , membrane conductance G_m , membrane capacitance C_m . These three properties have been calculated like in Fig. 37. Add Sp.: artificial spines have been added to the reconstructed morphology using the TREES toolbox. W1 (Wyler grade 1) and W3/W4 (Wyler grade 3 and 4) are indicated by the colour code.

The values of C_m for human granule cells depicted in Fig. 37 are, like those of the mouse, close to $1\mu F/cm^2$. C_m for the original human morphologies without any compensation for the lack of spines is, however, much larger, with $C_m \approx 1.72\mu F/cm^2$. Therefore, with proper compensation for the lack of spines, this analysis finds C_m of human granule cells to be within the same range as C_m of granule cells in the mouse. As mentioned earlier, the data set of human dentate granule cells contains morphologies with different Wyler grades (WG) or levels of hippocampal sclerosis (HS). Fig. 38 illustrates how electrophysiological properties of neurons with WG1 differ from neurons with WG3 and WG4. Fig. 38 consists of the data from the 6 individual morphologies, for which the Wyler grade as well as the spine densities were recorded (3 morphologies for WG1 and 3 for WG3/WG4) as mentioned before. The differences seem to be very reminiscent of the differences between human and mouse granule cells depicted in Fig. 37. Human granule cells with severe HS (WG3 and WG4) exhibit passive

electrophysiological properties that are more mouse-like than their WG1 counterparts. R_{in} is increased in WG3/WG4 leading to increased excitability in accordance with Ohm's law. At the same time T_m is also increased like in the mouse granule cell. V_{rest} sees a slight decrease in WG3/WG4 but is still within close range of WG1. As expected, the axial resistance R_a is constant within Wyler grades even with artificially added spines, since like in Fig. 37 a wide range (error bars) of values is acceptable to fit the values for R_{in} . Interestingly, G_m is significantly decreased in WG3/WG4, to the point where the value for the original morphologies in Fig. 38 is in the same range as the values for human granule cells with artificial spines in Fig. 37. The values for G_m in Fig. 38 for WG3/WG4 seem to be decreased in such a way that they can compensate for the increase in T_m , to produce a similar membrane capacitance C_m for both WG1 and WG3/WG4 ($C_m = T_m/G_m$). This is true for morphologies with artificial spines as well. As illustrated in Fig. 35, the morphological features of a neuron heavily impact its electrophysiological behaviour. Therefore, Fig. 39 compares the morphological properties of the mouse and human neurons that had their passive electrophysiological properties analysed in Fig. 37 and 38. Additionally, the morphological features of the mouse and human CA1 pyramidal cells used to validate the neuron repair tool are depicted as well. The total dendritic length as well as the mean dendritic diameter of human neurons is significantly larger than in mice, for both granule and CA1 pyramidal neurons.

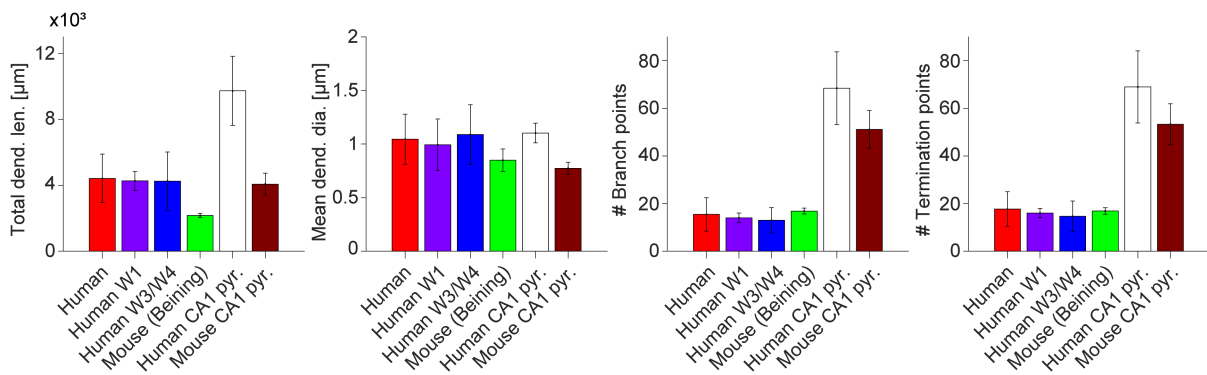


Figure 39. Comparing morphological properties of mouse and human granule and CA1 pyramidal neurons

From left to right: Total dendritic length (apical and basal); Mean dendritic diameter (apical and basal); Total number of dendritic branch points; Total number of dendritic termination points. Human: Human granule cells, Human W1: Human granule cells with Wyler grade 1, Human W3/W4: Human granule cells with Wyler grade 3 or 4, Mouse (Beining): Mouse granule cells from Beining et al. (2017), Human CA1 pyr.: Human CA1 pyramidal cells from Benavides-Piccione et al. (2020) (morphologies depicted in Fig. 34 A, Mouse CA1 pyr.: Mouse CA1 pyramidal cells from Benavides-Piccione et al. (2020) (morphologies depicted in Fig. 30.)

This explains the lower input resistance R_{in} in human granule cells compared to mice (Fig. 37), since a smaller cell poses more resistance to an incoming current than a larger one. Differences in Wyler grade seem to have no impact on both total dendritic length and mean diameter. Interestingly, while the difference in dendritic length is substantial between CA1 pyramidal neurons and granule cells, the mean dendritic diameter is similar for both cell types in the respective species. The dendritic length in a human granule cell is ≈ 2.04 times larger than in a mouse granule cell. For CA1 pyramidal neurons, the difference in dendritic length is governed by a similar factor of ≈ 2.3911 . Since the dendritic length of mouse CA1 pyramidal neurons is similar to that of human granule cells, one could assume that they exhibit a similar input resistance as well. This is, however, unlikely due to the low dendritic diameter in mouse neurons. The number of branch and termination points is a measure of neuronal complexity. In this regard CA1 pyramidal neurons are significantly more complex than granule cells (Fig. 39 right). Additionally, in pyramidal neurons, human morphologies are exceedingly more complex than those of mice. On the flip side, in granule cells, complexity does not seem to differ between humans and mice. A possible explanation for this could be that granule cells favour direct connections to the soma and therefore do not branch a lot. This explanation will be explored in further detail in the next section (**Chapter 5.3.5**), where different cell types are repaired using the neuron repair tool. To model different cell types, different sets of parameters, that govern how much the dendrites branch, have to be used in the model.

5.3.5 Repairing other cell types

The neuron repair tool is designed to be applicable to all neuron cell types besides just pyramidal cells, in the animal and the human brain. Using the TREES toolbox (Cuntz et al. (2010)) modelling different cell types can be done via just one parameter called the balancing factor bf . bf balances the need to minimise conduction time towards the soma, alongside maintaining a small wiring cost (see Fig. 10). Furthermore, the dendritic arbor of a neuron is set apart by the density profile of its spanning field. bf is estimated automatically by the repair algorithm (Bird and Cuntz (2019)), as well as the density profile of termination and branch points in the dendritic arbor of the input neuron that is supposed to be repaired. Carrier points are then distributed accordingly within the growth volume provided by the user.

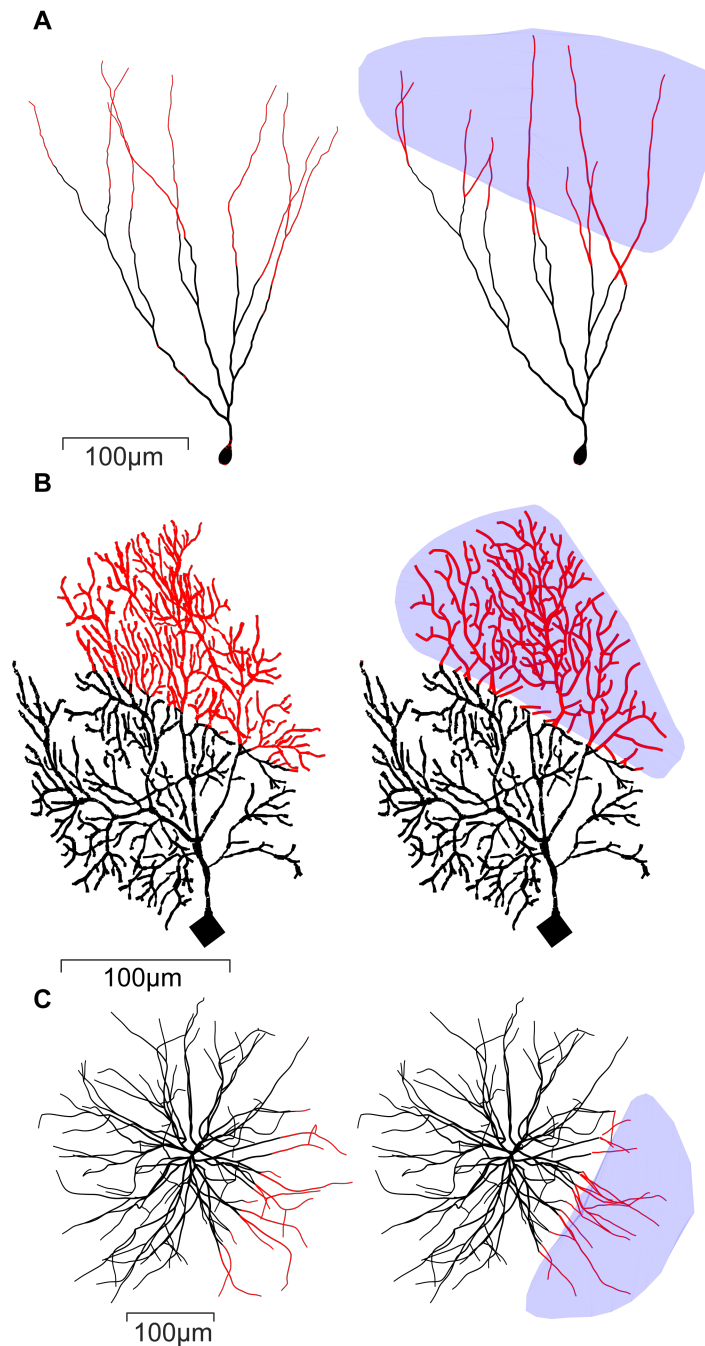


Figure 40. Repairing different cell types: hippocampal granule cells, cerebellar Purkinje cells and artificially grown cells

A, Granule cell of the mouse (Beining et al. (2017)). (Left) Reference morphology with intentionally cut dendrites marked in red. (Right) The morphology in black has been repaired with artificially grown dendrites marked in red. The blue shaded area marks the growth volume. **B**, Purkinje cell from the mouse (Chen et al. (2013)). Same layout as in **A** with the reference on the left and the repair on the right. **C**, Artificial spherical neuron grown with the TREES toolbox (Cuntz et al. (2010)). Layout like in **A** (reference on the left, repair on the right).

These carrier points are the framework used by the MST algorithm of the TREES toolbox to grow into. The number of carrier points is dependent on the size of the growth volume as well as on the density profile of the dendritic arbor of the input neuron. These parameters calculated automatically by the repair tool can also be adjusted manually if needed (see Materials and methods **Chapter 4**). By using different values for bf and different densities and numbers of carrier points, different cell types can be modelled and therefore be repaired by the algorithm. Fig. 40 shows examples of such repairs that are not pyramidal cells. Panel **A** depicts a granule cell of the mouse (Beining et al. (2017)). Like in Fig. 30, the original reference morphology is shown on the left, with the intentionally cut part of the dendrite marked in red. The repaired version is shown on the right, with the blue shaded area representing the growth volume and the artificially extended dendrites marked in red. The granule cell typically favours low conduction time over minimal wiring cost and can therefore be modelled using a high bf value. The carrier point density distributed in the growth volume is relatively low. A purkinje cell on the other hand tends towards the other end of the spectrum, minimising wiring cost rather than conduction time. Panel **B** shows an example repair of a mouse purkinje cell (Chen et al. (2013)) that uses a low bf value. Compared to the granule cell, the density of carrier points is much larger in the purkinje cell. As illustrated by panel **B**, this configuration leads to a lot of branching. The layout of panel **B** is the same as in panel **A**. The last panel **C** of Fig. 40, which has the same layout as the previous ones, depicts a spherical, fully artificial neuron produced by the MST of the TREES toolbox. As a proof of concept, this neuron has been intentionally cut and repaired in the same way as the others. The incomplete growth mode was used for the repairs of the cells depicted in Fig. 40, repairing a part of the dendrite that is known to exist.

5.3.6 Biological repair of class IV da-neurons of *D. melanogaster*

To investigate the development of dendrites and dendriotomy, the class IV da neurons of the *Drosophila* fly are used as a model. The objective here is to reproduce experimental findings in dendriotomy by Song et al. (2012), Li et al. (2018) and Stone et al. (2014), mimicking real neurons of *Drosophila*. This was done using five reconstructions of class IV neurons (Song et al. (2012)) from the data base *neuromorpho.org* (Ascoli et al. (2007)). This project was inspired by the previous work done by two students of the Cuntz lab at ESI (Ernst-Strüngmann-Institut) Frankfurt am Main, Hannah Moessinger and Barbara Schaffran, who investigated

the biological regrowth of class IV *Drosophila* neurons using computational modelling. The class IV neurons had one branch cut off (lesion), leaving one cut off point defined as the incomplete node. The cell will then grow into the area left vacant by the lesioned branch. This would either happen by neighbouring branches 'invading' the space, or by a new branch sprouting from the incomplete node ('conserved branches'). This behaviour of the neurons can be simulated using the neuron repair tool. Using the biological growth mode, new dendrites can grow from any random point on the input morphology. Repairing the *Drosophila* neurons with the repair tool multiple times yielded a distribution of invasion and conserved regrowth. The repairs obtained by the algorithm were grouped depending on the fraction of invading

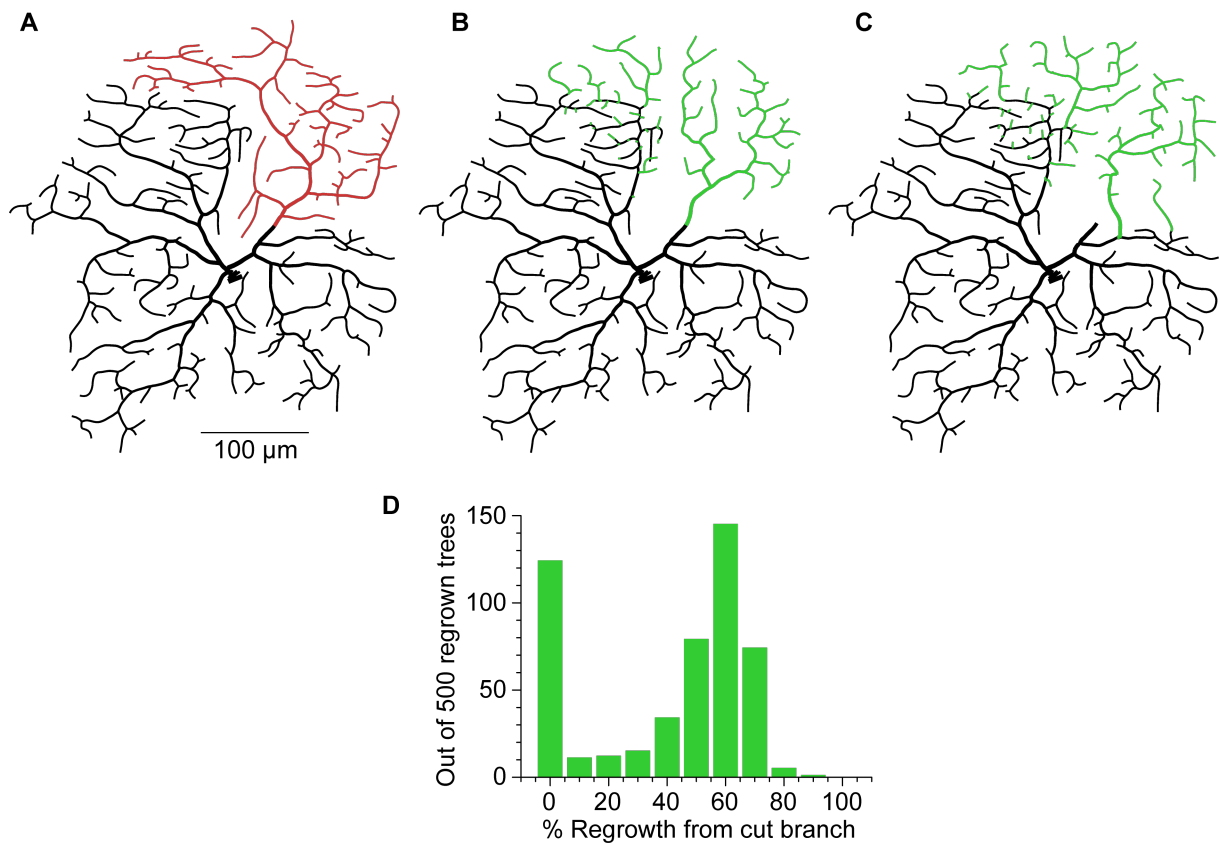


Figure 41. Biological regrowth using the neuron repair tool

Class IV neurons of *Drosophila* (Song et al. (2012)). **A**, Reference morphology with the intentionally sectioned branch marked in red. **B**, Biological regrowth using the neuron repair tool of the severed branch from **A**. In this case, the new dendrites grew mainly from the severed stem. **C**, Biological regrowth using the neuron repair tool of the severed branch from **A**. Here, the area left vacant by cutting the branch is invaded by new dendrites from neighbouring branches. **D**, Statistics of what percentage of the newly grown dendrites originates from the severed stem over 500 trials. This means applying the biological regrowth algorithm to the *Drosophila* neuron from **A** 500 times.

branches that regrew from neighbouring branches rather than from the incomplete node during the repair. Panels **A-C** in Fig. 41 show examples of biological regrowth performed on a class IV da-neuron of *Drosophila*, with the original reference morphology in panel **A**. Panel **B** shows an example of conserved regrowth originating from the incomplete node and panel **C** shows an example of invasion. The cut and repaired dendrites are marked in red respectively. If the removed branch represented approximately 25% of the total dendritic path length of the original neuron, conserved regrowth from the incomplete node tended to occur. Invasion was observed to occur in all neurons regardless of how much dendritic material was cut off. With more of the neuron's path length removed, invasion seemed to occur less. Predicting the amount of invasion was not possible. The distribution of conserved regrowth and invasion was of bimodal nature as depicted in Fig. 41 D that shows the percentage of regrowth from the cut branch out of 500 regrown neurons. The distribution features two distinct peaks at 0% of the regrown material originating from the cut branch and 60% of the material stemming from the incomplete node. This is in accordance with the research conducted by Song et al. (2012), who observed the same bimodal distribution. Over 60% of the artificially regrown morphologies displayed invasion when less than 25% of the total dendritic material of the original cell was cut. The 40% that remain displayed a degree of conserved growth, approximately 20% of the sectioned branches' total length.

The repair algorithm is therefore capable of reproducing biological regrowth. The regrowth simulates a neuron's capability of recovering/regrowing dendritic material in an area where its dendrites were damaged. The results show the same balance between invasion and conserved regrowth as experimental findings by Song et al. (2012).

6 Discussion

The two computer models introduced in this thesis aim to make a contribution to further our understanding of how the brain works. They achieve this feat in different ways. The macroscopic model of brain folding provides an explanation as to how gyrification emerges, what the differences between species are, how neural connectivity of the cortex on a local and global scale is constituted to produce the different levels of convolutions and how pathological diseases might impact gyrification. The interaction between diseases and gyrification will be discussed in more detail at a later stage of this thesis. The microscopic model provides a way to enhance research on neuron morphologies, especially human ones, by repairing incomplete morphologies, restoring their appearance and electrophysiological properties. This can be a means to improve the poor human neuron data situation, increasing the reliability and accuracy of these data sets, potentially revealing more of the subtle differences between human neurons and those of other mammals. It is applicable to all different cell types and features a biological regrowth mode.

6.1 What causes the brain to fold?

The model of gyrification introduced in this thesis reproduces the trend of increased cortical folding found in mammalian brains with increasing size (Zilles et al. (2013), Mota and Herculano-Houzel (2015), Hofman (1985)). The model also provides an explanation for outliers like the lissencephalic cortex of the manatee (Charvet et al. (2016)). The principles the model is build on are very simplistic. Neuronal placement is constraint by the demand that wiring length must be minimised (Laughlin and Sejnowski (2003), Wang and Clandinin (2016), Ruppin et al. (1993), Chklovskii and Koulakov (2004)). The model predicts folding patterns with different levels of gyrification for a connectivity distribution with strong local and sparse global connections. Such a connectivity is the result of a compromise also implemented by the real brain to optimise network performance with fast conduction time and global information processing (Bullmore and Sporns (2012)). According to the model, folding in larger cortices is likely to depend on their high number of columns C as they represent cortical size, compared to the number of neurons per column M , which is disproportionately low. Cortical thickness represented by M stays relatively constant. The level of gyrification in the model is however

critically dependent on connectivity parameters as well, suggesting that brain folding patterns with similar appearance could be defined by multiple parameters. Therefore, differences in cortical size, the number of neurons within a cortical column (cortical thickness), and connectivity work together to produce the intricate folding patterns we observe in the brain. Changing any of these parameters in the model in a local area leads to stereotypical folds emerging in these sections. These predictions by the model could explain the characteristic folds that appear on the cortices of mammalian brains.

The magnitude of the increase in Cortical folding with increasing brain size varies depending on connectivity parameters as demonstrated in Fig. 21. These differences in scaling were also observed in different orders of mammals (Mota and Herculano-Houzel (2015), Zilles et al. (2013), Pillay and Manger (2007)). Specifically γ changed the maximum slope of the sigmoidal fit significantly in the model. Since γ changes the rate of decay in global connectivity, future research should analyse the differences in global connectivity between mammalian orders. Specifically questions like how far global connections reach in the cortex and whether mammalian orders with strong scaling feature connections that span the maximum available distance in their cortices, could be interesting.

The differences in the scaling of the degree of folding between mammalian orders could also be the result of different cortical thicknesses (Mota and Herculano-Houzel (2015)). Thicker cortices in turn can be the consequence of larger neurons, which additionally lead to an increased width in local connectivity, since they span longer distances. Indeed, in rodents of increasing body size, the size of neurons and the width of local connectivity increases much more dramatically compared to primates (Elston and Manger (2014)). Therefore, the lower rate of gyrification scaling in rodents compared to other mammalian orders could be the result of a diminished number of neurons, columns and a broader local connectivity (Zilles et al. (2013), Pillay and Manger (2007)).

In the folding model, differences in the number of neurons per column and therefore cortical thickness influence the degree of folding significantly (Fig. 25 C). These variations could be an explanation as to why the degree of folding in humans and primates is not constant along the rostrocaudal axis (Toro et al. (2008), Toro (2012), Zilles et al. (1988), Zilles et al. (1989)). While the degree of folding in the rostral part of the cortex is lower than in the caudal part, the caudal part features larger numbers of neurons than the rostral part (Charvet et al. (2016), Charvet et al. (2015)). As depicted in Fig. 25 C, the model predicts the exact opposite for the degree of folding.

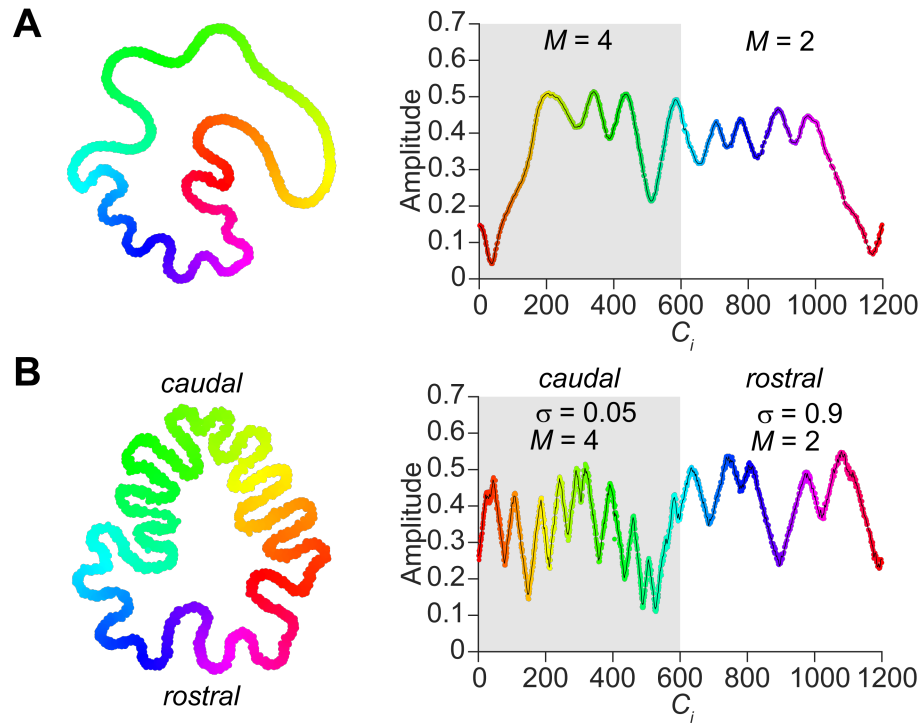


Figure 42. Rostrocaudal folding differences

(Note: Figure by Groden et al. (2019), Fig. S7) Changing connectivity can cancel out the effect of changing the number of neurons per column M . Folding parameters are fixed unless stated otherwise ($M = 2$, $C = 1200$, $\sigma = 0.9$, $a = 0.2$, $b = 1$, $\gamma = 1$). **A**, Example folding pattern on the left with folding amplitudes plotted on the right. M is changed in one region of the cortex compared to the other, as indicated by the shaded area. Dot colours indicate columns and position on the folding pattern. **B**, Another folding pattern with the same changing values of M as in **A**, but also changing values of σ (local connectivity). The differences in folding and connectivity mimic the situation in the rostral vs caudal part of the cortex.

The cortex is, however, much thicker in the rostral part than in the caudal part, which is associated with a decreased degree of folding (Zilles et al. (1989), Mota and Herculano-Houzel (2015), Pillay and Manger (2007), Welker (1990), Hofman (1985)). Interestingly, in the rostral region, cortical thickness is increased despite the low number of neurons per column. Since columns span the cortex vertically, less neurons per column should correlate with a thinner cortex and therefore increased folding. In primates and rodents the opposite is true, which is likely due to an increased neuron size in the rostral part of their cortex. As mentioned earlier, this can lead to a thicker cortex despite low numbers of neurons. Neurons of larger size are the only explanation since the size and number of glial cells is constant throughout the cortex (Herculano-Houzel (2014)). Elston (2000) and Elston (2003) actually found neurons in the

rostral part of the cortex to be larger than in the caudal part. With increasing size, neurons span larger horizontal distances as mentioned before, resulting in a wider local connectivity (Elston (2003)). Keeping in mind that despite low numbers of neurons per column, cortical thickness is increased in the rostral region due to larger neuron size, which also increases local connectivity width, the gyrification model can reproduce the difference in folding between the rostral and caudal parts of the brain as shown in Fig. 42. Changing only the number of neurons per column M , and therefore cortical thickness, results in the opposite effect as depicted in Fig. 42 A. The part with a decreased number of neurons per column (rostral part) is more convoluted than the other part, which is not what we find in biology. However, changing local connectivity according to the biological findings reveals that the connectivity parameters can compensate for the lack of neurons (Fig. 42 B). In the rostral part, neuron size and therefore the width of local connectivity, is increased. This is modelled by an increase in σ , which increases local connectivity width in the model. Despite the low number of neurons per column M compared to the caudal section, the degree of folding in the rostral part is now significantly lower.

In biology, it is oftentimes observed that regions which perform similar functions or are complementary are located in close vicinity and feature strong interconnectivity. Such regions that share a common functionality tend to form gyri (Welker (1990)). This structure therefore represents, for instance, a certain body part, or part of the auditory system with high connectivity (Scannell (1997)). In case two regions do not share a common function, they are likely to be separated by a sulcus. As stated by Welker (1990), some species even show a direct correlation between the number of nuclei in the thalamus and the number of gyri. Gyri could therefore be the manifestation of nuclei in a nervous system, but here, they form on the cortical sheet (as gyri). The gyrification model predicts something similar. Applying extreme sets of parameters in the model, neurons group into nuclei-like arrangements as shown in Fig. 15 B. When decreasing the number of neurons per column, the model predicts a phase transition towards a cortical sheet (Fig. 43). The nuclei arrangement resembles the organisation of neurons in birds (Jarvis et al. (2005)). Since a gyrus moves its walls closer together allowing for shorter connections, it may be a compromise that features the benefits of a nucleus as well an arrangement of neurons in a layered sheet. Such a compromise would be the result of strong lateral connectivity between columns and neurons that share a common function. In the gyrification model, effects on connectivity because of functional similarities between neurons are neglected.

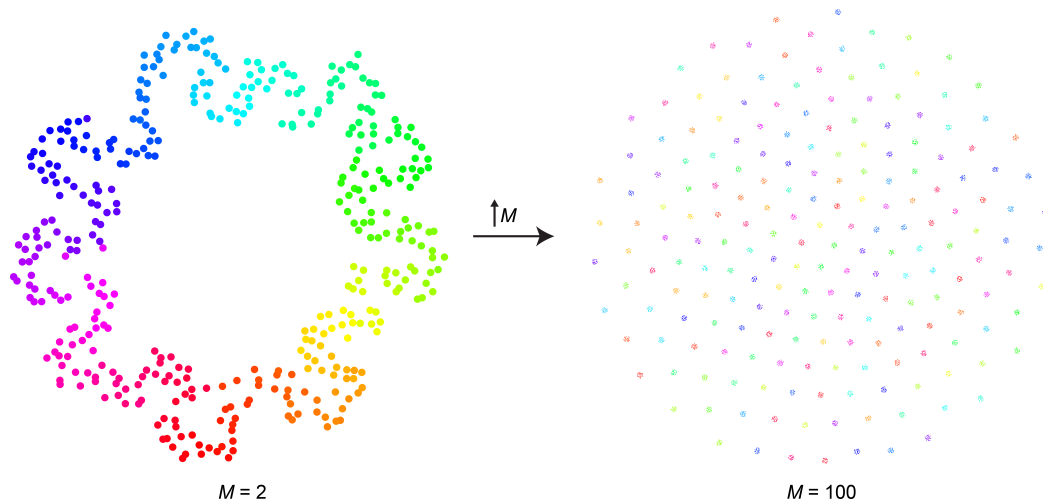


Figure 43. From cortical arrangement to nuclei

(Note: Figure by Groden et al. (2019), Fig. S6) A dramatic increase in the number of neurons per columns M leads to the transition from gyrification to nuclei ($C = 200$, $a = 0.1$, $b = 1$, $\sigma = 0.01$, $\gamma = 1$).

However, increasing connectivity in a small part of cortex can easily be done in the model. As depicted in Fig. 26, such a local increase in connectivity leads to the formation of a characteristic single fold. Unfortunately, the model predicts the formation of a sulcus rather than a gyrus. This is not surprising, since the model can not identify the benefits of bringing neurons closer together via a gyrus. On a local scale in the model, a sulcus is equally as optimal as a gyrus; however, on a global scale, the model favors the sulcus to reduce the distance to all other neurons, especially the ones that are topologically distant. In a real cortex, the gyrus would be far more beneficial to minimise wiring cost, since axons would be able to go right across rather than going all the way around like they would have to with a sulcus. There is no doubt that cortical folding depends on some physical force acting on the tissue pulling it together, thus creating gyri and sulci. Even though the gyrification model does not simulate any physical forces, it does not contradict their existence. Specifically forces that lead to wiring cost optimisation are compatible with the model. However, hypotheses like the axonal tension theory provide a more direct correlation between gyrification and wiring cost optimisation (Van Essen (1997)). Strongly interconnected parts of the cortex are consequently pulled together due to the force exerted by the axons connecting them forming a gyrus. The competing forces lead to neurons taking positions that optimise wiring cost. Analogously, the model predicts the positions of neurons based on how interconnected they are with highly connected ones in close vicinity, without the need to simulate physical forces. Predictions

by the model are therefore likely to represent self-organising global neural arrangements, created by forces pulling on single neurons. It is possible to explain gyrification of the cortex using such a self organising mechanism. If the position of a neuron depends on a mechanical pulling force exerted by its connections, then the magnitude of this force is going to change with the number of neurons. Given that the relative connectivity stays constant, this would lead to different folding layouts, explaining the phase transition from lissencephalic to highly convoluted folding patterns. This transition is predicted by the model and observed in biology, with the degree of folding depending predominantly on the number of columns (increasing cortical size increases the number of neurons) and not the specific connectivity (Weigand et al. (2017)). Furthermore, the model suggests that local connectivity and global connectivity result in different mechanical forces respectively that work together producing gyrification. The model was able to show that the formation of gyri depends on local connectivity (Fig. 23 A left), given that the balance between cortical size (number of columns) and the size of a column (neurons per column) is in the right range (Fig. 15 B). However, in the model, global connectivity is equally as important for the degree of folding of a folding pattern (Fig. 23 A middle and C). The physical tension of global connections tries to pull the entire structure together, making it more compact. The result would be a thick cortex, while local connectivity forces a small part of the cortex to contract. Local connectivity alone would therefore lead to a thin cortex.

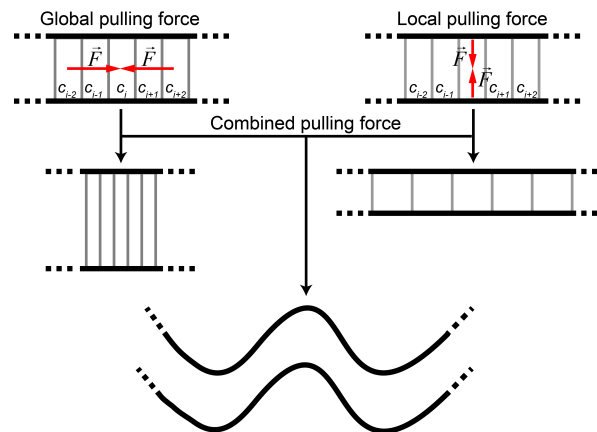


Figure 44. Local and global folding forces

(Note: Figure by Groden et al. (2019), Fig. S9) Presumably a combination of forces exerted by global and local connectivity leads to the formation of gyri and sulci. (Left) Global connectivity, in an attempt to save wiring length, exerts a pull in the tangential direction causing the cortex to thicken. (Right) Local connectivity which is dominant within cortical columns compresses the cortex. (Bottom) These two contradicting forces result in the formation of gyri and sulci signifying a compromise.

Combining the two counteracting forces, the only option for the cortex to fulfil both constraints is to fold, which represents a compromise (Fig. 44). Mechanical forces of significant magnitude have indeed been found (Bray (1984), Dennerll et al. (1989), Lamoureux et al. (1989), Chada et al. (1997), Heidemann et al. (1995), Xu et al. (2009), Xu et al. (2010), Hanein et al. (2011), Franze (2013)). Such forces were initially thought to be sufficient to drive the formation of gyri and sulci as proposed by Van Essen (1997). A more recent study by Xu et al. (2010), however, found that the tension exerted by axons is not strong enough to pull gyri walls together. As suggested by our model, forces that originate from local and global connectivity combine to define the folding pattern in the cortex. Analogously, a recent study by Lawton et al. (2019) showed that a differentially expanding outer layer under the influence of tensile radial forces and forces along the circumference determine the shape of the initial folding pattern of the cerebellum. The results of the model suggest that circumferential force within grey matter and forces pulling on the global structure through axon fibres in white matter are the reason behind gyrification in the biological cortex (Herculano-Houzel et al. (2010), Xu et al. (2010)). Additionally, Kroenke and Bayly (2018) found that the start of cortical folding in a growing brain coincides with the formation of connectivity. As soon as connections form, there are tensile forces along the axonal fibres. The formation of convolutions also corresponds to functional areas in the brain with characteristic folds usually forming in the same areas (Welker (1990)). Analysing these cytomolecular forces in the future would be interesting. Such investigations could be aided by the gyrification model, linking neuron's circuits to these mechanical forces.

6.2 Folding in pathological human brains

Disorders in the human brain can change the level of gyrification in parts or the entirety of the cortex. The result of such a change can, for instance, be lissencephaly in the human brain (Welker (1990), Di Donato et al. (2017)). A cortex described as lissencephalic features no or reduced gyri and increased thickness, since neurons fail to migrate to their proper positions within the cortex and remain stuck in white matter (Moon and Wynshaw-Boris (2013), Richman et al. (1975)). The absence of gyri and sulci is predicted to be the result of increased cortical thickness by mechanical models in a pathological lissencephalic condition (Budday et al. (2014), Richman et al. (1975), Toro and Burnod (2005)). In a thicker cortex, outer neuronal layers can be thinner compared to relatively thick inner layers.

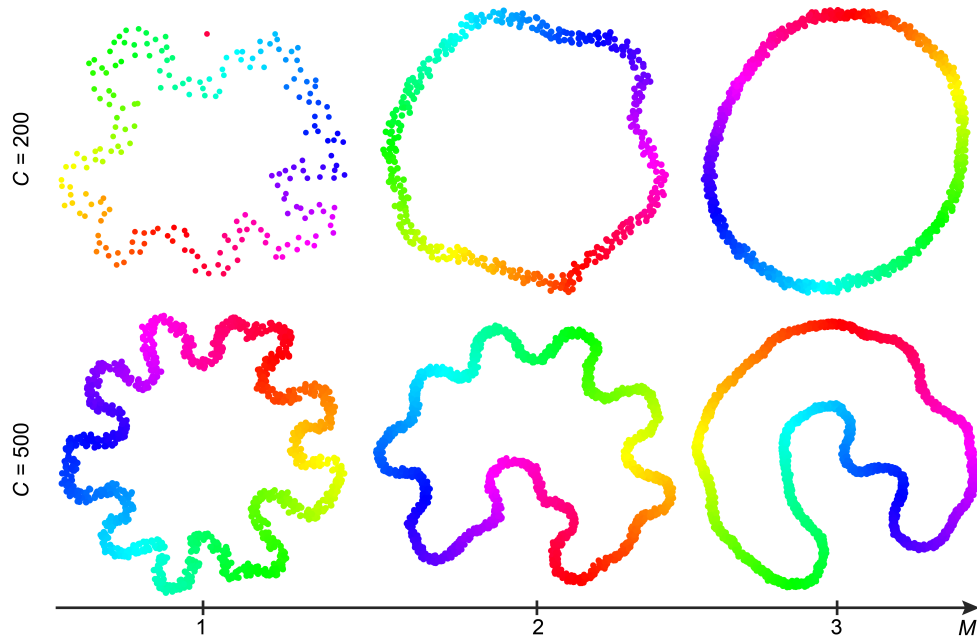


Figure 45. Increasing M leads to lissencephaly

(Note: Figure by Groden et al. (2019), Fig. S9) Increasing the number of neurons per column M leads to lissencephalic arrangements. For $C = 200$ the folding pattern reaches a state of no folding at all, while for $C = 500$ the transition is not completed entirely ($a = 0.2$, $b = 1$, $\sigma = 0.1$, $\gamma = 1$).

In line with these findings, the gyrification model described in this thesis predicts lissencephalic folding patterns for increasing numbers of neurons per column M (Fig. 45 top), which is the equivalent of increased cortical thickness in the model. Connectivity, however, plays a role equally as important, as changes here may result in lissencephaly as well. In lissencephalic cortices, the amount of white matter is reduced, which decreases the long-range connectivity, as shown by experiments conducted by Kao et al. (2011) and Lee et al. (2004). Similarly, a decreasing global connectivity leads to lissencephalic cortices (Fig. 23 C). Therefore, there might be a synergy of weak global connectivity and increased cortical thickness (larger numbers of neurons per column), that further reduces the prominence of gyri, leading to lissencephaly. Neither decreased global connectivity nor increased cortical thickness on their own are enough to produce completely lissencephalic folding patterns when the number of columns is increased (Fig. 45 bottom, Fig. 23 A and B).

Lissencephaly is just one example of a change in cortical folding that is caused by brain disorder. There are a wide variety of such pathological phenomena that change folding in different ways (Walsh (1999), Sun and Hevner (2014), Barkovich et al. (2012), Fernández et al. (2016)). By altering the corresponding parameters in accordance with how cytoarchitecture

changes within a pathological cortex, the gyrification model is capable of reproducing the same change in folding observed in biology as was demonstrated in Fig. 27.

6.3 Gyrification model relationships

Cortical connectivity is reportedly very strong on the local scale, but decays rapidly on a global scale, weakening long range connectivity (Kaiser et al. (2009), Ercsey-Ravasz et al. (2013), Hellwig (2000)). In the gyrification model presented in this thesis, only cortico-cortical connections are taken into consideration. This is done to make the model as simple as possible, since connections from subcortical regions do not contribute to folding in a significant way (Barron (1950), Welker (1990)). In the model, neurons are assigned to cortical columns, which are connected in a cyclical chain. The connection probability function, that defines which connections form between neurons, is based on the topological distance between the cortical column a neuron was assigned to. For reference, see Fig. 15 A and Fig. 22, which show the connection probability function in detail. Model results are able to reproduce folding patterns of varying degree of folding, ranging from arrangements with no folds to highly convoluted ones. Folding patterns exhibit multiple levels of gyrification with varying spatial frequencies of gyri and sulci. Changing the number of columns relative to the number of neurons per column and vice versa is enough to achieve such variety in the model (Fig. 15 B). The degrees of gyrification in mammalian species are covered by the model results, as the model produces folding patterns with folding comparable to large primates or even cetacean species, which exhibit the largest degree of folding (Fig. 16, Fig. 18 B, Fig.19, compare to findings by Mota and Herculano-Houzel (2015), Zilles et al. (1989), Welker (1990)).

Larger numbers of columns C in the model, corresponds to a cortical sheet of increasing size. This leads to an increase in the degree of folding, with large primary folds emerging first, and smaller folds of high frequency developing on top of the primary folds as secondary folds (Fig. 18 B, Fig. 19). The secondary folds exhibit a smaller amplitude. Opposed to that, the number of neurons per column M corresponds to cortical thickness, with low M signifying a thin, and large M signifying a thick cortex. In the model, folding increases with low M (thin cortices) and decreases with large M (thick cortices)(Fig. 45). These model predictions are in line with observations in mammalian species, where a thick cortex exhibits little folding, while cortices of larger size develop high degrees of gyrification (Welker (1990), Zilles et al. (1989), Hofman (1985), Mota and Herculano-Houzel (2015), Pillay and Manger (2007)).

There are a multitude of other models of gyrification that found the same influence cortical size and thickness have on the level of gyrification (Mota and Herculano-Houzel (2014), Tallinen et al. (2014), Budday et al. (2014), Bayly et al. (2013), Toro and Burnod (2005), Richman et al. (1975), Todd (1982), Prothero and Sundsten (1984)). The majority of these approaches focused on mechanical forces acting on the cortical sheet, that would cause it to fold. Therefore, they analysed what kind of strain the cortex experiences during growth and how it would react to such forces due to material properties and the properties of the white matter beneath, in an attempt to explain why gyrification emerges (Toro and Burnod (2005), Richman et al. (1975), Bayly et al. (2013), Budday et al. (2014)). Since they model mechanical forces, these models are well adapted to further our understanding of the underlying mechanism of cortical folding. The models, however, struggle to explain the development of stereotypical gyri and sulci. Specific folds are reproducible with the model presented in this thesis, when using the same connectivity, but introducing local changes of the connection probability function (Fig. 25 A and B). With respect to that, the model presented here is unique, since it takes connectivity into account, enabling the investigation of the effect of connectivity on gyrification. Variations in connectivity could hence be responsible for stereotypical folding patterns and explain why folding patterns can be inherited (Biondi et al. (1998), Bartley et al. (1997), Lohmann et al. (1999)). This approach could furthermore provide an explanation why folding patterns are characteristic within mammalian clades (Welker (1990)), why specific gyri and sulci can be identified as functional areas (Fischl et al. (2008), Welker (1990)), and why perturbations in connectivity change the appearance of folding patterns (Welker (1990), Rakic (1988)). Without any local changes of connectivity, the position of folds predicted by the model is random, even when using the same connectivity for two separate folding patterns (Fig. 24). The degree of gyrification, however, remains much the same. In mammalian species with high levels of gyrification, characteristic as well as unpredictable folds have been observed. The degree of gyrification in such mammalian species remains similar among individuals belonging to the same species, despite the fact that the exact position of a fold is unpredictable (Zilles et al. (2013)), which is in agreement with the model predictions. Therefore, it is likely that characteristic convolutions in the brain are the result of functional areas of the cortex that are highly interconnected and feature a highly organised connectivity. Unpredictable convolutions probably emerge due to variations in cortical sheet size, the number of neurons per column or connectivity.

The gyrification model presented in this thesis is very practical when it comes to understanding

the link between cortical folding and connectivity, as was demonstrated for multiple examples from biology. The model is, however, based on assumptions, which greatly simplify the model, but work on an abstract level (O'Leary et al. (2015)). The numbers of neurons used in the model are far below what is observed in mammalian species. The sheer computational power to handle such numbers is simply not available. The model assumes that the relative position of neurons is decided by how the neurons are connected. This is done by using a dimension reduction method that determines a neurons position based on its connection dissimilarities. Since in such arrangements, neurons that share a lot of connections are placed spatially close, they instinctively satisfy optimal wiring constraints (Chklovskii and Koulakov (2004), Laughlin and Sejnowski (2003), Ruppin et al. (1993), Wang and Clandinin (2016)). Costa et al. (2007) and Song et al. (2014) actually found that connection dissimilarities correspond to the relative connectivity between functional areas. This relative connectivity in turn is associated with the distance between such areas in the cortex (Ercsey-Ravasz et al. (2013)). The model assumes that this relationship between connection dissimilarity and distance can be carried over and applied to neurons as well. It has already been shown that a dimension reduction method, namely oMDS (ordinal multidimensional scaling), is capable of predicting cortical maps in mammalian visual cortices (Weigand et al. (2017)). Here, connectivity is determined by feature preferences of neurons. Instead of using oMDS, the gyrification model uses t-SNE (van der Maaten and Hinton (2008)), since it performs much better. t-SNE specialises on preserving data structure locally and globally on the projection of low dimensions, as well as set apart data that lies on multiple high dimensional manifolds (van der Maaten and Hinton (2008)). Studying the effect of connectivity on the folding pattern arrangement on different scales, meaning global and local connections, is made possible by these distinct properties of t-SNE. oMDS as a more conservative approach falls short in these regards. Importantly, t-SNE next to its advantages does have some unwanted flaws or side effects (Wattenberg et al. (2016)), occasionally resulting in solutions exhibiting some form of degeneracy (Fig. 17). Evidently, the cost function minimised by t-SNE has no relation to a growing cortex, where cells migrate to the cortical layers, like we observe in biology (see Materials and methods **Chapter 4**). Also, for the dimension reduction method there is no reason why neurons in folding patterns can not form a sheet rather than a circular line. This leads to the formation of degenerate arrangements. The degree of folding was easy to recognise in the degenerate folding patterns, matching the level of gyrification in regular ones within the same parameter range. All degenerate solutions were, however, discarded using an automatised algorithm

that filtered out all results that did not form a closed loop (see Materials and methods **Chapter 4**). Since computational power limits the number of neurons used in the model, as mentioned earlier, the model is not capable of explaining how connectivity and the number of neurons relate quantitatively. However, in spite of such simplifications, the qualitative predictions of the model are widely in line with experimental data, as shown before. Taking into account what has been found by Weigand et al. (2017) regarding cortical maps in addition to matching cortical folding and connectivity, the gyrification model suggests that the nervous system is moulded by optimising wiring constraints.

The potential of the gyrification model is far greater than what has been elaborated on in this thesis. Using relatively low numbers of neurons and corresponding connectivity parameters, it was possible to compute large sets of data that include a lot of different levels of gyrification, showing a large proportion of the folding pattern spectrum. Creating folding patterns with much larger numbers of neurons is, however, theoretically possible (Fig. 16). Such folding layouts potentially feature extreme degrees of gyrification. Changing the connectivity matrix in very specialised ways reveals what the model is capable of. This is demonstrated in Fig. 46 A right, where a folding pattern with two distinct hemispheres was created using a special connectivity matrix. Two topological rings of columns feature the same connectivity used in the model, with sparse global but strong local connectivity, within themselves respectively. This is indicated by the connectivity matrix depicted in Fig. 46 A left, with the upper left section of the matrix corresponding to one hemisphere and the lower right section to the other. The interconnectivity in between the two hemispheres is very sparse and corresponds to the lower left and the upper right section of the matrix. Fig. 46 B right demonstrates another special connectivity folding pattern that mimics the rough shape of the hippocampal region. The layout of the connectivity matrix in Fig. 46 B left is the same as in Fig. 46 A left. In this particular case, random noise connections were added to the connectivity, as depicted in the connectivity matrix. In the future, the model could be used to uncover the anatomical aspects of homologous structures in the brain. For this purpose, a lot of details of cortical connectivity would have to be added, forming special models that help explain the distinct folding arrangement of the mammalian hippocampus and the comparatively simple corresponding homologous regions in reptiles (Tosches et al. (2018)).

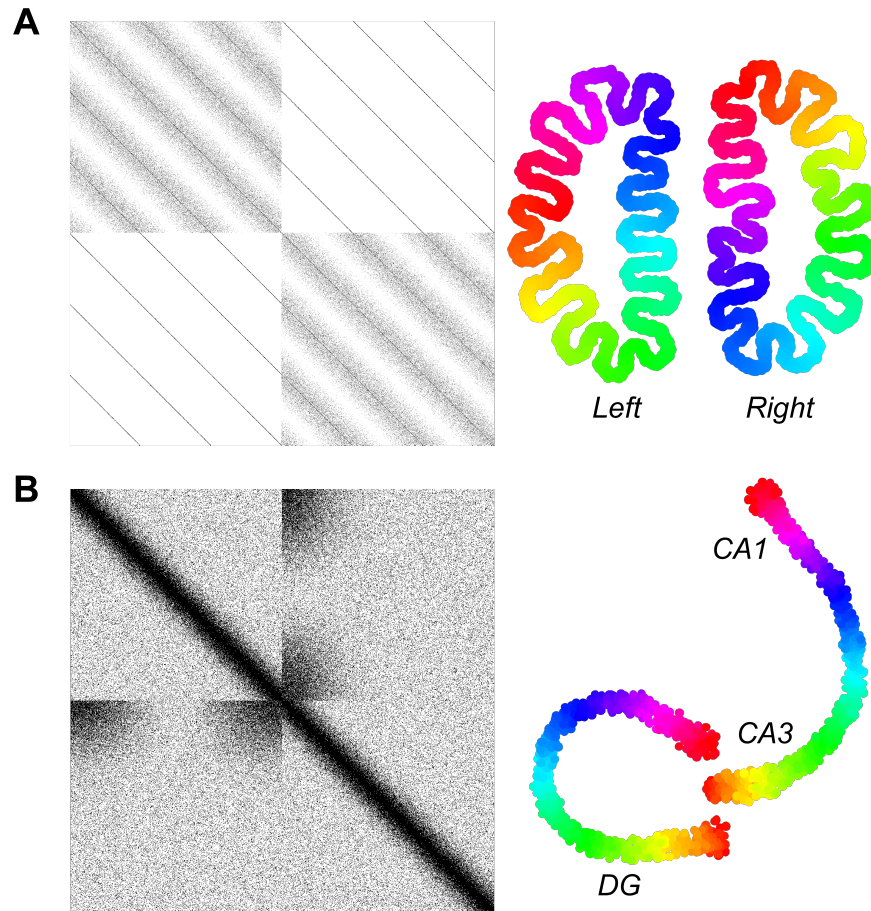


Figure 46. Modelling specific anatomical structures

(Note: Figure by Groden et al. (2019), Fig. S8) **A**, Binary connection matrix on the left with every black dot signifying a connection. The two folding pattern hemispheres on the right feature the same intra-connectivity as usual (top left and bottom right in the matrix). Every column is also connected to its counterpart of the folding pattern in the other hemisphere. The connection probability rapidly decays the further columns are separated topologically (bottom left and top right in the matrix). **B**, Binary connection matrix on the left like in **A**. The two chains are non-cyclical, with one chain being strongly connected to both ends of the other chain (bottom left and top right in the matrix). The chains feature a similar connectivity within themselves. The connectivity represents a rough, simplified version of the connectivity in the hippocampus, with the dentate gyrus (DG), the CA1, and CA3 region.

6.4 The lissencephalic manatee

It is unlikely the presumed connectivity differences between mammals and rodents are mainly responsible for the often lissencephalic appearance of rodent cortices. Recent studies suggest that the low degree of folding in rodents is due to the small size of their cortical

sheet (Mota and Herculano-Houzel (2015)), which is in agreement with the findings of the gyrification model presented in this thesis. Interestingly, there is an outstanding exception that debunks the theory that lissencephalic cortices are only observed in species with a small cortical sheet, which is the manatee. The manatee's cortical size and number of neurons is in the range of primates, yet its cortex is lissencephalic (Charvet et al. (2016)). Considering that marine mammals and species of the Afrotherian clade that are closely related (Foote et al. (2015)) display extreme levels of gyrification (Zilles et al. (2013), Mota and Herculano-Houzel (2015), Pillay and Manger (2007)), this seems even more peculiar. According to the gyrification model, there is a peak level of folding when increasing the number of columns and therefore increasing cortical size, after which folding decreases back towards lissencephalic arrangements (Fig. 20). These lissencephalic folding patterns feature a thicker cortex that still shows some larger primary convolutions. In the model it seems as if the small high frequency secondary folds fuse together creating a thicker cortex. The same could be happening in the manatee leading to its lissencephalic cortex. Approaching from a different angle, in the model low degrees of folding can correspond to a large number of neurons per column (Fig. 45, Fig. 43). Alternatively, strong local connectivity in addition to weak global connectivity by itself or in conjunction with large numbers of neurons per column would yield the same model results (Fig. 23 A, B and C) and could explain how neurons cluster into *Rindenkerne* (Butti et al. (2011)).

6.5 Benefits of a neuron dendritic repair tool

Most of the insight into the detailed functionality of structures in the brain has been derived from experimental research conducted in animals. The research is mostly based on animal data, since reliable, accurate data on the human brain and neurons is sparse (DeFelipe (2015)). In June of the year 2021, the data on human nerve cells contained by *neuromorpho.org* (Ascoli et al. (2007), Parekh and Ascoli (2013)), which is one of the largest public data bases on neuron morphologies, amounts to only approximately 4.9% of the entire data set. Adding to the already limited data situation is the fact that acquiring large data sets of neurons from human brain tissue is restricted by ethical issues (Kellmeyer (2021), Tilimbe (2019), Palk et al. (2020)). It is, however, of critical importance to be able to study human neurons specifically instead of those of animals. This is due to observations that found functional and structural differences between neurons of humans and other mammals (Geschwind and Rakic (2013), Hofman

(2014), Rilling (2014), Kaas (2013), Sherwood et al. (2012), DeFelipe (2011), Oberheim et al. (2009), Schmidt and Polleux (2022)), which is the reason why substituting human with other mammalian data is not viable (Zhao and Bhattacharyya (2018)). There are a multitude of reported differences between for example, homologous mouse and human neurons involving gene expression, morphology and laminar distribution (Hodge et al. (2019)). Eyal et al. (2016) found human layer 2/3 pyramidal neurons from the temporal cortex to have a lower membrane capacitance $C_m \approx 0.5\mu F/cm^2$, compared to the agreed upon $C_m \approx 1\mu F/cm^2$ found in other species. The study predicts the lower membrane capacitance improves synaptic charge-transfer from the dendrites to the soma and spike propagation along the axon in human neurons by using 3D reconstruction models. The human brain's size increased during evolution as well as its complexity (DeFelipe (2011)). Therefore, specialised mechanisms developed in human neurons to handle the increased complexity of higher brain functions, including strong excitatory synapses allowing excitatory principal cells to cause local inhibitory neurons to fire through only a single action potential (Szegedi et al. (2016)). Firing patterns of large groups of neurons that represent the higher functions of the brain could otherwise not be coordinated. From a morphological standpoint, synaptic spines have been reported to be significantly larger, longer and come in higher densities in human neurons compared to mice (Benavides-Piccione et al. (2002)). Also human CA1 pyramidal neurons have been found to be larger and structurally different from mouse CA1 pyramidal neurons (Benavides-Piccione et al. (2020)). Understanding these differences between human neurons and those of other species will be key to unravel what makes the human brain so unique in terms of cognitive abilities. On top of the problematic human neuron data situation, most of the 3D morphology reconstructions originating from human cells that are available, are taken from pathological neurons extracted from patients with brain disorders that can potentially change the morphology and functional aspects of the neurons (Houser (1992), Glass and Dragunow (1995)). The reconstruction process after obtaining the neurons from patients is a difficult procedure that is unfortunately prone to error itself (De Schutter and Jaeger (2000)). By resecting tissue, dendrites of neurons can be accidentally cut, or agents injected into the neuron to stain it for microscopy may not reach remote areas of the dendrite and the resulting microscope image can be distorted, to mention just a few possible errors.

To tackle the issue of studying human morphologies for their specific structural and functional aspects, the scientific community needs to have access to large, complete and reliable data sets of 3D reconstructions of human neurons. The neuron dendrite repair tool introduced in

this thesis is designed to improve the data situation on specifically human neurons, as well as solve and relief problems and difficulties associated with neuron reconstruction. Data sets that already exist and contain incomplete reconstructions can be improved by completing these morphologies. This will enlarge data sets of human neurons, counteracting the problematic ethical situation that limits the ways data of human neurons can be acquired. Data that would otherwise be invalid due to pathological damage to neurons and brain disorders can be repaired such that these neurons resemble their healthy state more closely. These repairs can then be added to the existing data bases.

6.6 Recovering human CA1 pyramidal neuron morphology and electrophysiology

By extending the dendrites of human CA1 pyramidal neurons using the neuron repair tool (see Fig. 33 and 34), the apical arbor reaches more than halfway into the SLM layer, making the formation of synaptic input connections arriving from the perforant path that would normally form (Ito and Schuman (2012)) possible. None of the human reference morphology reconstructions in Fig. 33 feature an apical tuft. Since the tuft is located far away from the soma it is hard to reconstruct. However, the projections reaching the CA1 region of the hippocampus from the entorhinal cortex contact the apical tuft regions of CA1 pyramidal neurons as well as interneurons in the SLM layer as shown for rats (Capogna (2011), Desmond et al. (1994)). Therefore attaching an artificial tuft to a human CA1 pyramidal neuron reconstruction can help recover their original functionality, providing better insight into the properties of human neurons. The same concept can be applied to other cells in different regions. Unfortunately, it is impossible to know exactly what incomplete dendrites would look like in real life. The areas where the new artificial dendrite extensions would grow (Fig. 34 C) were designed in accordance with the expertise and experience of Benavides-Piccione et al. (2020). Examples of the growth volumes provided by Benavides-Piccione et al. (2020) are attached in the Appendix (**Chapter 11**) Fig. S1. The placement of the growth volumes was done taking regions of arriving synaptic input into account. Furthermore, dendritic material lost due to tissue lesion was recovered, which was mainly the case for the basal arbors.

Repairs executed with the neuron tool are able to recover the firing behaviour of the original reference morphology, as demonstrated in Fig. 35. While the damaged morphology exhibits

a significantly increased firing rate when stimulated somatically compared to the reference, the repair behaves like the reference. These differences in firing behaviour are to be expected, since alterations in morphology reportedly have a big impact on neuron firing response (Zhu et al. (2016)). The firing rate of the repaired morphology does not match the reference perfectly, with the repair showing a slightly reduced firing rate. This can be due to differences in topology between the repaired morphology and the reference. While the morphology of the repair closely resembles the appearance of the reference, they are not an exact match. Such small structural differences in geometry and complexity have been shown to affect a neuron's firing behaviour (Mainen and Sejnowski (1996), Zhu et al. (2016), van Ooyen et al. (2002)). Compared to the cut neuron, the repaired morphologies' firing rate has improved significantly, fixing what would otherwise potentially be a neuron behaving in a pathological fashion. The neuron repair tool can therefore help recover the true functionality and behaviour of neurons, specifically human neurons.

The repair of both human and mouse neurons influences their electrophysiological behaviour in a similar way. The cut morphologies exhibit an increased firing rate as shown in Fig. 35, yet the effect is not identical. As mentioned before in **Chapter 5**, analysing the electrophysiological differences between the human and mouse CA1 pyramidal neurons provided by Benavides-Piccione et al. (2020), that were repaired with the neuron repair tool, has not been possible, due to a lack of data. The analysis of the electrophysiological differences between human and mouse dentate gyrus granule cells in Fig. 37 (data provided by Buchin et al. (2020)) that was performed instead, showed that there are indeed significant differences between the two species. These differences are also linked to the morphological differences displayed in Fig. 39. Compared to the input resistance of mouse granule cells (GCs) reported by Schmidt-Hieber et al. (2007) ($R_{in} = 308 \pm 26 M\Omega$) and Beining et al. (2017) ($R_{in} = 289.5 \pm 34.9 M\Omega$), the value for human cells ($R_{in} = 109 \pm 10.63 M\Omega$) was significantly lower. Reported values for human dentate GCs include a wide range of values. Stegen et al. (2012) find R_{in} to be very high ($394.8 \pm 60.2 M\Omega$) in human GCs with mild hippocampal sclerosis (HS) and reduced in case of severe HS ($155.5 \pm 41.4 M\Omega$). In another study by Stegen et al. (2009), values for R_{in} range from $290 \pm 41 M\Omega$ for cells of Wyler grade 2 to $192 \pm 16 M\Omega$ for Wyler grade 3 (the Wyler grade (WG) indicates the level of HS (Wyler et al. (1992))). The human GCs provided by Buchin et al. (2020) seem to follow a different trend, as WG1 (mild HS) shows lower R_{in} than WG3/WG4 (severe HS) (Fig. 38). Stegen et al. (2012) state that the low values of input resistance for severe HS are likely due to an increase in membrane conductivity rather than a change in cell size,

as the membrane surface area was similar for mild and severe HS. This is in line with the results in Fig. 39, since the total dendritic length and the mean dendritic diameter does not change with different WG. Therefore, the surface area does not change either. The values for R_{in} reported by Stegen et al. (2009) and Stegen et al. (2012) seem to be more in the range of mouse cells when compared to Schmidt-Hieber et al. (2007), Beining et al. (2017) and Young et al. (2009) ($421 \pm 12M\Omega$). This is, however, strange, since human GCs tend to be larger than mouse GCs, as demonstrated in Fig. 39, and should therefore have lower R_{in} . The concept applies to other cell types as well, as shown by Beaulieu-Laroche et al. (2021) who compare the properties of layer 5 pyramidal neurons across different species, with the large human neurons exhibiting one of the lowest values for R_{in} . Similar to R_{in} , the membrane time constant T_m in human GCs ($13.11 \pm 1.33ms$) is reduced when compared to the mouse ($34 \pm 2ms$ Beining et al. (2017), $37.2 \pm 2.6ms$ Schmidt-Hieber et al. (2007)). Again T_m for human GCs (mild HS: $43.2 \pm 2.1ms$; severe HS: $28.4 \pm 1.2ms$) as found by Stegen et al. (2012) resembles the mouse. The difference in T_m between WGs is also reversed in Fig. 38 compared to Stegen et al. (2012). According to the results in this thesis and the literature, there seems to be a large variation in R_{in} and T_m due to pathological changes within human GCs caused by HS.

The Membrane resting potential V_{rest} for human GCs ($-90.9 \pm 2.93mV$) was in a similar range compared to mice ($-80.4 \pm 1.3mV$ (Schmidt-Hieber et al. (2007)), $-92.7 \pm 0.5mV$ (Beining et al. (2017))). V_{rest} does not seem to be significantly affected by HS in human GCs as well, as displayed in Fig. 38 and found by Stegen et al. (2012) (mild HS $-73.1 \pm 1.0mV$, severe HS $-78.9 \pm 0.9mV$) and Stegen et al. (2009) (WG2: $-73.2 \pm 1.1mV$, WG3: $-75.1 \pm 1.1mV$). The calculated mean values for the axial resistance R_a in Fig. 37 are slightly increased in humans ($225.04 \pm 88.28\Omega cm$) compared to mice ($194 \pm 24\Omega cm$ Schmidt-Hieber et al. (2007)), but feature a large range of possible values. Even with artificially added spines R_a does not change a lot (artificial spines: $226.81 \pm 87.87\Omega cm$). This is due to the wide range of possible values for R_a that produce a fitting value for R_{in} , even for different WGs (Fig. 38). Therefore, R_{in} seems to be mostly dependent on the value for G_m . Reported values for R_a range from $142.03\Omega cm$ in mild HS to $212.56\Omega cm$ in severe HS (Stegen et al. (2012)), indicating large fluctuations. In Fig. 37 the variations in the membrane conductance G_m are significant, compared to R_a . Adding artificial spines increases R_m overall, which in turn decreases G_m . Thus the human GC reconstructions exhibit a high value for G_m ($1.17 \cdot 10^{-4} \pm 2.17 \cdot 10^{-5}S/cm^2$), where as with added spines ($0.94 \cdot 10^{-4} \pm 1.49 \cdot 10^{-5}S/cm^2$), G_m decreases. Since with added spines the surface area of the neuron increases by a factor of ≈ 1.465 , G_m here is not as low as it

would be with spine control factor of ≈ 2 as suggested by Schmidt-Hieber et al. (2007). G_m in case of the mouse ($2.63 \cdot 10^{-5} \pm 0.16 \cdot 10^{-5} S/cm^2$ Schmidt-Hieber et al. (2007)) is much lower. This is likely due to the large values of T_m in mice compared to humans, to compensate and achieve a membrane capacitance of $\approx 1 \mu F/cm^2$ ($C_m = T_m/G_m$). C_m is largely agreed upon to be a natural constant (Curtis and Cole (1938)). The results by Schmidt-Hieber et al. (2007) support this hypothesis, however, there have been recent studies suggesting a lower C_m of $\approx 0.5 \mu F/cm^2$ in human layer 2/3 pyramidal neurons (Eyal et al. (2016)) or $\approx 0.9 \mu F/cm^2$ in rat layer 5 neurons (Gentet et al. (2000)). In Stegen et al. (2012), C_m is fixed at $1 \mu F/cm^2$. Their reported values in human GCs for R_m (mild HS $42.36 k\Omega cm^2$; severe HS $14.79 k\Omega cm^2$), as $R_m = 1/G_m$, are within the range of those found in this thesis ($9.76 \pm 1.82 k\Omega cm^2$; added spines $11.97 \pm 1.84 k\Omega cm^2$). The difference in R_m and G_m between different WGs in Fig. 38 is, however, the opposite of that reported by Stegen et al. (2012). However, the difference between WG1 and WG3/WG4 in Fig. 38 ensures that $C_m \approx 1 \mu F/cm^2$. This is true in Fig. 37 as well, since with proper compensation for the lack of spines, both human (added spines $1.15 \pm 0.18 \mu F/cm^2$) and mouse ($1.01 \pm 0.03 \mu F/cm^2$ by Schmidt-Hieber et al. (2007)) neurons feature $C_m \approx 1 \mu F/cm^2$. Without any compensation for spines C_m in human GCs is too high $1.44 \pm 0.24 \mu F/cm^2$. Therefore, the findings in this thesis suggest that the hypothesis of a constant $C_m \approx 1 \mu F/cm^2$ holds true.

The morphological differences between human and mouse neurons in Fig. 39 suggest that human neurons are larger and more complex than those of mice. This is in line with studies that found similar results when comparing human morphologies to those of other species like macaque monkeys, marmosets and chimpanzees (Elston et al. (2001), Bianchi et al. (2013), Schmidt and Polleux (2022)). Human neurons are both larger and more complex in all cases. Interestingly, the ratio of the difference in total dendritic length between mouse and human neurons in both GCs and CA1 pyramidal neurons seems to be similar in Fig. 39. This suggest that the size scaling factor between the two species is similar across different cell types. Pathological conditions like HS seem to cause a large variation in electrophysiological properties in human GCs. The neurons seem to undergo changes in passive properties, presumably to maintain a consistent input output relationship, as neurons of different WG still maintained a membrane capacitance of $\approx 1 \mu F/cm^2$. The analysis of the passive electrophysiological properties of both mice and human neurons further underlines the importance of being able to repair especially incomplete human morphologies. The differences in electrophysiology between the two species illustrate how human neurons compensate for differences in their

morphology. Supplying complete human morphology data sets will help unravel whether these changes are just for compensation or actually change the way human neurons process information.

6.7 Neuron dendrite regeneration

Class IV da neurons in *Drosophila* are studied for their ability to regenerate dendrites (Song et al. (2012)). In the peripheral nervous system (PNS) regeneration of class IV dendrites is common, as Song et al. (2012) found regrowth to originate from the lesioned stem in 49.4% of the cases, which was also reported by Stone et al. (2014) but not quantified. In case the dendrite did not regrow from the sectioned stem, branches from the neighbouring dendrites invaded the vacant region, covering the epithelial area with the dendritic network. Song et al. (2012) reported this bimodal regrowth behaviour. In almost 100% of the cases, the vacant region was recovered by the neuron dendrites in one way or the other (Stone et al. (2014)).

Since the process of regeneration is very complex when considering cell type, stage in development and specific mechanisms, covering all these factors with the neuron repair tool has not yet been possible. It is, however, possible to reproduce the resulting bimodal distribution of dendrite regrowth, using the comparatively simple approach of the TREES toolbox. Focusing more on the method used by Song et al. (2012) to calculate invasion would be worthwhile at this point. Song et al. (2012) found that for cases with 100% invasion, the lesioned dendrite would stall or retract. In such a case it is, however, unclear whether the branch is still operational or not. In case of a retraction, new target points could be connected to the branch, which was not considered by Song et al. (2012). Leaving a longer stump when cutting the dendrite caused regeneration to sprout from that location more often (Stone et al. (2014)). With regard to this finding, investigating what impact the site of dendriotomy has on invasion occurring as opposed to regeneration should be of interest.

Although the neuron repair algorithm can not mimic biological regrowth completely, the results presented in this thesis allow for more insight and more secure use of the TREES toolbox. Since the repair algorithm was able to reproduce the bimodal distribution between invasion and regeneration, the results show that the same algorithm using the balancing factor bf can be implemented to regenerate dendrites mimicking biological regrowth and to repair an incomplete neuron. Additionally, the model shows that dendrites have similar properties before the lesion event and after the regrowth regardless of whether neighbouring dendrites

invade or the lesioned stem regrows.

6.8 Pros and cons of the neuron repair tool

Distributing carrier points in a specifically chosen volume is the underlying approach the neuron repair tool is based on. The algorithm successively connects these carrier points to the existing morphology reconstruction, using optimal wiring constraints. The volume within which the carrier points are distributed can be based on the convex hull of sectioned dendrites, or chosen by the user arbitrarily. This method provides high flexibility, enabling the user to specify exactly where the morphology should be extended. On the flip side, it presupposes a certain level of intuition and experience of the user. The addition of a background image of sufficient quality, which can be used as a reference, negates some of this problem. Specifically users/morphology re-constructors with experience in the field will be able to judge the dimensions and boundaries of a morphology as well as where parts might be missing much more effectively when using a background image. In case of the CA1 region of the hippocampus and other brain regions with a similar organisation into different layers, the procedure is greatly facilitated, since layer boundaries clearly indicate where dendrites and somata are located. Other regions, like the cortex, are likely to pose a bigger challenge, since here, neurons do not grow within well defined layers but anywhere within a cortical column (Tischbirek et al. (2019)). To eliminate the problem of an arbitrarily chosen growth volume, the final complete boundary of any neuron would have to be predicted by an algorithm that implements a large data base of neuron morphology reconstructions. Such an algorithm would have to analyse the existing input morphology (just like the neuron repair tool introduced in this thesis) and consider its specific cell type, region of origin in the brain and species. The data base the algorithm relies on has to contain a large number of complete neuron reconstructions from different species, cell types and brain regions. Based on the specifications of the input morphology, the most probable complete boundary of the input neuron is then predicted by averaging over the spanning volumes of all neurons from the data base that fit those requirements. The average is then scaled to fit the size and dimensions of the input neuron so its missing parts can be completed by the repair algorithm. Implementing this data base based approach could be the subject of future research.

Input morphologies with increasingly larger sectioned parts of their dendritic arbor make it more and more difficult to reliably analyse the properties of what is left of the neuron.

Deriving repair parameters off of a highly damaged morphology therefore is likely to be flawed. The level of uncertainty in a morphology repair consequently increases in case the input morphology features only minimal reconstructed dendritic material.

Studying how neurons react to damage or injury *in vivo*, and how these sectioned dendrites regrow afterwards, has been the subject of recent research (Song et al. (2012), Li et al. (2018), Stone et al. (2014)). Repairing these morphologies by replacing the missing dendritic material with artificial ones has not been attempted. Hence, the approach of the neuron repair tool described in this thesis is unique, as it is a simple general method, applicable to any cell type or species. As the tool is available as an easy to use graphical-user-interface, anyone can repair sectioned dendrites of morphologies that would otherwise be unusable for research. The growth process in most morphological computer models is implemented as a stochastic procedure, depending on branching probability, how many branching events occur, and the number of segments etc. (van Pelt and Schierwagen (2004), Ascoli and Krichmar (2000), Donohue and Ascoli (2008)). As the repair tool is build upon the TREES toolbox, wiring optimisation is taken into account. Different cell types can therefore be modelled using a single parameter (the balancing factor bf), since different cell types fulfill different optimal wiring constraints. According to Poirazi and Papoutsi (2020), the parameter set used to implement a model should be as small as possible. Such an approach, like the neuron repair tool introduced in this thesis, provides the needed simplicity and adaptability to seamlessly be implemented into daily research.

6.9 Conclusion

Both the macroscopic and the microscopic structure of the brain follow the constraint of wiring optimisation. This fact is demonstrated by the two computer simulations described in this thesis. While the intricate folding patterns of the cortical sheet can be modelled by a specific connectivity function that ensures weak global but strong local connectivity and minimising wiring cost, dendrites of damaged neurons can be repaired using a similar principle. The repair of these dendrites depends on a compromise between minimising wiring cost and conduction time to the soma. Therefore, wiring optimisation is essentially a compromise in both cases that holds a delicate balance between network performance and wiring cost.

Cortical folding can be predicted by using a dimension reduction method (here t-SNE) that finds the optimal positions for neurons in terms of wiring optimisation. In order for this

approach to work, the model assumes strong local but weak global cortical connectivity. The predictions made by the gyrification model are consistent with experimental findings, reproducing cortical gyrification patterns in a large range and relations between common measures. The model can be used to investigate the emergence of characteristic folding patterns, how folding scales, and give insights into pathological brain disorders, revealing the underlying connectivity and circuitry. By adding more detail to the model, the approach can in the future give rise to models that explore the anatomy of neural circuits more precisely. Damaged dendritic arbors of different neuron types can be repaired artificially using in silico computer models like the neuron repair tool described in this thesis. This is relevant, since the reconstruction process of neuron morphologies is a difficult procedure that is prone to error. Especially in case of human morphologies, where availability of reliable complete reconstruction data is very limited, repairing morphologies artificially could improve the situation significantly, enabling more research of human cells. Investigation of human neurons is of critical importance, since more and more reports emerge that state how properties of human neurons are different from other species. Additionally, the neuron repair tool can mimic biological regrowth of neurons, reproducing the findings of biological experiments.

7 Publications

The research presented in this monographic doctoral thesis has been conducted with the intent of publication in the form of scientific journal papers. The publications are listed in the following section.

Publication 1

A model of brain folding based on strong local and weak long-range connectivity requirements

Status: *published*

Journal

Cerebral Cortex

Publication 2

A biologically inspired dendritic repair mechanism for reconstructions of human and nonhuman neurons

Status: *Submission*

8 Acknowledgements

I am very grateful for the support and guidance of Prof. Dr. Peter Jedlička and Dr. Hermann Cuntz, who have both supervised me since the early stages of my master thesis. Their far sight and expertise has provided invaluable input that made the research projects presented in this thesis what they are.

Great gratitude also goes to Prof. Dr. Christian Heiliger who without hesitation agreed to supervise my Ph.D. thesis.

On the first project regarding the macroscopic model of gyrification of the cortex, Dr. Marvin Weigand proved to be an invaluable partner and collaborator. Without his expertise in the field of coding and guidance, many features of the model would not have been explored to the extend shown in this thesis.

Dr. Ruth Benavides-Piccione and Dr. Javier DeFelipe kindly provided the data sets of mouse and human CA1 pyramidal cells. Furthermore they also provided their much needed expertise on morphology reconstructions and the practical procedure used to obtain them. Without their knowledge of where and how dendritic material is usually lost in the reconstruction process, repairing and extending human morphologies would not have been possible. The inspiration for the neuron repair tool came from research that was previously conducted on Class IV Drosophila neurons by Hannah Moessinger and Barbara Schaffran. Many thanks also go to Anatoly Buchin for providing the data on human dentate granule cells.

My final thanks go to the people surrounding me in my everyday life. Writing a doctoral thesis without any emotional support can be tough. Therefore I very much appreciate the support of especially my parents who have been doing this the longest and my girlfriend who had to deal with it every day. I also appreciate the support of everyone else who might have contributed unknowingly with a nice word or an inspiring scientific conversation.

9 Declaration

I declare that I have completed this dissertation single-handedly without the unauthorized help of a second party and only with the assistance acknowledged therein. I have appropriately acknowledged and cited all text passages that are derived verbatim from or are based on the content of published work of others, and all information relating to verbal communications. I consent to the use of an anti-plagiarism software to check my thesis. I have abided by the principles of good scientific conduct laid down in the charter of the Justus Liebig University Giessen "Satzung der Justus-Liebig-Universität Gießen zur Sicherung guter wissenschaftlicher Praxis" in carrying out the investigations described in the dissertation.

Giessen, 11.11.2022

10 References

- Akkiraju N, Edelsbrunner H, Facello M, Fu P, Mucke E, Varela C (1995) Alpha shapes: definition and software. *Proceedings of the 1st International Computational Geometry Software-Workshop* p. 66.
- Alderson-Day B, McCarthy-Jones S, Fernyhough C (2015) Hearing voices in the resting brain: A review of intrinsic functional connectivity research on auditory verbal hallucinations. *Neurosci Biobehav Rev* 55:78–87.
- Amunts K, Zilles K (2015) Architectonic Mapping of the Human Brain beyond Brodmann. *Neuron* 88:1086–1107.
- Ascoli GA, Donohue DE, Halavi M (2007) NeuroMorpho.Org: a central resource for neuronal morphologies. *J Neurosci* 27:9247–9251.
- Ascoli GA, Krichmar JL (2000) L-neuron: A modeling tool for the efficient generation and parsimonious description of dendritic morphology. *Neurocomputing* 32-33:1003–1011.
- Barkovich AJ, Guerrini R, Kuzniecky RI, Jackson GD, Dobyns WB (2012) A developmental and genetic classification for malformations of cortical development: update 2012. *Brain* 135:1348–1369.
- Barron DH (1950) An experimental analysis of some factors involved in the development of the fissure pattern of the cerebral cortex. *Journal of Experimental Zoology* 113:553–581.
- Bartley AJ, Jones DW, Weinberger DR (1997) Genetic variability of human brain size and cortical gyral patterns. *Brain* 120 (Pt 2):257–269.
- Bayly PV, Okamoto RJ, Xu G, Shi Y, Taber LA (2013) A cortical folding model incorporating stress-dependent growth explains gyral wavelengths and stress patterns in the developing brain. *Phys Biol* 10:016005.
- Bayly PV, Taber LA, Kroenke CD (2014) Mechanical forces in cerebral cortical folding: a review of measurements and models. *Journal of the mechanical behavior of biomedical materials* 29:568–581.

- Beaulieu-Laroche L, Brown NJ, Hansen M, Toloza EHS, Sharma J, Williams ZM, Frosch MP, Cosgrove GR, Cash SS, Harnett MT (2021) Allometric rules for mammalian cortical layer 5 neuron biophysics. *Nature* 600:274–278.
- Beining M, Mongiat LA, Schwarzacher SW, Cuntz H, Jedlicka P (2017) T2N as a new tool for robust electrophysiological modeling demonstrated for mature and adult-born dentate granule cells. *eLife* 6:e26517.
- Benavides-Piccione R, Ballesteros-Yáñez I, DeFelipe J, Yuste R (2002) Cortical area and species differences in dendritic spine morphology. *Journal of Neurocytology* pp. 337–346.
- Benavides-Piccione R, Regalado-Reyes M, Fernaud-Espinosa I, Kastanauskaite A, Tapiá-González S, LeÁn-Espinosa G, Rojo C, Insausti R, Segev I, DeFelipe J (2020) Differential Structure of Hippocampal CA1 Pyramidal Neurons in the Human and Mouse. *Cerebral Cortex* 30:730–752.
- Bianchi S, Stimpson CD, Bauernfeind AL, Schapiro SJ, Baze WB, McArthur MJ, Bronson E, Hopkins WD, Semendeferi K, Jacobs B, Hof PR, Sherwood CC (2013) Dendritic morphology of pyramidal neurons in the chimpanzee neocortex: regional specializations and comparison to humans. *Cereb Cortex* 23:2429–2436.
- Biondi A, Nogueira H, Dormont D, Duyme M, Hasboun D, Zouaoui A, Chantôme M, Marsault C (1998) Are the brains of monozygotic twins similar? A three-dimensional MR study. *AJNR Am J Neuroradiol* 19:1361–1367.
- Bird A, Cuntz H (2019) Dissecting Sholl Analysis into Its Functional Components. *Cell reports* 27(10):3081–3096.e5.
- Bird AD, Cuntz H (2016) Optimal current transfer in dendrites. *PLOS Computational Biology* 12:1–12.
- Blanpied T, Ehlers M (2004) Microanatomy of dendritic spines: emerging principles of synaptic pathology in psychiatric and neurological disease. *Biol Psychiatry* pp. 55(12):1121–1127.
- Bodmer R, Jan YN (1987) Morphological differentiation of the embryonic peripheral neurons in *Drosophila*. *Roux's archives of developmental biology* .
- Borg I, Groenen P (2005) *Modern Multidimensional Scaling* Springer-Verlag New York.

- Borrell V, Götz M (2014) Role of radial glial cells in cerebral cortex folding. *Curr Opin Neurobiol* 27:39–46.
- Borrell V, Reillo I (2012) Emerging roles of neural stem cells in cerebral cortex development and evolution. *Dev Neurobiol* 72:955–971.
- Borrell V (2018) How cells fold the cerebral cortex. *Journal of Neuroscience* 38:776–783.
- Bray D (1984) Axonal growth in response to experimentally applied mechanical tension. *Developmental Biology* 102:379–389.
- Buchin A, de Frates R, Nandi A, Mann R, Chong P, Ng L, Miller J, Hodge R, Kalmbach B, Bose S, Rutishauser U, McConoughey S, Lein E, Berg J, Sorensen S, Gwinn R, Koch C, Ting J, Anastassiou CA (2020) Multi-modal characterization and simulation of human epileptic circuitry. *bioRxiv* .
- Budday S, Raybaud C, Kuhl E (2014) A mechanical model predicts morphological abnormalities in the developing human brain. *Scientific Reports* 4:5644.
- Bullmore E, Sporns O (2012) The economy of brain network organization. *Nature Reviews Neuroscience* 13:336–349.
- Butti C, Raghanti MA, Sherwood CC, Hof PR (2011) The neocortex of cetaceans: cytoarchitecture and comparison with other aquatic and terrestrial species. *Ann N Y Acad Sci* 1225:47–58.
- Buxhoeveden DP, Casanova MF (2002) The minicolumn hypothesis in neuroscience. *Brain* 125:935–951.
- Capogna M (2011) Neurogliaform cells and other interneurons of stratum lacunosum-moleculare gate entorhinal-hippocampal dialogue. *J Physiol* 589:1875–1883.
- Carnevale NT, Hines ML (2006) *The NEURON Book*, pp. i–iv Cambridge University Press.
- Carper RA, Courchesne E (2005) Localized enlargement of the frontal cortex in early autism. *Biol Psychiatry* 57:126–133.
- Catani M, Dell’Acqua F, Budisavljevic S, Howells H, Thiebaut de Schotten M, Froudist-Walsh S, D’Anna L, Thompson A, Sandrone S, Bullmore ET, Suckling J, Baron-Cohen S, Lombardo MV, Wheelwright SJ, Chakrabarti B, Lai MC, Ruigrok ANV, Leemans A, Ecker C,

- Consortium MA, Craig MC, Murphy DGM (2016) Frontal networks in adults with autism spectrum disorder. *Brain : a journal of neurology* 139:616–630 26912520[pmid].
- Chada S, Lamoureux P, Buxbaum RE, Heidemann SR (1997) Cytomechanics of neurite outgrowth from chick brain neurons. *J Cell Sci* 110 (Pt 10):1179–1186.
- Chang BS, Piao X, Giannini C, Cascino GD, Scheffer I, Woods CG, Topcu M, Tezcan K, Bodell A, Leventer RJ, Barkovich AJ, Grant PE, Walsh CA (2004) Bilateral generalized polymicrogyria (BGP): a distinct syndrome of cortical malformation. *Neurology* 62:1722–1728.
- Charvet CJ, Cahalane DJ, Finlay BL (2015) Systematic, cross-cortex variation in neuron numbers in rodents and primates. *Cereb Cortex* 25:147–160.
- Charvet CJ, Reep RL, Finlay BL (2016) Evolution of cytoarchitectural landscapes in the mammalian isocortex: Sirenians (*Trichechus manatus*) in comparison with other mammals. *J Comp Neurol* 524:772–782.
- Chen XR, Heck N, Lohof A, Rochefort C, Morel M, Wehrlé R, Doulazmi M, Marty S, Cannaya V, Avci H, Mariani J, Rondi-Reig L, Vodjdani G, Sherrard R, Sotelo C, Dusart I (2013) Mature Purkinje cells require the retinoic acid-related orphan receptor-alpha (RORalpha) to maintain climbing fiber mono-innervation and other adult characteristics. *The Journal of neuroscience : the official journal of the Society for Neuroscience* 33(22):9546–9562.
- Chenn A, Walsh CA (2003) Increased neuronal production, enlarged forebrains and cytoarchitectural distortions in beta-catenin overexpressing transgenic mice. *Cereb Cortex* 13:599–606.
- Chklovskii DB, Koulakov AA (2004) Maps in the brain: what can we learn from them? *Annu Rev Neurosci* 27:369–392.
- Costa LF, Kaiser M, Hilgetag CC (2007) Predicting the connectivity of primate cortical networks from topological and spatial node properties. *BMC Systems Biology* 1:16.
- Courchesne E, Pierce K (2005) Why the frontal cortex in autism might be talking only to itself: local over-connectivity but long-distance disconnection. *Curr Opin Neurobiol* 15:225–230.
- Csernansky JG, Gillespie SK, Dierker DL, Anticevic A, Wang L, Barch DM, Van Essen DC (2008) Symmetric abnormalities in sulcal patterning in schizophrenia. *Neuroimage* 43:440–446.

- Cuntz H, Forstner F, Borst A, Häusser M (2010) One rule to grow them all: a general theory of neuronal branching and its practical application. *PLoS Computational Biology* 6:e1000877.
- Cuntz H, Haag J, Forstner F, Segev I, Borst A (2007) Robust coding of flow-field parameters by axo-axonal gap junctions between fly visual interneurons. *PNAS* 104:10229–10233.
- Curtis HJ, Cole KS (1938) TRANSVERSE ELECTRIC IMPEDANCE OF THE SQUID GIANT AXON. *J Gen Physiol* 21:757–765.
- de Juan Romero C, Bruder C, Tomasello U, Sanz-Anquela JM, Borrell V (2015) Discrete domains of gene expression in germinal layers distinguish the development of gyrencephaly. *EMBO J* 34:1859–1874.
- De Schutter E, Jaeger D (2000) *Computational Neuroscience: Realistic Modeling for Experimentalists (1st ed.)*, chapter 6 CRC Press.
- DeFelipe J (2011) The evolution of the brain, the human nature of cortical circuits, and intellectual creativity. *Frontiers in neuroanatomy* p. 29.
- DeFelipe J (2015) The anatomical problem posed by brain complexity and size: a potential solution. *Frontiers in neuroanatomy* 9.
- Dehay C, Horsburgh G, Berland M, Killackey H, Kennedy H (1991) The effects of bilateral enucleation in the primate fetus on the parcellation of visual cortex. *Brain research. Developmental brain research* 62 1:137–41.
- Del Toro D, Ruff T, Cederfjäll E, Villalba A, Seyit-Bremer G, Borrell V, Klein R (2017) Regulation of Cerebral Cortex Folding by Controlling Neuronal Migration via FLRT Adhesion Molecules. *Cell* 169:621–635.
- Dennerll TJ, Lamoureux P, Buxbaum RE, Heidemann SR (1989) The cytom mechanics of axonal elongation and retraction. *The Journal of cell biology* 109:3073–3083 2592415[pmid].
- Desmond NL, Scott CA, Jane JA, Levy WB (1994) Ultrastructural identification of entorhinal cortical synapses in CA1 stratum lacunosum-moleculare of the rat. *Hippocampus* 4:594–600.
- Di Donato N, Chiari S, Mirzaa GM, Aldinger K, Parrini E, Olds C, Barkovich AJ, Guerrini R, Dobyns WB (2017) Lissencephaly: Expanded imaging and clinical classification. *Am J Med Genet A* 173:1473–1488.

- Domínguez-Álvaro M, Montero-Crespo M, Blazquez-Llorca L, Insausti R, DeFelipe J, Alonso-Nanclares L (2018) Three-dimensional analysis of synapses in the transentorhinal cortex of Alzheimer's disease patients. *Acta Neuropathologica Communications* .
- Donohue DE, Ascoli GA (2008) A comparative computer simulation of dendritic morphology. *PLOS Computational Biology* 4:1–15.
- Elston GN (2003) Cortex, cognition and the cell: new insights into the pyramidal neuron and prefrontal function. *Cereb Cortex* 13:1124–1138.
- Elston GN, Benavides-Piccione R, DeFelipe J (2001) The pyramidal cell in cognition: a comparative study in human and monkey. *J Neurosci* 21:RC163.
- Elston G, Manger P (2014) Pyramidal cells in v1 of african rodents are bigger, more branched and more spiny than those in primates. *Frontiers in Neuroanatomy* 8:4.
- Elston GN (2000) Pyramidal cells of the frontal lobe: All the more spinous to think with. *Journal of Neuroscience* 20:RC95–RC95.
- Ercsey-Ravasz M, Markov NT, Lamy C, Van Essen DC, Knoblauch K, Toroczkai Z, Kennedy H (2013) A predictive network model of cerebral cortical connectivity based on a distance rule. *Neuron* 80:184–197.
- Eyal G, Verhoog MB, Testa-Silva G, Deitcher Y, Benavides-Piccione R, DeFelipe J, de Kock CPJ, Mansvelder HD, Segev I (2018) Human cortical pyramidal neurons: From spines to spikes via models. *Frontiers in Cellular Neuroscience* 12.
- Eyal G, Verhoog MB, Testa-Silva G, Deitcher Y, Lodder JC, Benavides-Piccione R, Morales J, DeFelipe J, de Kock CP, Mansvelder HD, Segev I (2016) Unique membrane properties and enhanced signal processing in human neocortical neurons. *eLife* 5:e16553.
- Falconer K (2004) *Fractal geometry: mathematical foundations and applications* Chichester: John Wiley and Sons.
- Felleman DJ, Van Essen DC (1991) Distributed hierarchical processing in the primate cerebral cortex. *Cereb Cortex* 1:1–47.
- Fernández V, Llinares-Benadero C, Borrell V (2016) Cerebral cortex expansion and folding: what have we learned? *EMBO J* 35:1021–1044.

- Fischl B, Rajendran N, Busa E, Augustinack J, Hinds O, Yeo BT, Mohlberg H, Amunts K, Zilles K (2008) Cortical folding patterns and predicting cytoarchitecture. *Cereb Cortex* 18:1973–1980.
- Footo AD, Liu Y, Thomas GWC, Vinař T, Alföldi J, Deng J, Dugan S, van Elk CE, Hunter ME, Joshi V, Khan Z, Kovar C, Lee SL, Lindblad-Toh K, Mancina A, Nielsen R, Qin X, Qu J, Raney BJ, Vijay N, Wolf JBW, Hahn MW, Muzny DM, Worley KC, Gilbert MTP, Gibbs RA (2015) Convergent evolution of the genomes of marine mammals. *Nature genetics* 47:272–275 25621460[pmid].
- Francis F, Meyer G, Fallet-Bianco C, Moreno S, Kappeler C, Socorro AC, Tuy FP, Beldjord C, Chelly J (2006) Human disorders of cortical development: from past to present. *Eur J Neurosci* 23:877–893.
- Franze K (2013) The mechanical control of nervous system development. *Development* 140:3069–3077.
- Geng G, Johnston LA, Yan E, Britto JM, Smith DW, Walker DW, Egan GF (2009) Biomechanisms for modelling cerebral cortical folding. *Med Image Anal* 13:920–930.
- Gentet LJ, Stuart GJ, Clements JD (2000) Direct measurement of specific membrane capacitance in neurons. *Biophysical Journal* 79:314–320.
- Geoffroy PA, Houenou J, Duhamel A, Amad A, De Weijer AD, Curčić-Blake B, Linden DE, Thomas P, Jardri R (2014) The Arcuate Fasciculus in auditory-verbal hallucinations: a meta-analysis of diffusion-tensor-imaging studies. *Schizophr Res* 159:234–237.
- Geschwind DH, Rakic P (2013) Cortical evolution: judge the brain by its cover. *Neuron* p. 633–647.
- Gilmore EC, Walsh CA (2013) Genetic causes of microcephaly and lessons for neuronal development. *Wiley Interdiscip Rev Dev Biol* 2:461–478.
- Glass M, Dragunow M (1995) Neurochemical and morphological changes associated with human epilepsy. *Brain Research Reviews* 21:29–41.
- Greenwood SM, Connolly CN (2007) Dendritic and mitochondrial changes during glutamate excitotoxicity. *Neuropharmacology* 53:891–898.

- Groden M, Weigand M, Triesch J, Jedlicka P, Cuntz H (2019) A Model of Brain Folding Based on Strong Local and Weak Long-Range Connectivity Requirements. *Cerebral Cortex* 30:2434–2451.
- Gulledge AT, Kampa BM, Stuart GJ (2005) Synaptic integration in dendritic trees. *Journal of Neurobiology* 64:75–90.
- Han C, Wang D, Soba P, Zhu S, Lin X, Jan L, Jan YN (2012) Integrins Regulate Repulsion-Mediated Dendritic Patterning of Drosophila Sensory Neurons by Restricting Dendrites in a 2D Space. *Neuron* 73:64–78.
- Hanein Y, Tadmor O, Anava S, Ayali A (2011) Neuronal soma migration is determined by neurite tension. *Neuroscience* 172:572–579.
- Hardan AY, Jou RJ, Keshavan MS, Varma R, Minshew NJ (2004) Increased frontal cortical folding in autism: a preliminary MRI study. *Psychiatry Res* 131:263–268.
- Heidemann SR, Lamoureux P, Buxbaum RE (1995) Cytomechanics of axonal development. *Cell Biochem Biophys* 27:135–155.
- Hellwig B (2000) A quantitative analysis of the local connectivity between pyramidal neurons in layers 2/3 of the rat visual cortex. *Biol Cybern* 82:111–121.
- Herculano-Houzel S (2014) The glia/neuron ratio: how it varies uniformly across brain structures and species and what that means for brain physiology and evolution. *Glia* 62:1377–1391.
- Herculano-Houzel S (2009) The human brain in numbers: a linearly scaled-up primate brain. *Frontiers in Human Neuroscience* 3:31.
- Herculano-Houzel S, Mota B, Wong P, Kaas JH (2010) Connectivity-driven white matter scaling and folding in primate cerebral cortex. *Proceedings of the National Academy of Sciences* 107:19008–19013.
- Hilgetag CC, Barbas H (2009) Sculpting the brain. *Sci Am* 300:66–71.
- Hilgetag CC, Barbas H (2006) Role of mechanical factors in the morphology of the primate cerebral cortex. *PLOS Computational Biology* 2:1–14.

- Hodge RD, Bakken TE, Miller JA, Smith KA, Barkan ER, Graybuck LT, Close JL, Long B, Johansen N, Penn O, Yao Z, Eggermont J, Höllt T, Levi BP, Shehata SI, Aevermann B, Beller A, Bertagnolli D, Brouner K, Casper T, Cobbs C, Dalley R, Dee N, Ding SL, Ellenbogen RG, Fong O, Garren E, Goldy J, Gwinn RP, Hirschstein D, Keene CD, Keshk M, Ko AL, Lathia K, Mahfouz A, Maltzer Z, McGraw M, Nguyen TN, Nyhus J, Ojemann JG, Oldre A, Parry S, Reynolds S, Rimorin C, Shapovalova NV, Somasundaram S, Szafer A, Thomsen ER, Tieu M, Quon G, Scheuermann RH, Yuste R, Sunkin SM, Lelieveldt B, Feng D, Ng L, Bernard A, Hawrylycz M, Phillips JW, Tasic B, Zeng H, Jones AR, Koch C, Lein ES (2019) Conserved cell types with divergent features in human versus mouse cortex. *Nature* .
- Hof PR, Van Der Gucht E (2007) Structure of the cerebral cortex of the humpback whale, *megaptera novaeangliae* (cetacea, mysticeti, balaenopteridae). *The Anatomical Record* 290:1–31.
- Hofman MA (1985) Size and shape of the cerebral cortex in mammals. I. The cortical surface. *Brain Behav Evol* 27:28–40.
- Hofman M (2014) Evolution of the human brain: when bigger is better. *Frontiers in Neuroanatomy* 8:15.
- Horcholle-Bossavit G, Gogan P, Ivanov Y, Korogod S, Tyc-Dumont S (2000) The problem of the morphological noise in reconstructed dendritic arborizations. *Journal of Neuroscience Methods* 95:83–93.
- Houser C (1992) Morphological changes in the dentate gyrus in human temporal lobe epilepsy. *Epilepsy research. Supplement* 7:223—234.
- Huggenberger S (2008) The size and complexity of dolphin brains—a paradox? *Journal of the Marine Biological Association of the United Kingdom* 88:1103–1108.
- Ito HT, Schuman EM (2012) Functional division of hippocampal area ca1 via modulatory gating of entorhinal cortical inputs. *Hippocampus* 22:372–387.
- Jansen A, Andermann E (2005) Genetics of the polymicrogyria syndromes. *Journal of medical genetics* 42:369–378 15863665[pmid].
- Jarsky T, Roxin A, Kath W, Spruston N (2005) Conditional dendritic spike propagation following distal synaptic activation of hippocampal CA1 pyramidal neurons. *Nat Neurosci.* pp. 8(12):1667–1676.

- Jarvis ED, Güntürkün O, Bruce L, Csillag A, Karten H, Kuenzel W, Medina L, Paxinos G, Perkel DJ, Shimizu T, Striedter G, Wild JM, Ball GF, Dugas-Ford J, Durand SE, Hough GE, Husband S, Kubikova L, Lee DW, Mello CV, Powers A, Siang C, Smulders TV, Wada K, White SA, Yamamoto K, Yu J, Reiner A, Butler AB (2005) Avian brains and a new understanding of vertebrate brain evolution. *Nature Reviews Neuroscience* 6:151–159.
- Just MA, Cherkassky VL, Keller TA, Kana RK, Minshew NJ (2007) Functional and anatomical cortical underconnectivity in autism: evidence from an fMRI study of an executive function task and corpus callosum morphometry. *Cereb Cortex* 17:951–961.
- Kaas JH (2013) The evolution of brains from early mammals to humans. *WIREs Cognitive Science* 4:33–45.
- Kaiser M, Hilgetag CC, van Ooyen A (2009) A simple rule for axon outgrowth and synaptic competition generates realistic connection lengths and filling fractions. *Cereb Cortex* 19:3001–3010.
- Kalmanti E, Maris TG (2007) Fractal dimension as an index of brain cortical changes throughout life. *In Vivo* 21:641–646.
- Kao YC, Peng SS, Weng WC, Lin MI, Lee WT (2011) Evaluation of white matter changes in agyria-pachygyria complex using diffusion tensor imaging. *J Child Neurol* 26:433–439.
- Kellmeyer P (2021) Big brain data: On the responsible use of brain data from clinical and consumer-directed neurotechnological devices. *Neuroethics* .
- Kingsbury MA, Rehen SK, Contos JJ, Higgins CM, Chun J (2003) Non-proliferative effects of lysophosphatidic acid enhance cortical growth and folding. *Nat Neurosci* 6:1292–1299.
- Kroenke CD, Bayly PV (2018) How forces fold the cerebral cortex. *Journal of Neuroscience* 38:767–775.
- Kötter R, Feizelmeier M (1998) Species-dependence and relationship of morphological and electrophysiological properties in nigral compacta neurons. *Progress in Neurobiology* 54:619–632.
- Lamoureux P, Buxbaum RE, Heidemann SR (1989) Direct evidence that growth cones pull. *Nature* 340:159–162.

10. REFERENCES

- Laughlin SB, Sejnowski TJ (2003) Communication in neuronal networks. *Science* 301:1870–1874.
- Lawton AK, Engstrom T, Rohrbach D, Omura M, Turnbull DH, Mamou J, Zhang T, Schwarz JM, Joyner AL (2019) Cerebellar folding is initiated by mechanical constraints on a fluid-like layer without a cellular pre-pattern. *eLife* 8:e45019.
- Lee SK, Mori S, Kim DJ, Kim SY, Kim SY, Kim DI (2004) Diffusion tensor mr imaging visualizes the altered hemispheric fiber connection in callosal dysgenesis. *American Journal of Neuroradiology* 25:25–28.
- Li D, Li F, Guttipatti P, Song Y (2018) A Drosophila In Vivo Injury Model for Studying Neuroregeneration in the Peripheral and Central Nervous System. *J Vis Exp* p. (135):57557.
- Liu JZ, Zhang LD, Yue GH (2003) Fractal dimension in human cerebellum measured by magnetic resonance imaging. *Biophysical journal* 85:4041–4046 14645092[pmid].
- Llinares-Benadero C, Borrell V (2019) Deconstructing cortical folding: genetic, cellular and mechanical determinants. *Nat Rev Neurosci* 20:161–176.
- Lohmann G, von Cramon DY, Steinmetz H (1999) Sulcal variability of twins. *Cereb Cortex* 9:754–763.
- London M, Häusser M (2005) Dendritic computation. *Annual Review of Neuroscience* 28:503–532 PMID: 16033324.
- Mainen Z, Sejnowski T (1996) Influence Of Dendritic Structure On Firing Pattern In Model Neocortical Neurons. *Nature* 382:363–6.
- Mandelbrot B (1983) *The fractal geometry of nature* New York: W.H. Freeman and Company.
- Martínez-Martínez MA, De Juan Romero C, Fernández V, Cárdenas A, Götz M, Borrell V (2016) A restricted period for formation of outer subventricular zone defined by Cdh1 and Trnp1 levels. *Nat Commun* 7:11812.
- Mayer G, Whittington PM (2009) Neural development in onychophora (velvet worms) suggests a step-wise evolution of segmentation in the nervous system of panarthropoda. *Developmental Biology* 335:263–275.

- McDougal RA, Morse TM, Carnevale T, Marengo L, Wang R, Migliore M, Miller PL, Shepherd GM, Hines ML (2017) Twenty years of ModelDB and beyond: building essential modeling tools for the future of neuroscience. *Journal of Computational Neuroscience* .
- Mihaljevic B, Larranaga P, Benavides-Piccione R, DeFelipe J, Bielza C (2020) Comparing basal dendrite branches in human and mouse hippocampal CA1 pyramidal neurons with Bayesian networks. *Scientific Reports* .
- Moon HM, Wynshaw-Boris A (2013) Cytoskeleton in action: lissencephaly, a neuronal migration disorder. *Wiley Interdiscip Rev Dev Biol* 2:229–245.
- Mora-Bermúdez F, Badsha F, Kanton S, Camp JG, Vernot B, Köhler K, Voigt B, Okita K, Maricic T, He Z, Lachmann R, Pääbo S, Treutlein B, Huttner WB (2016) Differences and similarities between human and chimpanzee neural progenitors during cerebral cortex development. *eLife* 5:e18683.
- Mota B, Herculano-Houzel S (2012) How the cortex gets its folds: an inside-out, connectivity-driven model for the scaling of Mammalian cortical folding. *Front Neuroanat* 6:3.
- Mota B, Herculano-Houzel S (2014) All brains are made of this: a fundamental building block of brain matter with matching neuronal and glial masses. *Front Neuroanat* 8:127.
- Mota B, Herculano-Houzel S (2015) Cortical folding scales universally with surface area and thickness, not number of neurons. *Science* 349:74–77.
- Mountcastle VB (1997) The columnar organization of the neocortex. *Brain* 120 (Pt 4):701–722.
- Nonaka-Kinoshita M, Reillo I, Artegiani B, Martínez-Martínez MA, Nelson M, Borrell V, Calegari F (2013) Regulation of cerebral cortex size and folding by expansion of basal progenitors. *EMBO J* 32:1817–1828.
- Nordahl CW, Dierker D, Mostafavi I, Schumann CM, Rivera SM, Amaral DG, Van Essen DC (2007) Cortical folding abnormalities in autism revealed by surface-based morphometry. *J Neurosci* 27:11725–11735.
- Oberheim N, Takano T, Han X, He W, Lin J, Wang F, Xu Q, Wyatt J, Pilcher W, Ojemann J, Ransom B, Goldman S, Nedergaard M (2009) Uniquely hominid features of adult human astrocytes. *J Neurosci* pp. 3276–87.

- O'Leary DD, Chou SJ, Sahara S (2007) Area patterning of the mammalian cortex. *Neuron* 56:252–269.
- O'Leary T, Sutton AC, Marder E (2015) Computational models in the age of large datasets. *Curr Opin Neurobiol* 32:87–94.
- Palk A, Illes J, Thompson PM, Stein DJ (2020) Ethical issues in global neuroimaging genetics collaborations. *NeuroImage* 221:117208.
- Parekh R, Ascoli G (2013) *NeuroMorpho.org*, pp. 1–3 Springer New York, New York, NY.
- Penzes P, Cahill ME, Jones KA, VanLeeuwen JE, Woolfrey KM (2011) Dendritic spine pathology in neuropsychiatric disorders. *Nature Neuroscience* .
- Pillay P, Manger PR (2007) Order-specific quantitative patterns of cortical gyrification. *Eur J Neurosci* 25:2705–2712.
- Poirazi P, Papoutsis A (2020) Illuminating dendritic function with computational models. *Nature Reviews Neuroscience* pp. 303–321.
- Poluch S, Juliano SL (2015) Fine-tuning of neurogenesis is essential for the evolutionary expansion of the cerebral cortex. *Cereb Cortex* 25:346–364.
- Prothero JW, Sundsten JW (1984) Folding of the cerebral cortex in mammals. *Brain, Behavior and Evolution* 24:152–167.
- Rai B, Gouda R, Moka S, Dunbar LE (2015) Isolated Microtia With Anterior Hemispheric Polymicrogyria. *J Child Neurol* 30:1086–1088.
- Raj A, Chen Yh (2011) The wiring economy principle: Connectivity determines anatomy in the human brain. *PLOS ONE* 6:1–11.
- Rakic P (1988) Specification of cerebral cortical areas. *Science* 241:170–176.
- Rash BG, Duque A, Morozov YM, Arellano JI, Micali N, Rakic P (2019) Gliogenesis in the outer subventricular zone promotes enlargement and gyrification of the primate cerebrum. *Proc Natl Acad Sci U S A* 116:7089–7094.
- Reillo I, de Juan Romero C, García-Cabezas MA, Borrell V (2011) A role for intermediate radial glia in the tangential expansion of the mammalian cerebral cortex. *Cereb Cortex* 21:1674–1694.

- Richman DP, Stewart RM, Hutchinson JW, Caviness VS (1975) Mechanical model of brain convolutional development. *Science* 189:18–21.
- Rilling JK (2014) Comparative primate neuroimaging: insights into human brain evolution. *Trends in Cognitive Sciences* 18:46–55.
- Ronan L, Fletcher P (2015) From genes to folds: a review of. *Brain Struct Funct* 220:2475–2483.
- Ronan L, Voets N, Rua C, Alexander-Bloch A, Hough M, Mackay C, Crow TJ, James A, Giedd JN, Fletcher PC (2014) Differential tangential expansion as a mechanism for cortical gyrification. *Cereb Cortex* 24:2219–2228.
- Ruppin E, Schwartz EL, Yeshurun Y (1993) Examining the volume efficiency of the cortical architecture in a multi-processor network model. *Biol Cybern* 70:89–94.
- Scannell JW (1997) Determining cortical landscapes. *Nature* 386:452–452.
- Schmidt ERE, Polleux F (2022) Genetic mechanisms underlying the evolution of connectivity in the human cortex. *Frontiers in Neural Circuits* 15.
- Schmidt-Hieber C, Jonas P, Bischofberger J (2007) Subthreshold dendritic signal processing and coincidence detection in dentate gyrus granule cells. *Journal of Neuroscience* 27:8430–8441.
- Sherwood C, Bauernfeind A, Bianchi S, Raghanti M, Hof P (2012) Human brain evolution writ large and small. *Prog Brain Res* pp. 237–54.
- Sholl D (1953) Dendritic organization in the neurons of the visual and motor cortices of the cat. *J Anat.* pp. 387–406.
- Shuman T, Amendolara B, Golshani P (2017) Theta rhythmopathy as a cause of cognitive disability in tle. *Epilepsy Currents* 17:107–111 PMID: 28491003.
- Sivagnanam S, Majumdar A, Yoshimoto K, Astakhov V, Bandrowski A, Martone M, Carnevale N (2013) Introducing the neuroscience gateway. *CEUR Workshop Proc.* Vol. 993.
- Skudlarski P, Jagannathan K, Anderson K, Stevens MC, Calhoun VD, Skudlarska BA, Pearlson G (2010) Brain connectivity is not only lower but different in schizophrenia: a combined anatomical and functional approach. *Biological psychiatry* 68:61–69 20497901[pmid].

- Song HF, Kennedy H, Wang XJ (2014) Spatial embedding of structural similarity in the cerebral cortex. *Proceedings of the National Academy of Sciences of the United States of America* 111:16580–16585 25368200[pmid].
- Song Y, Ori-McKenney K, Zheng Y, Han C, Jan L, Jan Y (2012) Regeneration of *Drosophila* sensory neuron axons and dendrites is regulated by the Akt pathway involving Pten and microRNA bantam. *Genes Dev.* pp. 1612–1625.
- Sporns O, Tononi G, Kötter R (2005) The human connectome: A structural description of the human brain. *PLoS Comput Biol* 1:e42.
- Stegen M, Kirchheim F, Hanuschkin A, Staszewski O, Veh RW, Wolfart J (2012) Adaptive intrinsic plasticity in human dentate gyrus granule cells during temporal lobe epilepsy. *Cereb Cortex* 22:2087–2101.
- Stegen M, Young CC, Haas CA, Zentner J, Wolfart J (2009) Increased leak conductance in dentate gyrus granule cells of temporal lobe epilepsy patients with Ammon’s horn sclerosis. *Epilepsia* 50:646–653.
- Stone M, Albertson R, Chen L, Rolls M (2014) Dendrite Injury Triggers DLK-Independent Regeneration. *Cell Reports* pp. 247–253.
- Sun T, Hevner RF (2014) Growth and folding of the mammalian cerebral cortex: from molecules to malformations. *Nat Rev Neurosci* 15:217–232.
- Szegedi V, Paizs M, Csakvari E, Molnar G, Barzo P, Tamas G, Lamsa K (2016) Plasticity in single axon glutamatergic connection to gabaergic interneurons regulates complex events in the human neocortex. *PLOS Biology* 14:1–21.
- Tallinen T, Chung J, Rousseau F, et al. (2016) On the growth and form of cortical convolutions. *Nature Phys* 12:588–593.
- Tallinen T, Chung JY, Biggins JS, Mahadevan L (2014) Gyrification from constrained cortical expansion. *Proceedings of the National Academy of Sciences* 111:12667–12672.
- Tilimbe J (2019) Ethical reflections of human brain research and smart information systems. *The ORBIT Journal* 2:1–24.

- Tischbirek CH, Noda T, Tohmi M, Birkner A, Nelken I, Konnerth A (2019) In vivo functional mapping of a cortical column at single-neuron resolution. *Cell Reports* 27:1319–1326.e5.
- Todd PH (1982) A geometric model for the cortical folding pattern of simple folded brains. *J Theor Biol* 97:529–538.
- Toro R, Burnod Y (2005) A morphogenetic model for the development of cortical convolutions. *Cereb Cortex* 15:1900–1913.
- Toro R, Perron M, Pike B, Richer L, Veillette S, Pausova Z, Paus T (2008) Brain size and folding of the human cerebral cortex. *Cereb Cortex* 18:2352–2357.
- Toro R (2012) On the possible shapes of the brain. *Evolutionary Biology* 39:600–612.
- Tosches MA, Yamawaki TM, Naumann RK, Jacobi AA, Tushev G, Laurent G (2018) Evolution of pallium, hippocampus, and cortical cell types revealed by single-cell transcriptomics in reptiles. *Science* 360:881–888.
- Trivedi R, Gupta R, Hasan K, Hou P, Prasad K, Narayana P (2006) Diffusion tensor imaging in polymicrogyria: a report of three cases. *Neuroradiology* 48:422–427.
- van der Maaten L, Hinton G (2008) Visualizing High-Dimensional Data Using t-SNE. *Journal of Machine Learning Research* pp. 2579–2605.
- Van Essen DC (1997) A tension-based theory of morphogenesis and compact wiring in the central nervous system. *Nature* 385:313–318.
- van Ooyen A, Duijnhouwer J, Remme MW, van Pelt J (2002) The effect of dendritic topology on firing patterns in model neurons. *Network* 13:311–325.
- van Pelt J, Schierwagen A (2004) Morphological analysis and modeling of neuronal dendrites. *Mathematical Biosciences* 188:147–155 *Topics in Biomathematics and Related Computational Problems: selected papers.*
- Volpe J (2008) *Neurology of the newborn* Philadelphia: Saunders, 5th ed edition.
- Walsh CA (1999) Genetic malformations of the human cerebral cortex. *Neuron* 23(1):19–29.
- Wang IE, Clandinin TR (2016) The Influence of Wiring Economy on Nervous System Evolution. *Curr Biol* 26:R1101–R1108.

- Wattenberg M, Viégas FB, Johnson I (2016) How to use t-sne effectively In *How to Use t-SNE Effectively*.
- Weigand M, Sartori F, Cuntz H (2017) Universal transition from unstructured to structured neural maps. *Proc Natl Acad Sci U S A* 114:E4057–E4064.
- Welker W (1990) Why does cerebral cortex fissure and fold? *Cerebral Cortex* 8B Boston: Springer:3–136.
- Wen Q, Chklovskii DB (2005) Segregation of the brain into gray and white matter: A design minimizing conduction delays. *PLOS Computational Biology* 1:1–14.
- Wisco JJ, Kuperberg G, Manoach D, Quinn BT, Busa E, Fischl B, Heckers S, Sorensen AG (2007) Abnormal cortical folding patterns within broca’s area in schizophrenia: evidence from structural mri. *Schizophrenia research* 94:317–327 17490861[pmid].
- Wyler AR, Curtis Dohan F, Schweitzer JB, Berry AD (1992) A grading system for mesial temporal pathology (hippocampal sclerosis) from anterior temporal lobectomy. *Journal of Epilepsy* 5:220–225.
- Xu G, Bayly PV, Taber LA (2009) Residual stress in the adult mouse brain. *Biomech Model Mechanobiol* 8:253–262.
- Xu G, Knutsen AK, Dikranian K, Kroenke CD, Bayly PV, Taber LA (2010) Axons pull on the brain, but tension does not drive cortical folding. *J Biomech Eng* 132:071013.
- Young CC, Stegen M, Bernard R, Müller M, Bischofberger J, Veh RW, Haas CA, Wolfart J (2009) Upregulation of inward rectifier K⁺ (Kir2) channels in dentate gyrus granule cells in temporal lobe epilepsy. *J Physiol* 587:4213–4233.
- Zhao X, Bhattacharyya A (2018) Human models are needed for studying human neurodevelopmental disorders. *The American Journal of Human Genetic* pp. 829–857.
- Zhu G, Du L, Jin L, Offenhäusser A (2016) Effects of morphology constraint on electrophysiological properties of cortical neurons. *Scientific Reports* 6:23086.
- Zilles K, Armstrong E, Moser KH, Schleicher A, Stephan H (1989) Gyrification in the cerebral cortex of primates. *Brain Behav Evol* 34:143–150.

10. REFERENCES

Zilles K, Armstrong E, Schleicher A, Kretschmann HJ (1988) The human pattern of gyrification in the cerebral cortex. *Anat Embryol (Berl)* 179:173–179.

Zilles K, Palomero-Gallagher N, Amunts K (2013) Development of cortical folding during evolution and ontogeny. *Trends Neurosci* 36:275–284.

11 Appendix

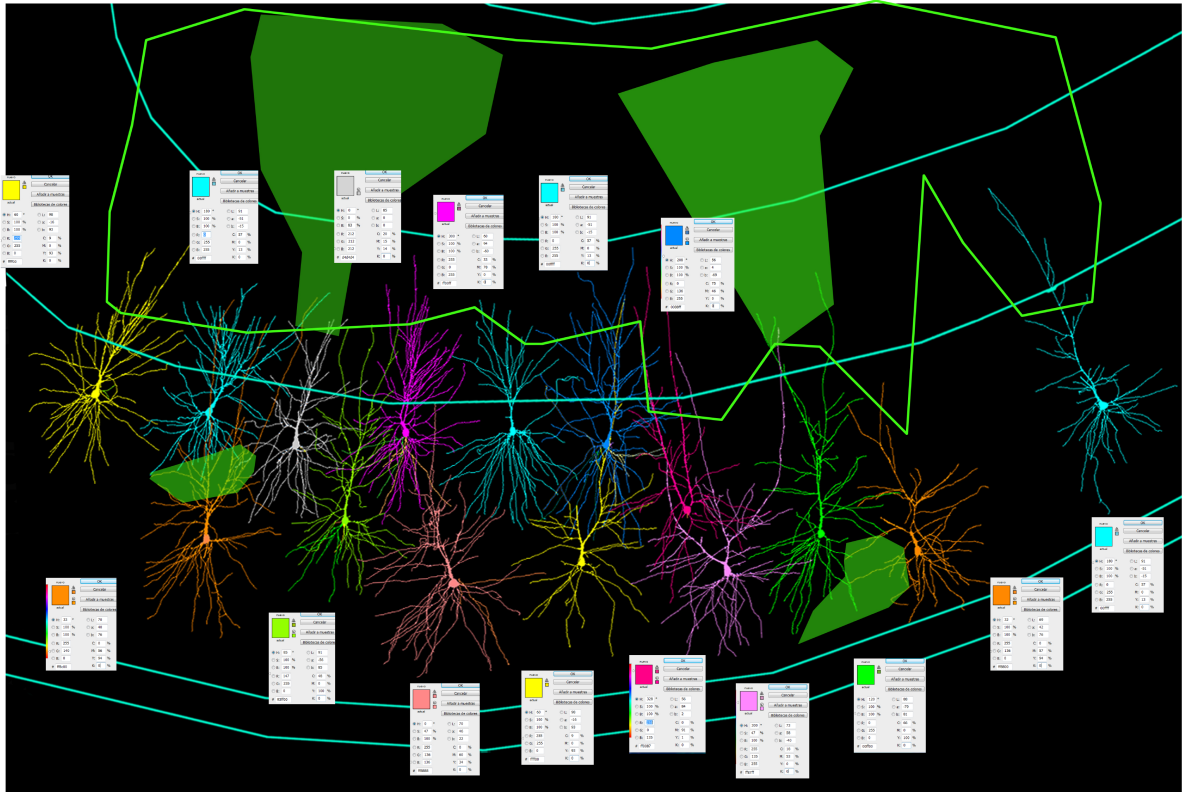


Figure S1. Human neuron extension volumes

Human CA1 pyramidal neuron data set region of interest (the same data as depicted in Fig. 33 and Fig. 34). This data is provided by Benavides-Piccione et al. (2020). The green shaded areas show potential dendrite extension volumes for the neuron repair tool drawn by Benavides-Piccione et al. (2020), showing where dendrites should be growing, since they could not be reconstructed successfully in these areas. The white panels show the RGB-colour code for each morphology.